Neuronal firing response and resonance, from theory to experiments, from single cell to population.

Alan Montarras

Alan Montarras. Neuronal firing response and resonance, from theory to experiments, from single cell to population.. Neurons and Cognition [q-bio.NC]. Université Paris sciences et lettres, 2022. English. NNT : 2022UPSLE083 . tel-04795792

HAL Id: tel-04795792
https://theses.hal.science/tel-04795792v1

Submitted on 21 Nov 2024

PSL
UNIVERSITÉ PARIS

THÈSE DE DOCTORAT
DE L'UNIVERSITÉ PSL

Préparée à Ecole Normale Supérieure

Réponse neuronale et résonance, de la théorie à l'expérience, de la cellule unique à la population

Soutenue par
Alan Montarras
Le 12 Décembre 2022

École doctorale n°158
Cerveau, cognition, comportement (3C)

Spécialité
Neurosciences

Composition du jury :

Nicolas Brunel Professor, Duke University	*Président du jury* *Rapporteur*
Arnd Roth Senior Research Fellow, University College London	*Rapporteur*
Alex Cayco Gajic Junior Professor, Département d'Études cognitive de l'Ecole Normale Supérieure	*Examinateur*
Joao Couto Senior Post-Doc, University of California Los Angeles	*Examinateur*
Boris Barbour Directeur de recherche, Institut de Biologie de l'Ecole Normale Supérieure	*Directeur de thèse*
Jonas Ranft Chargé de recherche, Institut de Biologie de l'Ecole Normale Supérieure	*Invité*

1794
ENS | PSL

Thesis Report

Neuronal firing response and resonance

From theory to experiments
From single cell to population

Alan Montarras

École Normale Supérieure, Université PSL.
École Doctorale N°158 Cerveau Cognition Comportement.

September 22, 2023

Jury:

- **Nicolas Brunel**, Rapporteur, Président du jury.
  Professor, Duke University.
- **Arnd Roth**, Rapporteur.
  Senior Research Fellow, University College London.
- **Alex Cayco Gajic**, Examinateur.
  Junior Professor, Département d'Études Cognitives de l'École Normale Supérieure.
- **Joao Couto**, Examinateur.
  Senior Post-Doc, University of California Los Angeles.
- **Boris Barbour**, Directeur de thèse.
  Directeur de recherche, Institut de Biologie de l'École Normale Supérieure.
- **Jonas Ranft**, Invité.
  Chargé de recherche, Institut de Biologie de l'École Normale Supérieure.

Contents

Summary 1

I Introduction 3

1 Membrane Resonance 4
- 1.1 Impedance 4
  - 1.1.1 The neuron as an electrical circuit 4
  - 1.1.2 Definition 6
  - 1.1.3 Neuronal impedance 7
- 1.2 Mechanisms of membrane resonance 14
  - 1.2.1 Passive components 14
  - 1.2.2 Active components 16
  - 1.2.3 Resonance and oscillation 18

2 Firing Resonance 21
- 2.1 The Neuron's output 21
  - 2.1.1 The Action Potential 21
  - 2.1.2 Models of a spiking neuron 22
- 2.2 Fast Population encoding 23
  - 2.2.1 Synaptic noise and filtering 23
  - 2.2.2 Experimental frequency responses 27
- 2.3 From sub-threshold to firing 28
  - 2.3.1 From theory 28
  - 2.3.2 To experiments 28

3 The Purkinje cell 36

II Results 42

4 Preliminary work 43
- 4.1 First protocols of resonance 43
- 4.2 Firing rate clamp 44
- 4.3 PRC 46

Precise measurement and mechanistic modelling
of high-frequency firing resonance
of cerebellar Purkinje cells
48

III Discussion **88**

5 General remarks **89**
5.1 A general and cell specific model ? . . . 89
5.2 Noise . . . 89
5.3 High-frequency resonance . . . 90

6 Perspectives **92**
6.1 Potassium channels . . . 92
6.2 Pyramidal cells . . . 94

References **98**

Personal Statement **105**

Summary

The Brain is a hugely complex environment. Billions of neurons stacked in numerous different interconnected areas. Each area is its own universe of different cellular types connecting between and within neuronal classes. Individual neurons are complex to understand alone.

Populations of neurons generate electrical waves when they synchronise. Distinct frequencies have been identified in the brain for specific populations. But, more importantly, in a desynchronised state a population is simply a combination of multiple frequencies. This raises the question of how populations of neurons integrate the information present from all of these frequencies? We could draw a parallel with radio waves; using a tuned receiver we can tune into one singular frequency to listen to what is noise when taken as a whole. Can information be transmitted in this manner through the brain?

Neurons themselves act as integrators; they combine the multiple synaptic inputs and produce action potentials as output. We can then imagine the population of neurons as a population of spiking units. As a population the neurons can be more responsive to specific frequencies. Populations of neurons could then encode or store information on the basis of their preferred frequencies.

Moreover, neurons do have preferred frequencies. They sometimes exhibit what is called membrane (subthreshold) resonance that can amplify inputs for a certain frequency range. How this impacts the output firing is still rather unclear. A neuron's output can also be sensitive to the input's frequency. This is called firing resonance. How the two resonances interact with each other will be the starting point of this work. The goal of the study was to build a simple and mechanistic model of the Purkinje cell to which we would compare the experimental results cell by cell.

The framework of the project was to have as much specific information on every cell, in the most precise manner, in order to build our models respecting inter-cellular variability. For each experiment, short voltage-steps transient responses were probed as well as the impedance at different voltages. These two experiments were the basis to fit (transients) and test (impedance) the sub-threshold dynamics of our model cells. We chose to start with a passive three compartment model to account for the massive dendritic arborisation of the Purkinje cell.

The spike triggering was implemented with an exponential integrate and fire mechanism (EIF) to which was added a time dependent potassium after hyperpolarisation (AHP) current.

It appeared that probing the firing profile of the cells in a precise and re-

producible manner was not an easy task. Preliminary results emphasised that struggle. We implemented a “firing rate clamp” in order to stabilise the firing responses, and designed a “comb” frequency profile protocol with simultaneous low-noise probing of 50 frequencies.

Interestingly, the impendance measurements revealed several imperfections in the amplifier’s high frequency responses in voltage-clamp and current-clamp. The overall findings revealed a strong high-frequency firing resonance in the Purkinje cells that could not be reproduced by our simple model despite a very satisfactory cell-to-cell comparison of the sub-threshold behaviour. The addition of a potassium after hyperpolarising current to an EIF spike mechanism made it possible to extrapolate the impact of the action potential to the passive dendritic compartments. This gave potential additional explanations for the high-frequency firing rate of the Purkinje cells.

This accurate model will make possible some extensive research of possible mechanisms with the model as a tool. Additionally experiments were done on another cellular type, neocortical Pyramidal cells. Fitting the model’s structure to these cells will provide an challenging test of the model’s robustness.

Part I

Introduction

1 Membrane Resonance

1.1 Impedance

1.1.1 The neuron as an electrical circuit

The neuron's enclosure is a bi-lipidic membrane filled with ionic channels. As the membrane is impermeable to ions, their concentration can differ from the outside to the inside of the cell. Ions are electrically charged, therefore those concentration differences, accompanied with organic anions "trapped" inside the cell, creates a voltage difference across the membrane that we call abusively: membrane potential (V_m). By definition Vm is the difference between the potentials of the inside and the outside of the cell. The main ions to take into consideration are Na^+, K^+, Cl^-. The flow of ions across the membrane is then controlled by the combination of concentration and electrical gradients. This is represented by the Nernst Equation that describes each ion's equilibrium (sometimes called reversal or Nernst) potential:

$$E_{ion} = \frac{RT}{zF} \ln \frac{[ion]_{out}}{[ion]_{in}}$$

*R is the gas constant (1.98 cal/°K*mol), F the Faraday constant (96.480 C/mol), T the absolute temperature (°K) and z the ion's valence.*

A last, and crucial, component is needed to complete the picture: the permeability of each ionic species (P_i). Permeability represents the capacity of the membrane to let a specific ion through. It is set by the type of the neuron's channels , their number and opening states. This was added to the Nernst equation, to give the more specific Goldman-Hodgkin-Katz (GHK) equation of the membrane potential:

$$V_m = \frac{RT}{F} \ln \frac{P_K[K^+]_{out} + P_{Na}[Na^+]_{out} + P_{Cl}[Cl^-]_{in}}{P_K[K^+]_{in} + P_{Na}[Na^+]_{in} + P_{Cl}[Cl^-]_{out}}$$

P_i is dimensionless, it is a number between 0 and 1.

One can transpose those biological features into electronic equivalents by treating the membrane as a capacitor (C_m), the equilibrium potentials as the electromotive force (E_i) and permeability as conductance (G_i), which is the inverse of the resistance ($R_i = 1/G_i$). As the channels are within the membrane the conductances are positioned in parallel to the capacitance (Figure 1a). With Thévenin's theorem it can be simplified into a parallel RC circuit. This rather simple circuit is enough to exhibit and understand a great variety of a neuron's passive behaviours.

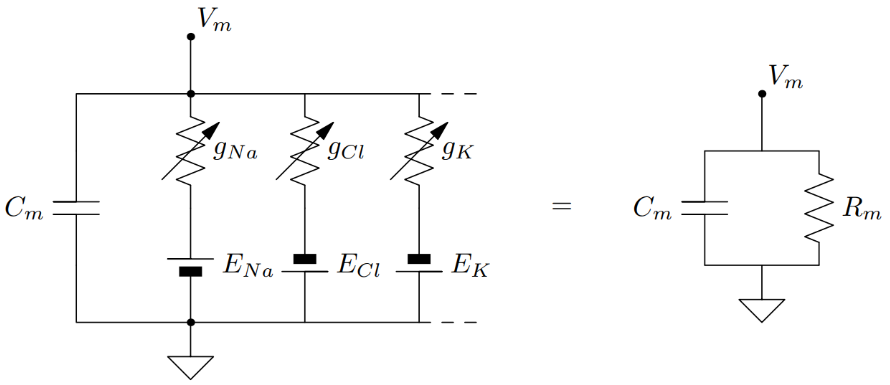

(a) Parallel conductance model with Thévenin's simplification.

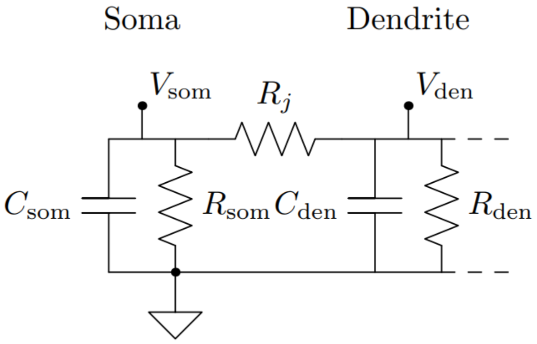

(b) Compartimental model.

Figure 1:
Neuron equivalent circuits
R for resistance, g for conductance, C for capacitance and E for electromotive force. R_j stands for junction resistance between compartments. From Barbour, 2018.

The membrane capacitance (C_m), represents the size of the cell but not the shape, so sometimes it can be necessary to add complexity to the circuit and add compartments (Figure 1b). Neurons are generally composed of a soma, where the nucleus is, and dendrites departing from it with a vast diversity of length, ramifications and shapes. This will be important when trying to understand impedance and spiking resonance in such extensively ramified cells as the Purkinje or Pyramidal cells. A capacitor takes time to charge and discharge. Thus, any inward or outward current will affect the potential with a certain delay due to this time of charge. This time is quantified by the membrane (or circuit) time constant:

$$I_m = C_m \frac{dV_m}{dt} + \frac{V_m}{R_m}$$

$$V_m = I_m R_m - \tau_m \frac{dV_m}{dt}$$

with:

$$\tau_m = R_m C_m = \frac{C_m}{G_m}$$

τ_m is expressed in seconds, R_m is the membrane resistance (Ω), G_m the membrane conductance (S) and C_m the capacitance (C).

1.1.2 Definition

One intuitive way of thinking of a neuron as an electric circuit is to analyse it with respect to time. One usually represents membrane voltage as: V_m(t). Before introducing the notion of impedance it can be interesting to change perspective and switch from time to frequency domain.

The idea is to look at the voltage not as a time dependent variable but as the sum of an infinite number of sine waves of different frequency, amplitude and phase shift. This is the Fourier transform principle, therefore we say that we have moved to the frequency domain. For each wanted frequency you can then find an amplitude and phase shift from the voltage and current trace. Impedance is a more general form of resistance, it can be used in the frequency domain:

$$Z(f) = \frac{V(f)}{I(f)}$$

Impedance is the generalization of resistance

The Fast Fourier Transform (FFT) is an algorithm that transforms a signal reversibly (iFFT) into the frequency domain, it will be used extensively through the manuscript. The ratio of amplitudes ($|Z|$) and the difference between phase shifts ($arg(Z)$) are embedded in the notion of impedance. For this reason a complex representation is usually more convenient:

$$Z = |Z|e^{j\theta} = R + jX$$

$|Z|$ is the magnitude, $\theta = arg(Z)$, R the resistance, X the Reactance and j the square root of -1.

The use of the term impedance can sometimes be confusing and refers to the magnitude, the resistance or the reactance (Figure 2).

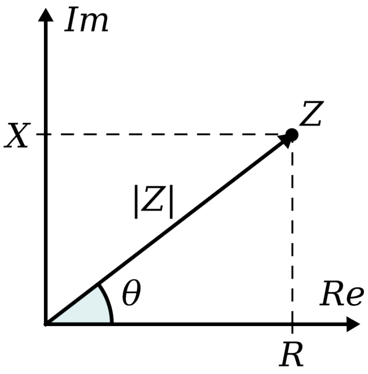

Figure 2:
Complex representation of impedance
Im y axis is the imaginary part where the Re x axis is the real one.

1.1.3 Neuronal impedance

We need to understand that investigating the impedance of a cell can have a great variety of meanings. As it is the general relation between the current and voltage, it could be seen as the neuron's transfer function. Depending on the type of experiment and most importantly the interpretation, impedance embeds all the changes in the neuron's electrical behaviour. By building more and more accurate circuits, comparing and fitting mathematical calculation to the data, it has proven itself to be a powerful tool. This has consolidated the idea that the neuron could be modelled as an electrical circuit.

In 1928 Kenneth S. Cole examined the impedance of the sea urchin *Arbacia Punctulata*'s eggs (Figure 3) to separate changes due to the membrane capacitance, the cytoplasm and the membrane resistance during fertilisation and early development (Cole, 1928). The same year Lawrence R. Blinks, based on work on the seaweed *Laminaria* (Osterhout, 1922) and his own, deduced from the impedance that: "The observed resistance change [to injury] is really a change in permeability of protoplasm to ions" (Blinks, 1928). Using impedance has played a major role in the understanding of membrane permeability to ions ever since. Ten years later, Cole and Howard J. Curtis examined the impedance changes during an action potential in the green algae *Nitella* (Cole & Curtis, 1938) and in the Giant squid axon (Cole & Curtis, 1939). They interpreted a transient change in the membrane's conductance during the spike. The same year Hodgkin and Huxley recorded this first intracellular action potential with the help of a glass micro-pipette (Hodgkin & Huxley, 1939). This major breakthrough permitted an access to the difference between the inside and the outside of the axon, whereas all the previous measurements were purely extracellular.

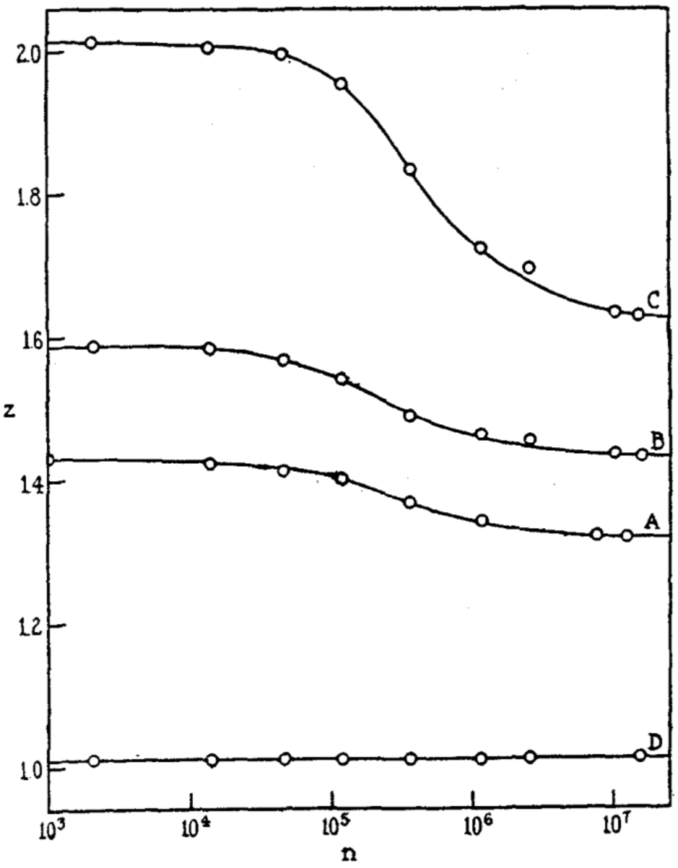

Figure 3:
Impedances of sea water Arbacia egg's suspensions
Impedance (Z) in arbitrary units) versus log frequency (n, cycles per second). (A-D) show different types of typical impedance profiles. From Cole, 1928.

In 1949 Cole and Marmont developed the voltage clamp technique (Marmont, 1949). With two pipettes and the use of a feedback amplifier they were able to control the membrane voltage at a defined value, and record the current necessary to "clamp" the cell. The ability to control voltage was used in the following years by Hodgkin and Huxley to develop experiments in order to dissect the changes in potassium and sodium conductances especially their time and voltage dependence (Hodgkin et al., 1952). These major breakthroughs led to their famous "ionic hypothesis" of the action potential (Hodgkin & Huxley, 1952). Their experiments did not involve any frequency analysis yet they were dissecting the ionic basis of the membrane impedance with respect to time, voltage and temperature.

In 1960, Wilfrid Rall reviewed different kinds of experiments of applied currents to the motoneuron in order to extract the soma time constant and a dendritic to soma conductance ratio. He conceptualised an experiment, and gave the theoretical response (Figure 4):

"*Essentially, the experiment would consist in applying a sinusoidal current across the soma membrane, at several different frequencies, and recording the oscillatory electrotonic potential that is developed across the soma membrane*" (Rall, 1960).

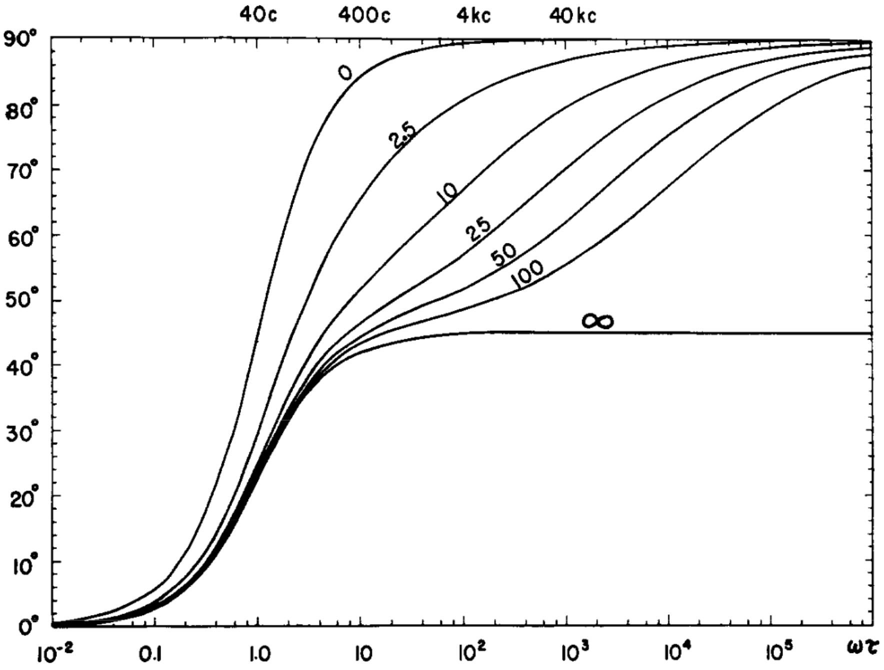

Figure 4:
Impedance simulations
"Theoretical relation between phase shift and frequency when a sinusoidal current is applied across the soma membrane, for [conductance] $\varrho = 0, 2.5, 10, 25, 50, 100$, and ∞. Zero phase angle implies a whole neuron impedance that is effectively a pure resistance; the 90° value corresponds to effectively pure capacitance. The $\omega\tau$ scale can be used for any τ [membrane time constant] value, the frequencies at the top of the figure apply when τ is 4 msec." From Rall, 1960

This was experimented in the cat spinal motoneuron by Nelson and Lux, 1970. It is interesting to point out the main focus on the phase angle to extract information from the system. As for the previous impedance work, done on the nerve, emphasis was put on the phase angle. As it gives an idea of whether the impedance is more resistive or capacitive, the two being orthogonal to one another.

Sabah and Leibovic, 1969, then Mauro et al., 1970, investigate an intriguing propriety of the giant squid axon's membrane. When injecting short and small pulses of currents into the axon, not enough to trigger an action potential, one can see some oscillation in the voltage response. As this phenomenon occurs under the action potential threshold, it is called subthreshold behaviour. On the impedance amplitude profile recorded from Mauro you can see a "bump" around 100 Hz (Figure 5). This "bump" represents the fact that for the frequencies centred around it, the membrane has a greater response than for the other frequencies. We say that the membrane has a preference range of frequency at which it resonates. This type of representation of the impedance is what we are nowadays most used to ; especially with this range of frequencies from 0 to 1 KHz.

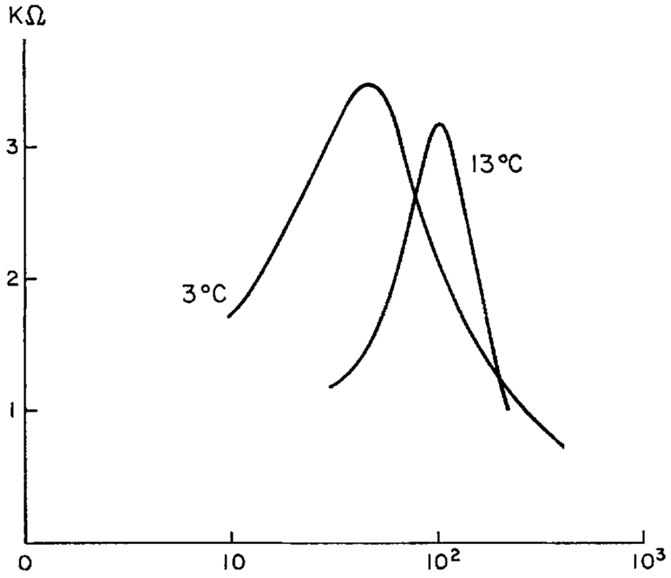

Figure 5:
Impedance amplitude profile of the Giant Squid axon
"Small-signal response of squid axon to variable frequency alternating current ("constant current" source). Note resonance and the dependence of resonant frequency on temperature. The values along the ordinate are given by the ratio of the peak voltage to the peak current for a 2 cm length of axon." From Mauro et al., 1970.

A few years later, in 1974, Rita Guttman injected Gaussian white noise generated current into the giant squid axon and got similar results (Guttman et al., 1974). She also was able to reproduce those results from a simulation based on the Hodgkin and Huxley model (Hodgkin & Huxley, 1952) (Figure 6). one can see a resonance around 200Hz. White noise is a signal in which all frequencies are represented with equal power. All the frequencies are probed at the same intensity and simultaneously. This technique was used several times for similar purpose (French & DiCaprio, 1975; Jahnsen & Karnup, 1994; Moore et al., 1988). Although white noise analysis can be a very powerful tool to assess neuron's properties, it has only been used a few times to asses the impedance profile.

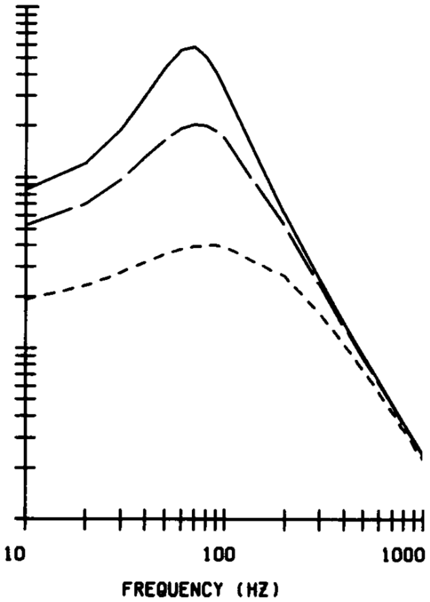

Figure 6:
Impedance profile simulations of the Giant Squid axon
"Power spectrum calculated from the linearized Hodgkin-Huxley equations. The solid curve shows standard conditions, temperature 6.3°C, leakage 0.3 mmho/cm2. The dashed curves show effect of increased leakage to twice and five times nominal value." From Guttman et al., 1974. *On the y axis, unit is unknown.*

In 1984 Gimbarzevsky introduced two major new aspects into the experimental procedure (Gimbarzevsky et al., 1984). He introduced the "ZAP" function, for *Impedance(Z) Amplitude Profile*, and used the Fast Fourier Transform (FFT) algorithm on the data. The "ZAP" function consists of a continuous function where the frequency on a sinusoid increases monotonically in time. Different to noise where the frequencies are all combined together, the "ZAP" function permits the probing of all frequencies independently from one another. As noted by Hutcheon, it is also visually informative. Without any data transformation, one can see approximately at which frequency range resonance occurs (Hutcheon & Yarom, 2000).

Work on the squid peripheral nerve (axon) unveiled the two voltage dependent conductances involved in the generation of the action potential. Then from work in the spinal motoneurones, it was assumed they had similar properties. In the same idea neurons from the central nervous system were seen as 'Platonic' as Rodolfo Llinas called them. Neurons were seen as simple threshold entities and the complexity was to come from the network (R. R. Llinás, 1988). But more and more diverse voltage-gated conductances were found with a great variety of behaviour ; with the idea that single neurons from the central nervous (CNS) system could have more intrinsic integration properties than expected.

With the advent of the patch clamp, invented by Sakmann and Neher, 1984, in conjunction with *in vitro* brain slicing techniques, it became easier to target neurons from the CNS of small mammals such as guinea pigs, rats and mice. Seeing oscillation at the network level, especially in the thalamus and the inferior olive, raised even more interest on sub-threshold oscillation and resonance (R. R. Llinás, 1988). Impedance profiles where resonance was seen were then recorded from NG-108 cultured cells (5-50Hz) (Moore et al., 1988), thalamic neurons (3-5Hz) (Puil et al., 1994), neocortical neurons (2-10Hz) (Gutfreund et al., 1995; Hutcheon et al., 1996) (Figure 7). Resonances are systematically voltage dependent, and the main goal of those studies was to dissect which conductances were involved.

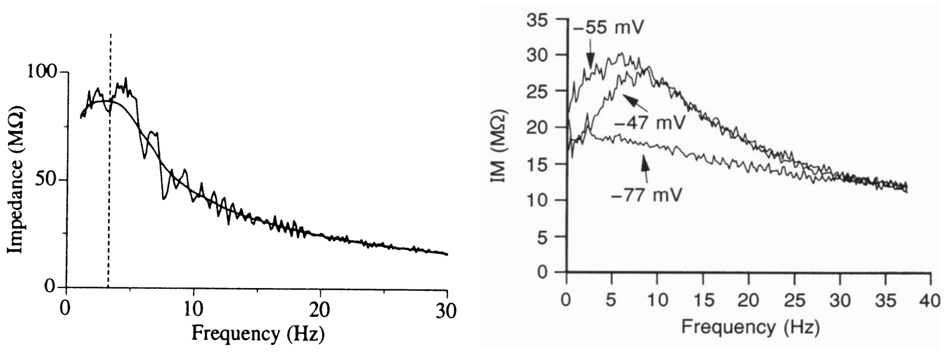

(a) Thalamic neurons from guinea Pigs. From Puil et al., 1994.

(b) Neocortical neurons from guinea Pig. From Gutfreund et al., 1995.

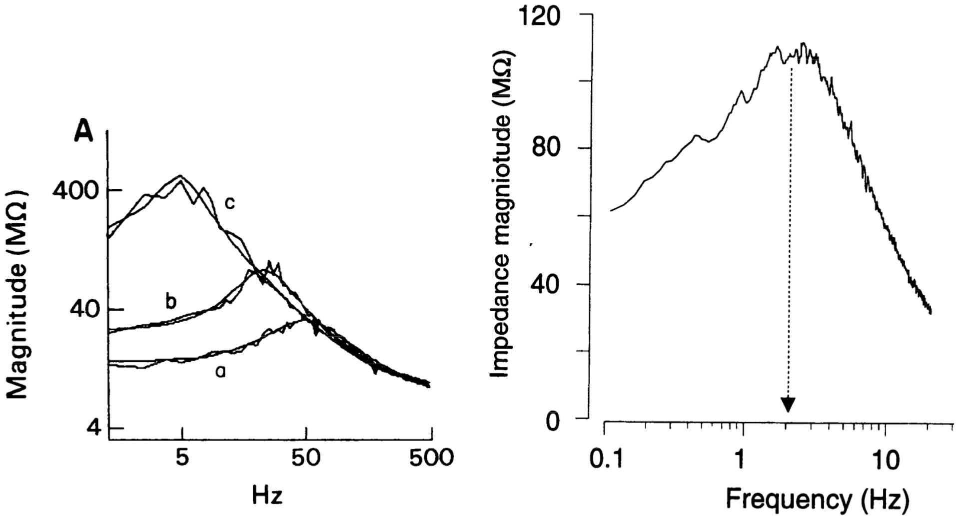

(c) Cultured neuronal NG-108 cells. *a,b,c respectivly -80mV,-60mV,-40mV.* From Moore et al., 1988.

(d) Neocortical regular neurons from juvenile rats. From Hutcheon et al., 1996.

Figure 7:
Mammalian neurons' sub-threshold resonance
A collection of reported sub-threshold membrane resonance in mammalian neurons. When reported the impedance's voltage dependency is reported. in (a) and (d) the dashed vertical line shows the resonant frequency.

1.2 Mechanisms of membrane resonance

1.2.1 Passive components

First, we need to look at the impedance profile of a simple parallel RC circuit (Figure 8). It acts as a low pass filter with a given cutoff frequency:

$$fc = \frac{1}{2\pi\tau_m}$$

In other words, the higher the input signal's frequency, above fc, the smaller the amplitude of the output signal.

The conductance involved is assumed to be constant over time and voltage. The only impact on the membrane's current is through the voltage difference towards the reversal potential, it only changes the driving force. The resulting current is usually called the leak current. At this stage the system is linear:

$$I_m(V_m) = g_{leak}(V_m - E_{leak})$$

Where $(V_m - E_{leak})$ *is the driving force and* E_{leak} *is the reversal potential of the leak channels ; which can also be assimilated to the resting membrane potential.*

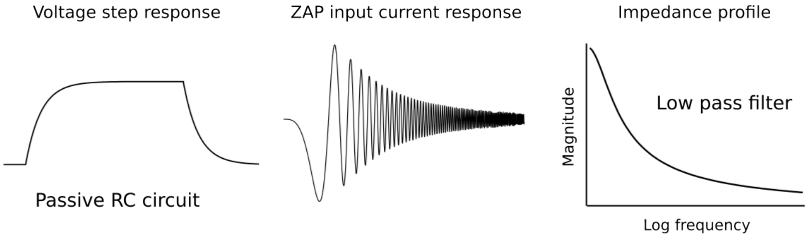

Figure 8:
Impedance of a RC circuit
Adapted from Hutcheon and Yarom, 2000.

The simplest form of probing approximately the passive properties is to apply a short voltage step. This is now a standard protocol done in almost all patch-clamp recordings, because it also gives information about the electrode resistance. When analysed in the time domain the step can be dissected in three periods (Figure 9).

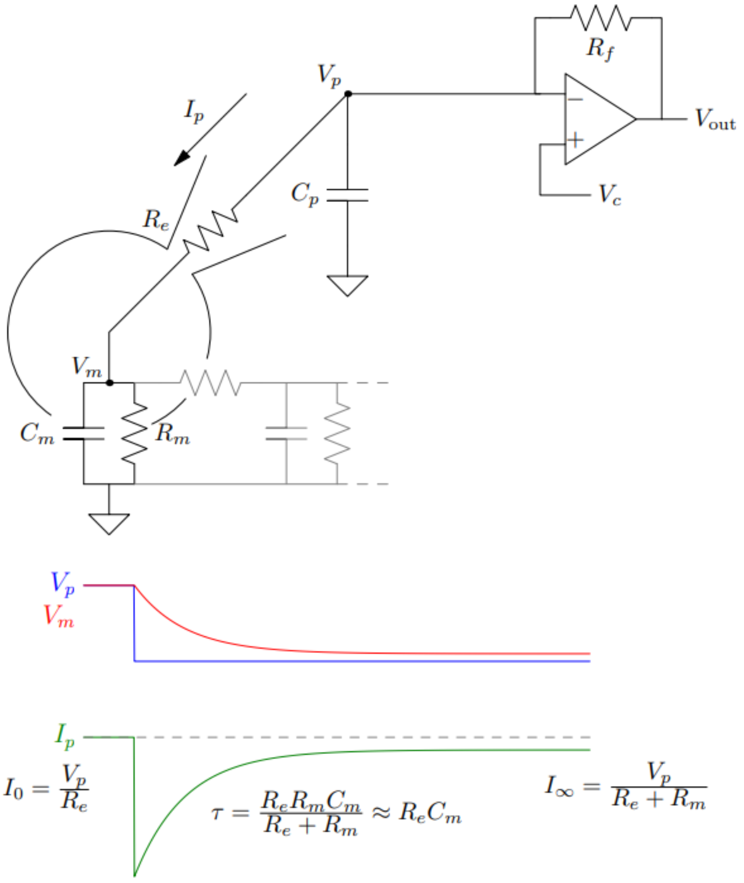

Figure 9:
The voltage clamp circuit

V_c is the command voltage, R_f the op amp feedback resistance insures the $V_p = V_c$. V_{out} the recorded voltage is then proportional to the pipette current I_p. R_e is the electrode resistance. When a voltage transient is applied at V_c the injected current can be separated in three phases. At the initial phase I_0, infinite current would be drawn by C_m and only R_e restricts the applied current. Then C_m charges exponentially and as $R_e << R_m$, τ can be simplified. At the equilibrium C_m draws no current and we can deduce R_m. C_p is the pipette capacitance, whose compensation is not treated here. From Barbour, 2018.

1.2.2 Active components

For some conductances the relation between V_m and the current is not linear. They are called "active" in contrast with the "passive" linear conductances. Hodgkin and Huxley were the first to build a mathematical model for voltage-gated channels that accounted for both voltage and time dependence (Hodgkin & Huxley, 1952). Their description is based on a "gate model" where the probability of opening of the channel is governed by one or several independent gating particles. A particle's probability of being in the active state y is described as follows (Johnston & Wu, 1994):

$$y(t, V_m) = y_0 - \left[\Big(y_0 - y_\infty(V_m)\Big)\Big(1 - e^{-t/\tau_y(V_m)}\Big)\right]$$

$$y_\infty(V_m) = \frac{\alpha_y(V_m)}{\alpha_y(V_m) + \beta_y(V_m)}$$

$$\tau_y(V_m) = \frac{1}{\alpha_y(V_m) + \beta_y(V_m)}$$

Where $\alpha_y(V_m)$ and $\beta_y(V_m)$ are the rate coefficients for the transitions to the active and inactive states, respectively:

$$\alpha_y(V_m) = \alpha_0 e^{\delta z F V_m / RT}$$

$$\beta_y(V_m) = \beta_0 e^{-(1-\delta) z F V_m / RT}$$

R is the gas constant, F the Faraday constant, T the absolute temperature and z the ion valence.
δ is a factor (0-1) of asymmetry of the voltage energy barrier between the cell's membrane.

We then have the following conductance of the ion selective channel:

$$g_{ion} = Y_{ion}(t, V_m)\bar{g}_{ion}$$

$$Y_{ion}(t, V_m) = \big[y_{ion}(t, V_m)\big]^P$$

Where $\bar{g}_{ion}$ is the maximum conductance and P is the number of independent gating particles involved in the process.

One can appreciate that by inverting the active and inactive states the equations can correspond to an activation (opening) or deactivation (closing) of the channel. The two processes can be combined within the same general probability description:

$$Y(t, V_m) = y_{act}(t, V_m)^{P_{act}} y_{deact}(t, V_m)^{P_{deact}}$$

Hodgkin and Huxley's model had a sodium and a potassium conductance fitted to the squid axon action potential. The model reproduced the action potential astonishingly well (see 2.1.1). Since then more and more voltage-gated channels were discovered among neurons. To date, the gated model has proven to be general and robust to describe channel behaviour. Voltage-gated channels display various phenotypes in terms of ionic selectivity, voltage threshold and activation/inactivation kinetics. Each type of neuron will have its own signature and compartmentalisation (dendrites, soma) of voltage-gated channels. How a channel impacts the cell's impedance and could potentially create resonance is beautifully explained by Hutcheon and Yarom "rules of thumb" for creating a subthreshold resonance (Hutcheon & Yarom, 2000) (Figure 11):

1. Passive components are low pass filters governed by the time constant (τ_{leak}) resulting from the parallel leak conductance.
2. A current that is activated by a voltage change and which will counteract (rectify) the voltage change. This will act as a high pass filter (Figure 10).
3. The active current time constant must be longer than τ_{leak}. So that it creates a band pass filter.

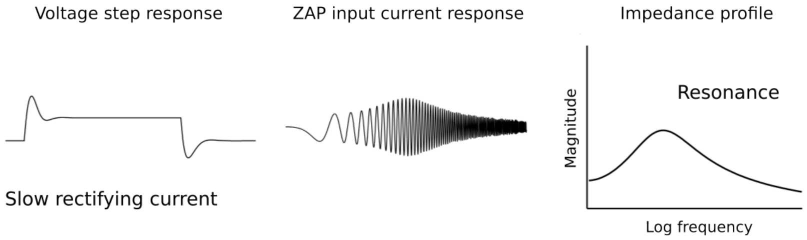

Figure 10:
Slow rectifying current as high pass filter
From Hutcheon and Yarom, 2000.

Therefore, with those rules, resonance arises from a band pass filter that diminishes the impedance around its boundaries. There are two major slowly activated rectifying currents known to be involved in membrane resonance:

- The outwardly rectifying potassium (K) current: I_K. Activated by depolarisation. With a reversal around - 90 mV (Hille, 2001)
- The hyperpolarisation (h) activated current I_h. Inwardly rectifying partially non-selective cationic current.

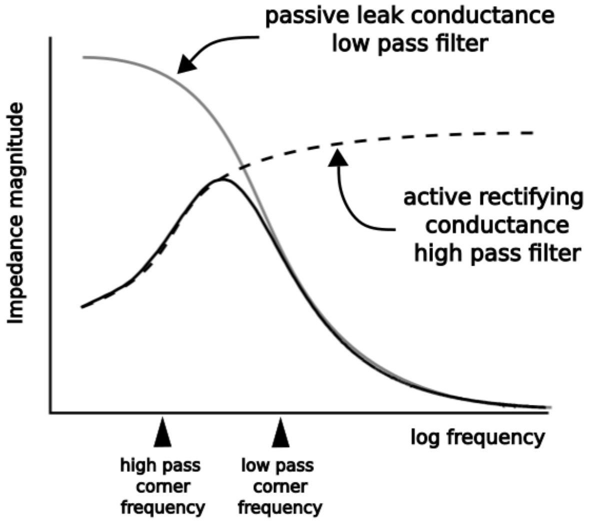

Figure 11:
How to create a resonance
The combination of the passive low pass filtering and active high pass filters governed by voltage-gated channels. Adapted from Hutcheon and Yarom, 2000.

A partially non-selective cationic current means that the channels are permeable to mainly Na^+, K^+ but with a slight difference in selectivity that brings the reversal potential to around -40 mV (Roth & Häusser, 2001). Another way of understanding how conductances can impact the resonance, is looking at the activation curve along the membrane voltage with respect to their reversal potential (Figure 13).

We understand that resonance is based upon the interplay between the neuron's passive properties and its voltage-gated channels ; thus the frequency and amplitude of a resonance is voltage dependent. One can imagine that almost any neuron can exhibit some resonance in a particular context (Richardson et al., 2003).

1.2.3 Resonance and oscillation

Some neurons exhibit intrinsic (pace-making) membrane oscillation, this phenomenon can arise when an amplifying current interacts with a resonant one. When the reversal potential of a channel corresponds to its voltage at which it is fully activated, voltage fluctuations will be enhanced thus amplified (Figure 13). The following are the channels best known to be suitable for amplifying resonance:

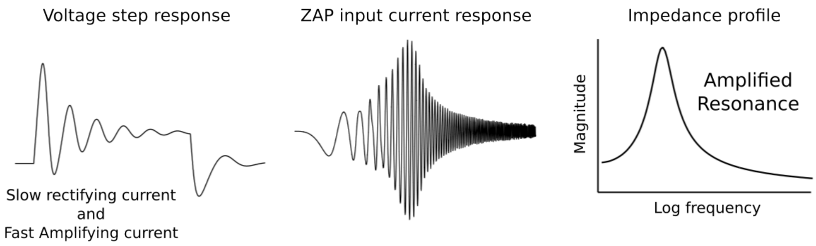

Figure 12:
Amplified resonance
Adapted from Hutcheon and Yarom, 2000.

- Persistent Na^+ channels (I_{NaP}). With a reversal around + 55mV (Richardson et al., 2003)
- Current mediated by NMDA activate channels (I_{NMDA}). There relief of Mg^{2+} block activates them only when the membrane is depolarised, and its reversal is around 0 mV (cationic).
- The dihydropyridine-sensitive high-threshold Ca^{2+} (I_L). With a reversal around + 50mV (Hille, 2001)

The presence of an amplifying current does not necessarily mean that the neuron's membrane potential will oscillate. For example, neurons from the somatosensory cortex of rats have I_h and I_{NaP} and some neurons of the frontal cortex of guinea pigs, I_K and I_{NaP} (Hutcheon & Yarom, 2000). Neither of them show oscillations, but they do have amplified resonance at low frequencies (Figure 12).

Neurons from the inferior olive (R. Llinás & Yarom, 1986) and thalamocortical neurons (Puil et al., 1994) exhibit pace-making membrane oscillation. One channel is mainly responsible for this:

- Low-threshold Ca^{2+} channels (I_T). It has an inactivation process that produces resonance and an activation one that amplifies it. Combined in one channel, at the right membrane voltage ('window current') the two processes create self sustained oscillation around 5Hz. With a reversal around + 50mV (Hille, 2001)

We can now say that neurons show various ways of integrating external information in the frequency domain. This integration depends on the membrane voltage and the types of current involved. We have seen how the input of a cell changes its membrane voltage. Nevertheless, neurons mainly communicate through the generation of action potential. Thus, the key question now is to understand how membrane potential resonance interacts with the firing output of neurons, especially in the frequency domain.

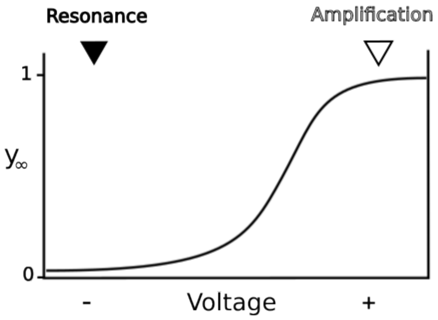

(a) Activated by depolarisation.

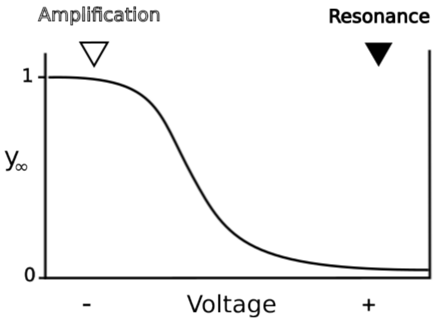

(b) Activated by hyperpolarisation.

Figure 13:
Voltage-gated channels' activation profiles
y_∞ as a function of voltage for channels activated by depolarisation a) or hyperpolarisation b). Arrows represent the reversal potential. Filled triangles are placed where the channel would produce rectifying currents and then resonance if it combined the activation profile and the reversal potential. The open triangles are placed where amplification would occur. Adapted from Hutcheon and Yarom, 2000.

2 Firing Resonance

2.1 The Neuron's output

2.1.1 The Action Potential

Neurons can communicate to each other in various ways:

- Synaptic communication. A presynaptic action potential triggers the release of neurotransmitters that will activate postsynaptic receptors with different time scales:
  - At a fast scale ($\sim$ 1 ms) channels will open changing the local membrane conductance and affecting its voltage.
  - At slower timescales, spillover (Szapiro & Barbour, 2007) and metabotropic receptor can also affect signalling, including by modulating plasticity.
- Non synaptic communication. Electrically, via gap junctions or in an ephaptic manner. Chemically via neuromodulation (volume transmission).

However, the present study will be restricted to fast synaptic communication, and especially the high-frequency components.

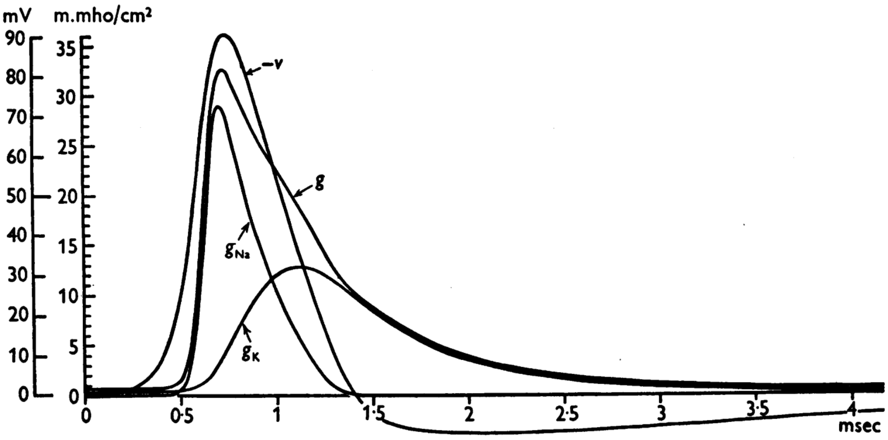

Figure 14:
Hodgkin and Huxley's action potential numerical solution. Components of membrane conductance (g) during propagated action potential. The membrane voltage is referred to the intracellular resting potential (as opposed to the modern convention $V_{in} - V_{out}$). From Hodgkin and Huxley, 1952.

The action potential is considered the "unit" of communication between neurons. The generation of an action potential is based on a voltage-dependent auto-regenerative process. At a certain depolarised voltage threshold, fast-activating sodium channels will open, depolarise even more the membrane, and so on. This creates a sharp onset. Those channels are also fast to inactivate, accompanied by the slower activation of potassium channels triggered by the depolarisation (delayed rectifier) induced by the sodium channels. Both of those processes will hyperpolarise the membrane and end the action potential with an overshoot, the after-hyperpolarisation (AHP) (Figure 14). This was discovered and described by Hodgkin and Huxley as follow:

$$I_{AP}(V_m, t) = g_K(V_m(t) - E_K) + g_{Na}(V_m(t) - E_{Na})$$
$$g_K(t, V_m) = \bar{g}_K n^4(t, V_m)$$
$$g_{Na}(t, V_m) = \bar{g}_{Na} m^3(t, V_m) h(t, V_m)$$

Where m and n are activation probability and h inactivation as described above in 1.2.2, for fitted values see (Hodgkin & Huxley, 1952)

2.1.2 Models of a spiking neuron

To have a general equation describing a spiking one compartment neuron, Hodgkin and Huxley combined the passive properties, capacitance and leak, with the conductances involved in the action potential:

$$C_m \frac{dV_m}{dt} = -I_{leak} - I_{Na} - I_K$$
$$I_{leak} = g_{leak}(V_m - E_{leak})$$
$$I_{Na} = g_{Na}(V_m - E_{Na})$$
$$I_K = g_K(V_m - E_K)$$

This was the first conductance-based model. The denomination conductance-based concerns any models that explicitly incorporate channel conductances rather than voltage-independent voltage or current changes; the large voltage excursions occurring during the action potential would render the voltage-independent approximations quite inaccurate. Other conductances than sodium and potassium can be added to such models, especially to give a more accurate description of the membrane sub-threshold dynamics. Their parameters can also be changed to fit more accurately some neuronal spikes, for example the Wang and Buzsáki model (WB) is fitted for fast-spiking interneurons (Wang & Buzsáki, 1996).

Conductance-based models are good representations of neurons. However, especially if we want the neurons to connect to each other in networks, the analytical solutions to the system become complicated to elucidate.

The idea of a simple “integrate and fire” (IF) neuron was introduced long before Hodgkin & Huxley, by Lapicque, 1907. It consists of:

- A simple one compartment passive neuron, parallel RC circuit.
- An arbitrary voltage threshold at which an action potential is generated.
- A reset voltage after the action potential.

It is a very simple yet powerful model and accurate for many applications (Abbott, 1999). As the only conductance in the model is the one due to the leak current, the model is called the “leaky integrate and fire” (LIF). The membrane voltage is then described as follow:

$$C_m \frac{dV_m}{dt} = -g_{leak}(V_m - E_{leak})$$

An interesting addition was made to the LIF by Fourcaud-Trocmé et al., 2003. In order to keep the simplicity of the LIF, but gain some complexity on the generation of the action potential, an exponential component mimicking the onset and generation of the action potential was added. The model is then called the “exponential integrate and fire” (EIF):

$$C_m \frac{dV_m}{dt} = -g_{leak}(V_m - E_{leak}) + \psi(V_m)$$
$$\psi(V_m) = g_{leak}\Delta_T exp\left(\frac{V_m - V_T}{\Delta_T}\right)$$

Where V_T *is the action potential threshold and* Δ_T *the “slope factor” controlling the sharpness of the spike.*

The exponential part simplifies the fast activation of the sodium channels. When the exponential makes the voltage too depolarised, the calculation is arbitrarily stopped and reset at a fixed voltage like in the LIF (Figure 15).

2.2 Fast Population encoding

2.2.1 Synaptic noise and filtering

We have seen that the passive components of a cell’s membrane act as a low-pass filter on external inputs, governed by the membrane time constant. The intuition would be that the output firing rate would follow this low pass filtering from the membrane. The question addressed here is to understand how external input are translated in terms of firing.

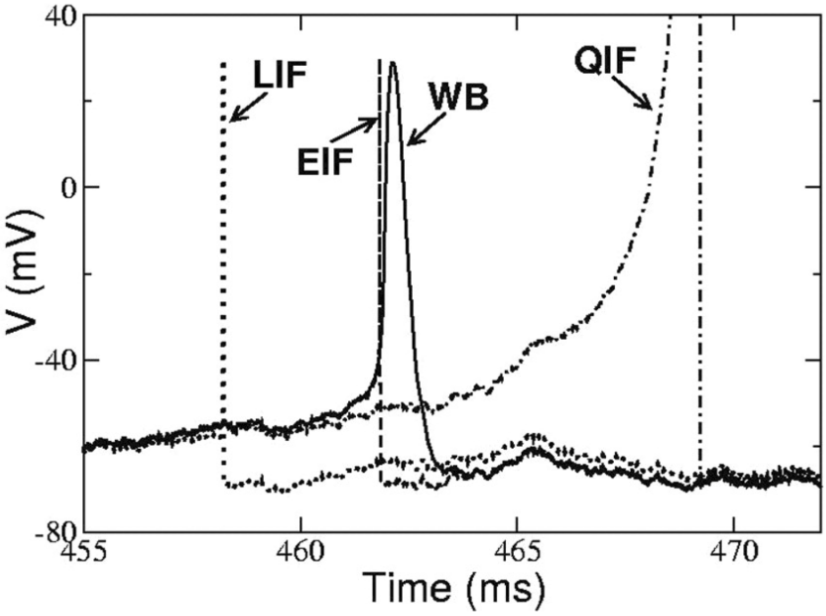

Figure 15:
Simulation of LIF, EIF, QIF and the WB neuron.
For the same input, the LIF is early and the QIF late compared to the EIF and the WB (Wang and Buzsáki model) which have similar spike times. QIF is for Quadratic IF. From Fourcaud-Trocmé et al., 2003.

We may need to clarify here what "translated into firing" means. The general "experimental" procedure that will be explored is somehow similar to the concept of impedance. The probed system is a neuron that is firing tonically at a fixed rate. A periodic current, ususally a sine wave at given frequencies, is injected into a neuron to perturb its firing. We can see the parallel made with impedance, in the same way we are looking for a "transfer function" from input to firing response in the frequency domain. The goal here is to compare the amplitudes and phases between the input and output firing, and attribute any filtering or resonance effects to the neurons.

Another important point needs to be discussed. Having a neuron's response to a periodic input can be understood as the mean response of the cell to one cycle, or as the response of an identical population of this neuron to one cycle of the input. This gives the information on how fast a population can transmit episodic information. On the other hand, it also answers the question of how the single neuron is synchronised to the periodic input, which is commonly called phase-locking.

Using the LIF as a model, with a finite size population, there is an effective low-pass filter due to the membrane time constant (Knight, 1972). If the homogenous population is “large” enough and in the best case infinite, then the output firing renders the input current with no filtering (Gerstner, 2000). Of course such a population is not biologically plausible. However, in a reduced size population, transfer of information of high frequencies can be improved by adding white noise to the input, making the population’s firing heterogeneous (Gerstner, 2000; Knight, 1972). In a perhaps more intuitive way, if the firing rate of each neuron is different, the chance to have neurons near threshold is higher and the speed of response also becomes higher (Gerstner, 2000).

In the absence of noise, the neuron’s frequency response is “polluted” by its firing rate frequency and harmonics. Adding perturbations also reduces the population firing rate resonance and its harmonics.

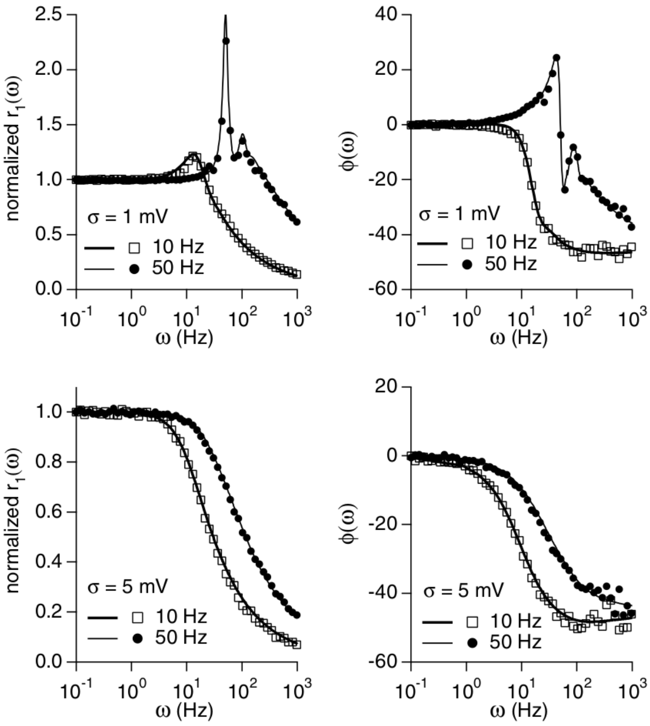

Figure 16:
Firing rate and noise effects on LIF frequency response.
$r_1(\omega)$ and $\phi(\omega)$ are respectively the amplitude and phase of the firing rates’s Fourier transform. Solid lines are analytical predictions for each firing rate (10 and 50 Hz). σ is the amplitude of the noise. $\tau_s = 0$. Amplitude is normalised over $r_1(0.1Hz)$. From Brunel et al., 2001.

Fourcaud-Trocmé and Brunel detailed these results raising an interesting problem: the white noise is not representative of the noise a neuron receives in vivo. The noise is filtered by the decay time of the postsynaptic channels (Brunel et al., 2001; Fourcaud & Brunel, 2002). They defined noise in the following manner:

$$\tau_s \frac{dI_{noise}}{dt} = \eta(t) - I_{noise}$$

Where τ_s represent the decay time constant of channels, $\eta(t)$ is a Gaussian white noise variable in which σ controls the amplitude

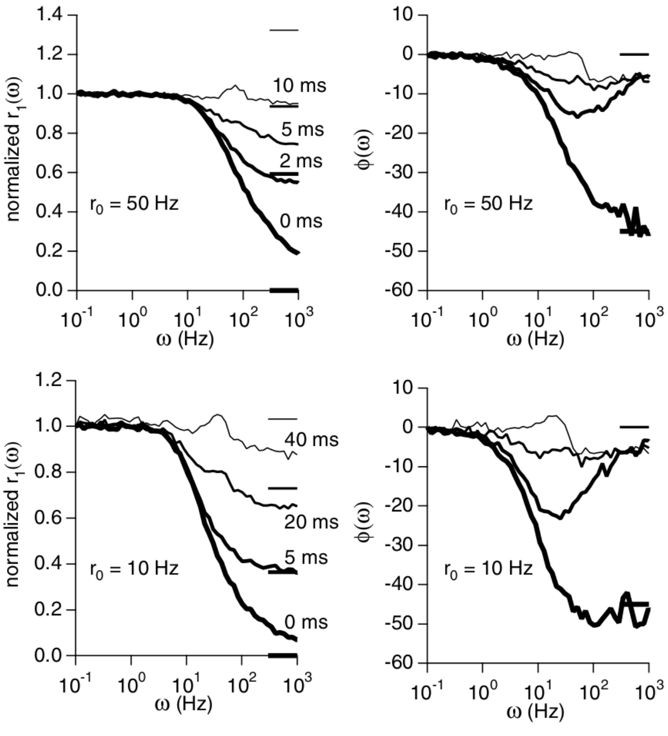

Figure 17:
Noise's τ_s effects on LIF frequency response.
$r_1(\omega)$ and $\phi(\omega)$ are respectively the amplitude and phase of the firing rates's Fourier transform. The different lines represent different τ_s. r_0 is the firing rate. Amplitude is normalised over r_1(0.1Hz). From Brunel et al., 2001.

With the more realistic noise, the signal gets filtered at rather low frequencies. We can see in Figure 16 the clear peak of resonance to the firing rate with low noise (σ = 1mV) that is smoothed out when the noise is greater (σ = 5mV). The firing rate seems also to shift the cutoff frequency to higher levels (Figure 16 and Figure 18A). However, the time constant τ_s has tremendous effects on the transfer of information. Indeed, in Figure 17 we clearly see that elevating the decay time constant restores transfer of information. Those time decays can be related to the realistic time constants of posynaptic channels (Fourcaud & Brunel, 2002):

- $\mathrm{GABA_A}$: 5-10 ms
- NMDA: 50-100 ms

Once again in certain conditions is it possible for a neuron to transfer the input without any filtering up to high frequencies, but counter-intuitively by raising the decay time of the synaptic noise.

Fourcaud-Trocmé and Brunel continued investigating fluctuating inputs by building the exponential IF (EIF), and examining its responses (Fourcaud-Trocmé et al., 2003). The EIF has a similar frequency response compared to a conductance based model, which is a low cutoff frequency (Figure 18). One major variable of the EIF is Δ_T which governs the sharpness of the spike initiation. On Figure 18 we can appreciate the effect of Δ_T on the cutoff frequency combined with the noise filtering. The smaller Δ_T the sharper the spike will be and the greater the cutoff frequency, when the "slow" noise is present. Being more realistic but simpler to analyse and implement than a conductance based model, the EIF is seems to be a promising model.

2.2.2 Experimental frequency responses

Köndgen et al., 2008, investigated this idea in neocortical neurons. They used small signal perturbation to assess the linear regime of the neurons. Using an Ornstein-Uhlenbeck stochastic process to generate noise with a zero mean, mimicking synaptic noise, they injected small sinusoid signals given frequencies from 1 to 1000 Hz while adding the noise. Taking as a population the combined data of all the neurons, the noise expanded the information transfer up to 200Hz (Figure 19). This cutoff frequency is higher than expected by the simulations on the EIF ($<$ 100 Hz). It could suggest faster rise of the action potential (Naundorf et al., 2005). This study also tested changing the time correlation in the noise (the τ_s in Brunel et al., 2001), and it did not have significant effects on the cutoff frequency.

Tchumatchenko et al., 2011 conducted a similar experiment to Köndgen et al., 2008. They compared "slow" and "fast" synaptic noise compared to *in vivo* data (Figure 20). Changing the noise dynamics had an impact on the population response, where "faster" noise induced greater filtering. The *in vivo* data had a frequency profile in between the two types of noise, showing that biological synaptic noise could be close to the artificial one. Also, in the two previous experiments noise was additive meaning it was added to the input, inducing changes in the mean input. Studies on multiplicative noise, inducing changes in the input's variance, showed that it could push up almost to 1 kHz the transfer's bandwidth (Boucsein et al., 2009; Lindner & Schimansky-Geier, 2001).

2.3 From sub-threshold to firing

2.3.1 From theory

Richardson et al., 2003 established the theoretical basis to understand how sub-threshold membrane resonances and oscillations could translate to the firing output of a neuron. They first characterised the sub-threshold behaviours (Figure 21) with a simple two-variable model. They combined the two variable models with an integrate and fire mechanism to generate what they called a Generalized Integrate and Fire model (GIF). The GIF was then compared to conductance-based models.

When analysing oscillating-input experiments, two types of firing resonance are to be differentiated. Assuming the neuron is spiking at a stable pace (r_0 in Figure 22), when the input frequency is the same or a harmonic, the resulting modulation of firing appears to be enhanced, thus a resonance (Brunel et al., 2001). The second one may be present or not and results from the possible membrane potential resonance (f_R in Figure 22). If no or low amplitude noise is added to the input, the firing rate resonance dominates. With strong noise which will result in the neuron firing in an almost Poisson manner, with unstable firing rate, the resonance from the sub-threshold regime appears (Figure 22). It is important to distinguish those two resonances from stochastic resonance which is generated by noise amplification. Especially for the sub-threshold-linked firing resonance which "appears" when noise is increased (Richardson et al., 2003).

2.3.2 To experiments

In the enthorinal cortex, two types of cells were investigated, stellate and pyramidal cells. Stellate cells have a membrane potential resonance, whereas pyramidal cells do not. Responses to injection of a different kinds of filtered noise, in the sub and supra threshold regime, showed continuity in the responses between the two (Engel et al., 2008; Erchova et al., 2004; Haas & White, 2002).

However, a study from Carandini et al., 1996 showed dissimilarity in a visual cortex regular-spiking neuron. They exhibit a low-pass filtered impedance with no resonance, but their firing profile shows amplified responses when the frequency rises until a cutoff (Figure 23) (Carandini et al., 1996). Similar results were found in the Oriens-lacunosum moleculare interneurons in the hippocampus (Kispersky et al., 2012).

In the striatum, Beatty et al., 2015 investigated four cellular types for their firing resonance. Three types of interneurons: fast-spiking, low-threshold spiking and cholinergic. They all showed membrane potential resonance at different frequency bands. The low-threshold spiking (Figure 24a) and the cholinergic interneurons had matching frequency preferences between impedance and firing profiles, whereas the fast spiking had both frequency preferences but at different bandwidths. The fourth neuronal type tested was the medial spiny neuron, it had no sub-threshold resonance and showed clear firing rate resonance (Figure 24b). Although the low-threshold exhibits sub-threshold resonance in around 20-40 Hz, from Figure 24a it is unclear what resonance we are looking at. There seems to be a rather clear firing rate resonance at least for higher firing rates (> 20 Hz).

Broicher et al., 2012 investigated the effects of changes in conductances and firing rates on the firing frequency profiles of hippocampal CA1 pyramidal neurons. Interestingly, changing background conductance, via a dynamic clamp, had opposite effects between sub and supra threshold regimes (Figure 25). Also elevating the firing rate changed the firing profiles and made the cells behave as band-pass filters with a higher frequency range than at low firing rates. Once again, discrepancies between impedance and firing frequencies profiles were observed. Other work has focused on neocortical neurons (Brumberg & Gutkin, 2007; Higgs & Spain, 2009) with the same overall conclusion that the sub-threshold behaviour is not sufficient to explain the firing resonances. Mechanisms in the spike initiation and after-hyperpolarisation are interesting paths to explore (Higgs & Spain, 2009), but no general mechanism has been identified yet.

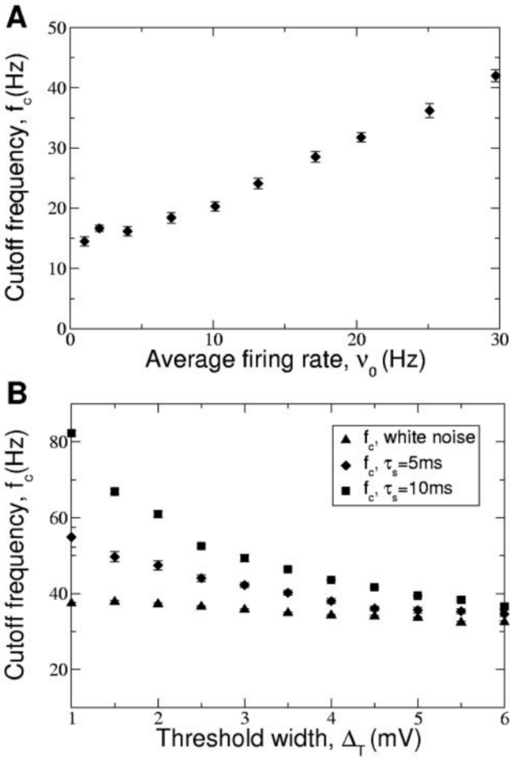

Figure 18:

EIF simulation with fluctuating input and noise.

A: effect of the firing rate on the EIF filtering cutoff frequency with white noise. EIF parameters were fitted to match a fast-spiking neuron conductance based model (Wang & Buzsáki, 1996). $\alpha = 8$ mV.

B: Effect of the EIF spike sharpness (Δ_T) on the cutoff frequency for an average firing rate of 24 Hz. $\alpha = 8$ mV.

From Fourcaud-Trocmé et al., 2003.

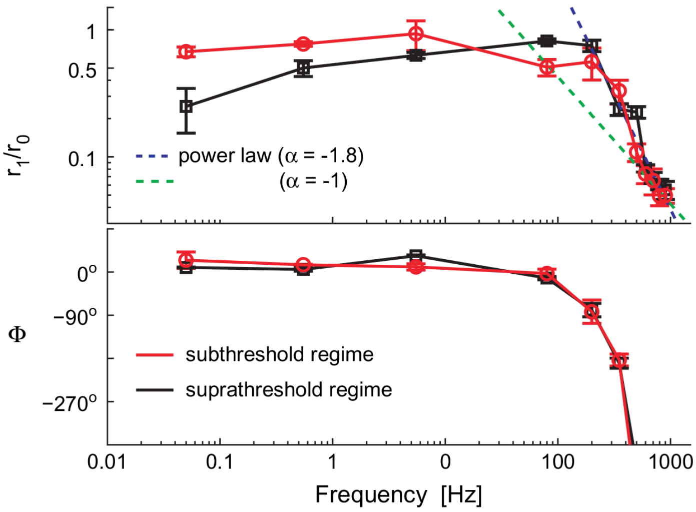

Figure 19:
Fast encoding of cortical neurons to oscillating input.
r_1/r_0 represents modulation of the firing rate. r_0 is the firing rate and r_1 the modulation induced by the oscillating input. Supra-threshold regime (red) is low amplitude noise where sub-threshold (black) is high amplitude noise. The power law relationship ($r_1 \sim f^\alpha$) in the high-frequency response is consistent with Brunel et al., 2001's predictions. From Köndgen et al., 2008.

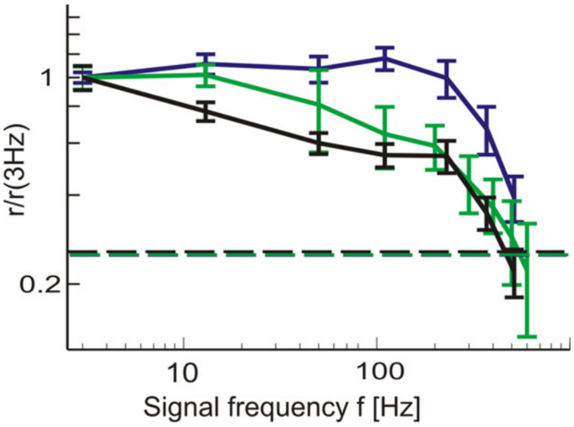

Figure 20:
Synaptic noise in cortical neurons' firing response.
Frequency response to oscillating input with slow (blue) or fast (black) synaptic-like noise. In green is in vivo experiments with no noise added. r is the vector strength quantifying the encoding at each frequency, normalised here. From Tchumatchenko et al., 2011.

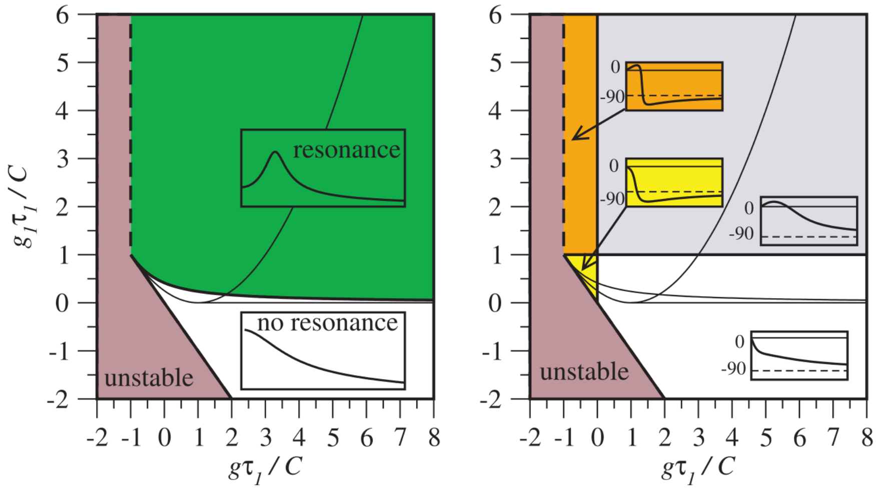

Figure 21:
Sub-threshold behaviour of a two-variable model.
Representing the different behaviours function of the effective leak ($g_1\tau_1/C$) and the coupling between the two variables ($g\tau_1/C$). On the left panel amplitude of the impedance and on the right phase of the impedance. From Richardson et al., 2003.

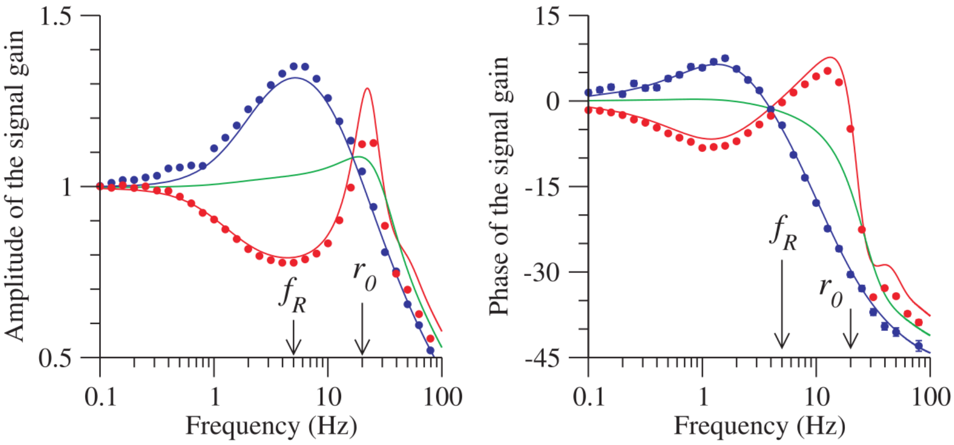

Figure 22:
Unveiling of firing resonance with noise in GIF.
Frequency response of a GIF in two configurations: high (blue) and low (red) amplitude noise. The solid lines are the theoretical predictions and dots numerical results. the green lines represent an intermediate noise amplitude. r_0 is the firing rate and f_R the sub-threshold resonance frequency. From Richardson et al., 2003.

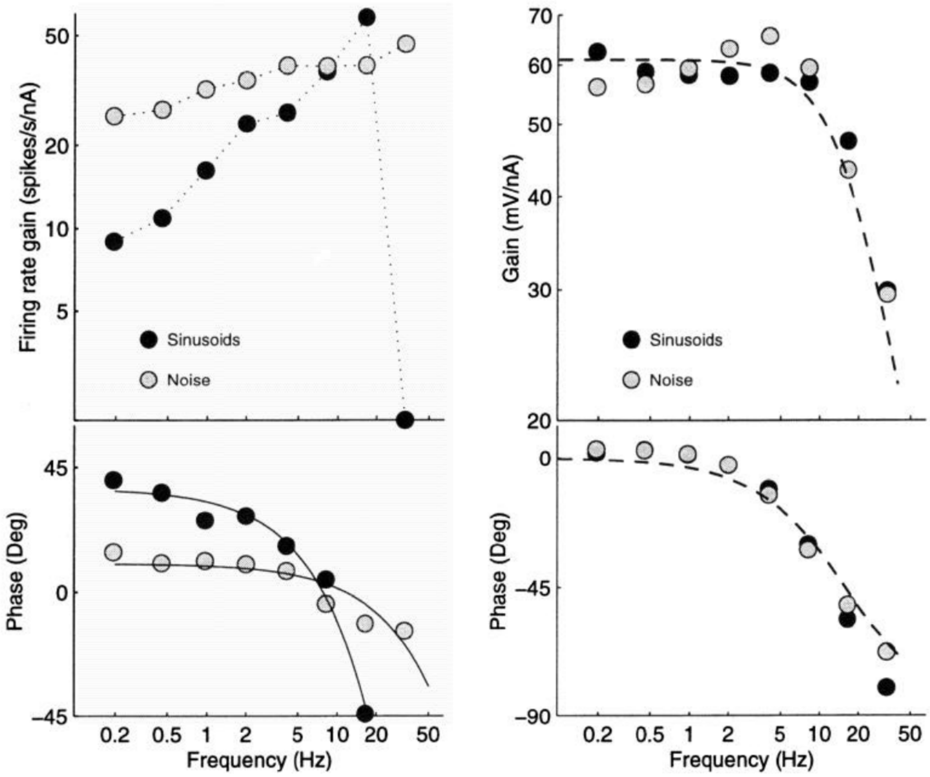

(a) Firing response. **(b)** Membrane response.

Figure 23:
Unmatched firing and impedance responses.
Firing (a) and membrane potential response to pure sinusoidal (black) or noise (grey). The noise being composed of a combination of 8 sine waves. Solid line is the phase of the firing profile in a fit. The dashed lines are the predictions of a RC circuit. From Carandini et al., 1996.

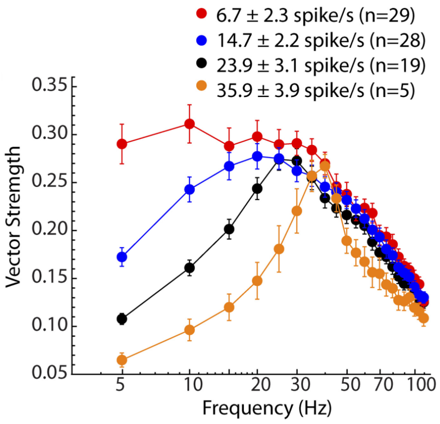

(a) Low threshold spiking neuron.

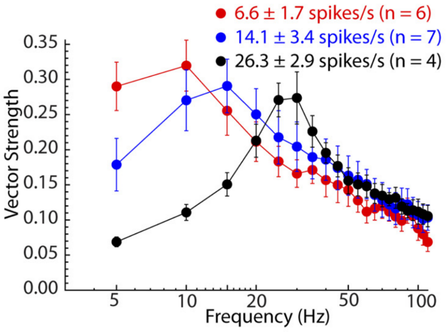

(b) Spiny neuron.

Figure 24:
Frequency response profile of striatal neurons.
Neuronal responses to a barrage of synaptic currents and background conductances at different firing rates. From Beatty et al., 2015.

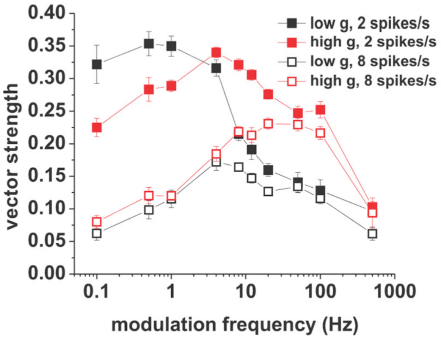

(a) Firing frequency profile.

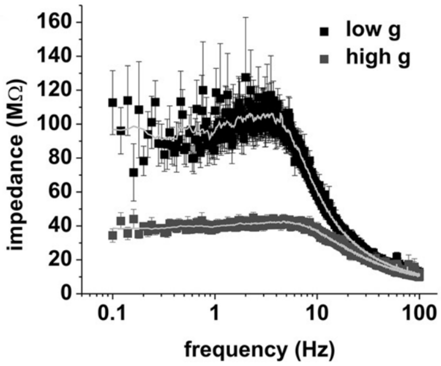

(b) Impedance amplitude profile.

Figure 25:
Frequency response in CA1 pyramidal cells.
Response to oscillating inputs (cosines) combined with background conductance noise of either low or high amplitude. The conductances were simulated via a dynamic clamp. From Broicher et al., 2012.

3 The Purkinje cell

As a major part of the hindbrain, the cerebellum is mainly known to play a key role in learning and controlling motor skills, as a relay point between descending cortical and ascending peripheral sensory information. The major input of the cerebellum comes from the mossy fibres conveying all sorts of information from motor command copies to contextual information and sensory inputs. Composed of a cortex and deep nuclei, the “simple” cerebellar circuit starts from the mossy fibres converging information onto cortical granule cells, diverging again onto the Purkinje cells integrating tremendous amounts of information with over $170,000$ connections each (Napper & Harvey, 1988). Purkinje cell axons exit the cortex to contact the deep nuclei, which are the output of the cerebellum. A second input to the cerebellum comes from the inferior olive which projects climbing fibres onto the Purkinje cells. A remarkable fact is that each Purkinje cell is connected to only one (rarely two) climbing fibre. The cerebellar cortex is organised in the three layers (from internal to external):

- The granule cell layer: where the granule cell somata are located.
- The Purkinje cell layer: theit somata aligned in a single cell layer, with their axons departing across the granular layer toward the nuclei and theit dendrites ascending into the upper molecular layer.
- The molecular layer: where all the granule cells’ projecting axons organised in parallel (the parallel fibres) contact Purkinje cell dendrites. Two types of inhibitory interneurons (basket and stellate cells) are located in this layer, mainly innevervating Purkinje cells.

The Purkinje cells are usually considered as the integrating cornerstones of the cerebellar circuit. Especially in the cerebellar learning theories of Marr (Marr, 1969) and Albus (Albus, 1971) that hypothesised synaptic plasticity at the granule cell–Purkinje cell synapse. This was eventually confirmed experimentally by Ito, showing long-term depression at the synapse (Ito et al., 1982). Purkinje neurons are inhibitory neurons, releasing GABA (γ-aminobutyric acid). Nearby Purkinje cells tend to synchronize themselves and converge on nuclear targets with a 40:1 ratio (Person & Raman, 2012). Their synchrony is still not well understood and could result from their recurrent connections between them and/or synchronised input from the parallel fibres (de Solages et al., 2008). De Solage et al also recorded high-frequency oscillations (~ 200 Hz) in the Purkinje cell layer and hypothesised it was a result of their synchrony.

The Purkinje cell is a complex neuron in various ways. First it has one of the most dense dendritic trees amongst the diverse neurons of the brain (Figure 26). Secondly it exhibits two types of somatic spike, the simple and the

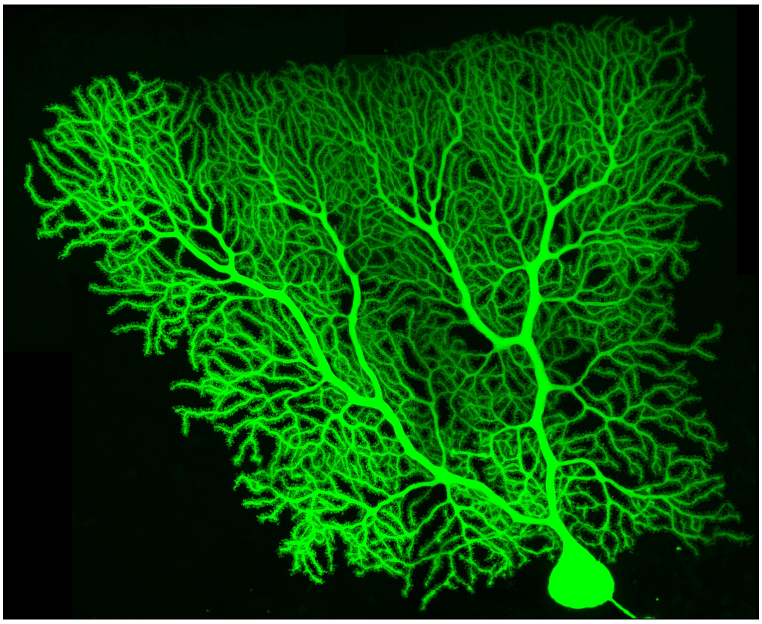

Figure 26:
The Purkinje cell.
Labelled with intracellular biotin, from an adult rat cerebellar slice. Picture from Boris Barbour.

complex spike. The simple spike is a standard action potential, whereas the complex spike is exclusively triggered by the climbing fibre stimulation and is characterised by a longer duration than the simple spike and its succeeding wavelets. The Purkinje cells's dendrites can also support specific calcium spikes (R. Llinás & Sugimori, 1980b).

The cell exhibits different firing regimes and patterns. Although "in vivo" recordings over long periods of time have reported an overall highly irregular firing, "in vitro" recordings of cells can exhibit short periods of regular firing and bursts (Shin et al., 2007). Also, when depolarised Purkinje cells reach a plateau and stop firing due to inactivation of sodium channels (R. Llinás & Sugimori, 1980a). When firing in a regular manner "in vitro", the cells are firing at a rather high rate between 20 Hz and more than 100 Hz (Shin et al., 2007).

The Purkinje cell is a huge integrator cell. Due to its dense dendritic tree, morphologically accurate models of the cells were designed to understand passive components (Rapp et al., 1994; Shelton, 1985), and dendritic integration (De Schutter & Bower, 1994; Roth & Häusser, 2001). The Purkinje cell also exhibits a great variety of ionic channels in its soma and dendrites which made De Schutter and Bower, 1994 add up to 10 voltage-gated chan-

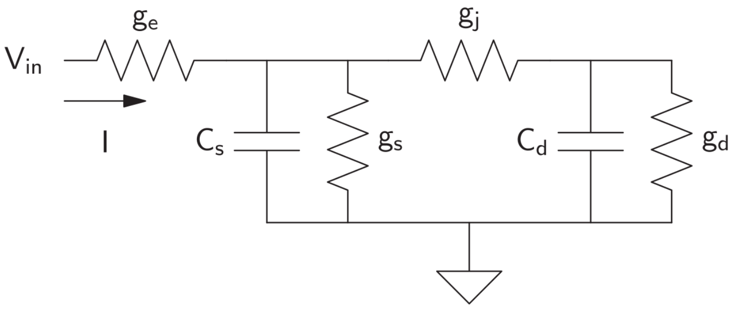

Figure 27:
Purkinje cell two-compartment passive model
Represents a two compartment passive cell with the patch electrode (g_e) in whole-cell mode. From Ostojic et al., 2015

nels in their model in an attempt to have the most exhaustive one. On the other hand Roth and Häusser, 2001, only added the I_h current as it significantly affects sub-threshold dynamics, on which they were focusing their work. As mentioned, the Purkinje cells can fire at a rather high frequency “in vitro”, potentially due to a “resurgent” sodium current (Raman & Bean, 2001). In order to test this hypothesis, Khaliq et al., 2003 incorporated eight ionic currents including this resurgent one, but in cylindrical mono-compartmental model to reproduce Purkinje cell firing behaviour.

Although complex models can reproduce single-cell responses with great accuracy, they present a number of limitations. Theoretical solutions are nearly impossible and understanding mechanisms is facing some kind of “black box”. Also, these models cannot be implemented in large networks. The opposite approach may reveal some advantages, starting with a simple model and adding block by block some complexity. At the passive level, the Purkinje can be represented as a passive two-compartment model (Llano et al., 1991) (Figure 27), with the first compartment representing the soma and proximal dendrites and the second the distal ones. The passive properties of a two-compartment Purkinje cell, when compared to a morphological detailed one can be quite similar (Roth & Häusser, 2001).

Investigating the Purkinje’s firing frequency profile, Ostojic et al., 2015, combined the two compartment model (Figure 27) with an EIF spiking mechanism. The Purkinje cell exhibits a rather unusual firing frequency response with an amplification (resonance) of the response in the 100 to 200 Hz range (Figure 28). The single compartment models failed to reproduce this response where the morphologically detailed one succeeded. But, more interestingly, a simple two-compartment EIF model with the right combination of high dendritic and small somatic noise was sufficient to qualitatively

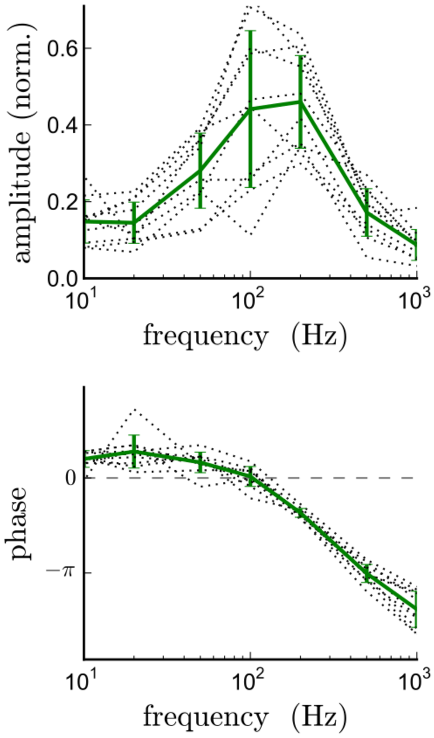

Figure 28:
Purkinje cell high-frequency firing resonance
Rat Purkinje cell spiking frequency response to oscillating current inputs. Dashed grey lines are individual cells. Green solid line and error bars are mean and standard deviation respectively. Amplitude is normalised on cell's firing rate. From Ostojic et al., 2015

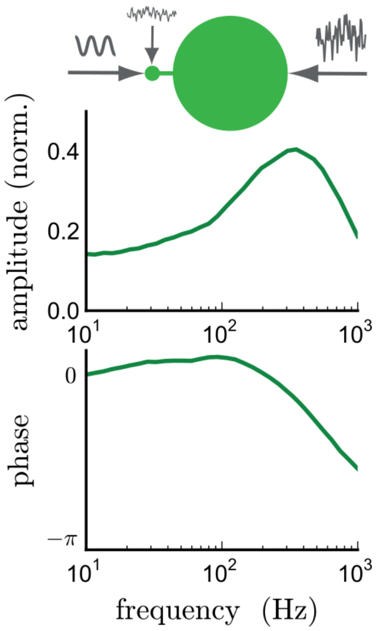

Figure 29:
Purkinje cell simulations reproduce firing resonance
Two compartment model cell response to oscillating current inputs with noise, represented by the drawing in the upper part of the figure. The mean response of multiple simulations is represented. Amplitude is normalised on the cell's firing rate. From Ostojic et al., 2015

reproduce the high-frequency resonance (Figure 29).

Part II

Results

4 Preliminary work

4.1 First protocols of resonance

Prior to this project some exploratory experiments were made on Purkinje cells' firing responses to short stimuli. Using the model of Ostojic et al., 2015 to reproduce the responses proved to be more challenging than expected. There was a need for a deeper characterisation of the Purkinje cells. Also, we changed from rat to mice compared to Ostojic et al., 2015, experiments; the first step was therefore to reproduce the same experiments and see if the two animal models had similar responses.

Using the same principle as the resonance experiments, we started probing the frequency responses of mouse Purkinje cells by putting the cell in current-clamp mode, where the cell already spikes at a rather steady pace without the injection of current. In this mode, a series of individual sine waves with an amplitutde of 10pA at 10 frequencies was injected. The frequencies were arranged in a random manner for each experiment. For each frequency sweep, individual spike times in one cycle were reported. The cycle was divided into 25 bins where the number of spikes was summed and divided by the time step of the bins, depending on each frequency. This gave a sine of spiking modulation that could be fitted and the amplitude and phase for each fit gave the frequency profiles in figures 30 and 31.

The first batch of experiments was performed on 12 cells without any pharmacological channel blockers (Figure 30). The results were similar to Ostojic et al., 2015. However two main problems appeared with these results:

- The great disparities between the individual responses.
- The prominent firing-rate resonance.

The peak of resonance is more or less centred around the firing rate making it impossible to disentangle whether the resonance arises from the firing rate or is an intrisic characteristic of the cell. For this reason, and with the idea of putting ourselves in the most deterministic situation we could, we chose to remove synaptic noise by adding NBQX (5µM) and Gabazine (10µM) in the bath, to block AMPA and $GABA_A$ receptors respectively. In order to have a more precise definition around the apparent resonance we concentrated the probed frequencies from 20 to 1000 Hz (9 frequencies). The results are shown in Figure 31.

We can see that when the definition is better, we can dissociate the two possible resonances. In Figure 31, a peak is associated with the firing rate but a second one around 200 to 300 Hz emerges. Nevertheless the firing rate frequency is still too prominent in the results and the second peak could also be a harmonic of the firing rate. It is also notable that the inter-

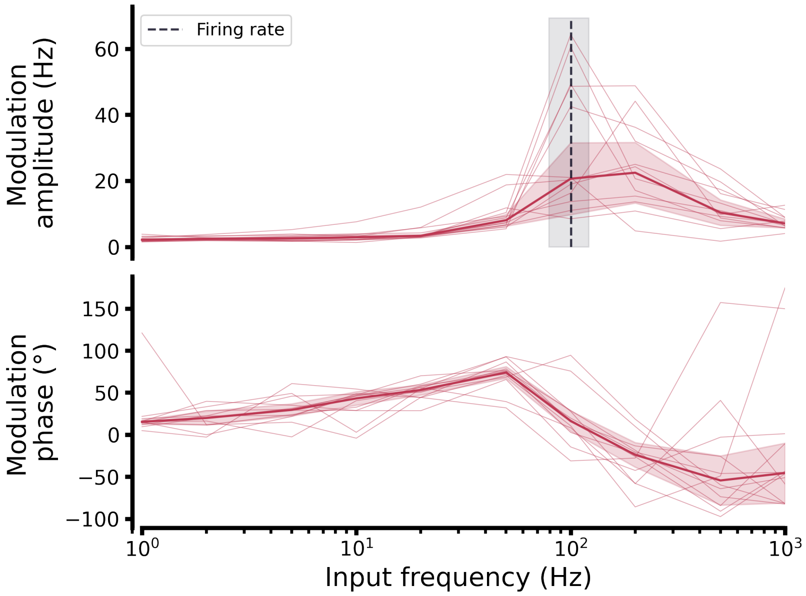

Figure 30:
Frequency profile with synaptic noise
The thin line represents individual cell responses. The solid line is the mean across the cells (n=12). The filled area around the median is the median absolute deviation (MAD). The dashed line represents the median firing rate (100 Hz) of all cells and the surrounding filled area the MAD (21 Hz). No pharmacology was used in these experiments.

cell variability was not obviously diminished by removing the synaptic noise. That led to the conclusion that the biggest contamination to the data would come from the firing rate resonance.

4.2 Firing rate clamp

One way of controlling the firing rate resonance would be to fix the firing rate of the cell during the experiments. Based on the work of Couto et al., 2015, we implemented an Arduino combined with a small circuit to compute the instantaneous firing rate and apply the appropriate amount of current inline to stabilise the cell at a given firing rate. The detail of this “firing rate clamp” will be given in the following article. This led to experiments similar to the one in figures 30 and 31. The overall results was still not satisfactory. The main problem was that not enough frequencies were probed during the experiments. Indeed, having the cell fire for more than a few minutes in a row is the maximum that could be expected from the experiments. For each

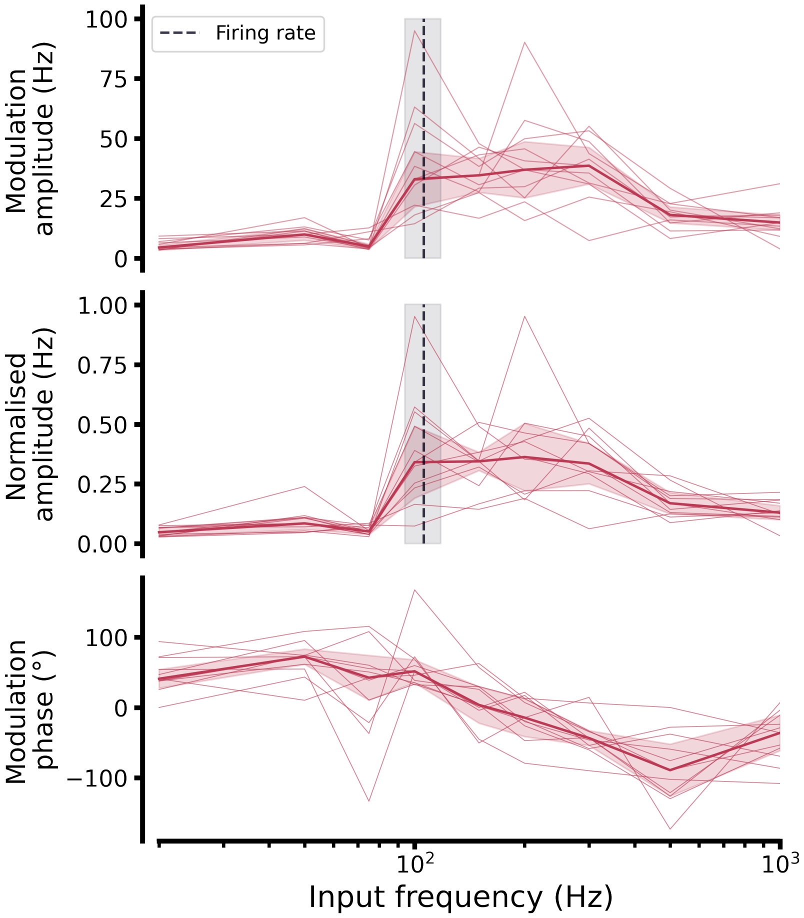

Figure 31:
Frequency profile without synaptic noise

The thin line represents individual cell responses. The solid line is the mean across the cells (n=11). The filled area around the median is the median absolute deviation (MAD). The dashed line represents the median firing rate (106 Hz) of all cells and the surrounding filled area the MAD (12 Hz). In the middle plot the data is normalised against each cells firing rate. We can see that the normalisation does not change the shape of the response. NBQX (5µM) and Gabazine (10µM) was used in these experiments to remove synaptic noise.

frequency there was a need for at least 5 seconds of firing in order to gather enough spikes for an comfortable analysis. We decided to try some other approaches.

4.3 PRC

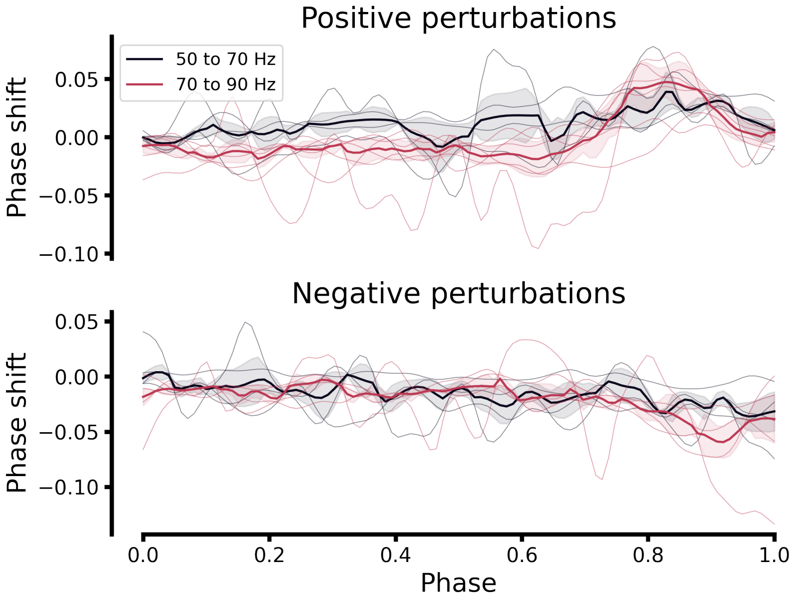

Figure 32:
Purkinje cell phase response curve
The thin line represents individual cell responses. The solid line is the median across the cells surrounded by the MAD (n=4). Solid lines surrounded by light area represent the median and the MAD of the data. A minimum of 300 steps was required for each positive or negative step so that the trace could be revealed.

We wanted to explore the frequency response of the Purkinje cell in the most deterministic manner we could. Inspired by the work of Couto et al., 2015, we decided to try to investigate the phase response (PRC) curve of the cells. The PRC consists of having a stable and frequency-locked system, here the cell firing at a given rate, and changing the system with small perturbations. The perturbations are distributed throughout the overall phase of the periodic system. The goal is to compute the phase shift produced by the perturbation depending on its time of arrival during the phase. The perturbations were distributed randomly between positive and negative steps to have an overall current of zero injected into the cell. The inter-perturbation intervals were not homogenous, to target the full range of phases. As we can see on Figure 32, the problem of obtaining a reproducible response across cells with a clear effect that could be explored by pharmacology and reproduced in models was not resolved by the PRC.

Precise measurement and mechanistic modelling of high-frequency firing resonance of cerebellar Purkinje cells

Alan Montarras, Guy Bouvier, Vincent Hakim, Jonas Ranft and Boris Barbour

Institut de Biologie de l'ENS (IBENS), Département de biologie, École normale supérieure, CNRS, INSERM, Université PSL, 75005 Paris, France.

November 23, 2022

Abstract

The most fundamental operation of a neurone is to transform synaptic input into output spikes. Active conductances are known to shape the responses of some neurones to inputs, typically at low and moderate input frequencies. In addition, a 'morphological' mechanism of firing-rate resonance resulting from a strong asymmetry of somatic and dendritic compartments has been reported in cerebellar Purkinje cells. In attempting to examine its mechanisms in detail, we encountered difficulties in performing sufficiently precise measurements of firing responses to test accurate single-cell models. Here, we describe on the one hand a general approach to constructing an accurate cellular model incorporating impedance and active conductances referred to the somatic compartment, where firing initiates, and on the other hand a measurement design enabling low-noise determination of the spectrum of firing modulation. We then compare the measured firing responses to the constructed model. Our measurements reveal a very strong high-frequency resonance and that interspike behaviour is controlled by a prolonged AHP. Our models are unable to account quantitatively for the strength of the firing response of the Purkinje, suggesting the existence of an unknown mechanism of high-frequency resonance.

1 Introduction

The biophysical mechanisms underlying synaptic integration and action potential generation are well understood in principle. However, constructing accurate and efficient firing models remains difficult. Spiking neurone models range from the single-compartment Leaky Integrate-and-Fire (LIF) model to detailed and explicit multi-compartment models incorporating complex voltage-dependent channel mechanisms. The simplest models fail to capture accurately the properties of synaptic integration and firing responses, while the huge numbers of parameters of the complex models can be extraordinarily difficult to determine and to interpret. In attempting to construct accurate and sufficiently simple models to generate insight into a remarkable high-frequency resonance in cerebellar Purkinje cells, we were confronted with an additional difficulty: testing a model precisely requires accurate characterisation of the firing response, which we were initially unable to perform. In this paper we describe the construction of a moderately simple and accurate firing model as well as the parallel design of a measurement technique able to characterise accurately the firing response of the neurone.

The transformation of synaptic input into action potentials can be characterised as a linear system by measuring the modulation of firing rate in response to sinusoidal currents, typically injected at the soma (although generalisation to dendritic inputs is obviously also of interest). The basic idea is illustrated in Fig. 1. The presence of certain voltage-dependent conductances can influence this response spectrum, notably the hyperpolarisation-activated channel, Ih, T-type calcium channels (Llinás and Yarom 1986; Puil et al. 1994). These conductances generally generate a resonance in the low- to medium-frequency portion of the response spectrum (Richardson et al. 2003).

A quite separate resonance mechanism has been described in modelling firing in a two-compartment model of the cerebellar Purkinje cell (de Solages et al. 2008), which led to the prediction of the existence of a firing resonance at much higher frequencies, around 200 Hz. We then verified the existence of the predicted resonance in measurements in Purkinje cells in slices (Ostojic et al. 2015). The main mechanism underlying the resonance was the interaction of any firing mechanism—implying the existence of a threshold—with a somatic impedance plateau in the 10–1000 Hz frequency range. However, our measurements were too noisy to permit comparison of single-cell models and measurements. This blocked us from exploring and corroborating the mechanism in greater detail.

Purkinje cells are continuously active in vivo and this is known to be an intrinsic property for Purkinje cells in slices; it remains an open question whether an excitatory synaptic barrage underlies the firing in vivo. In slices, if synaptic input is blocked, Purkinje cells fire with a high degree of

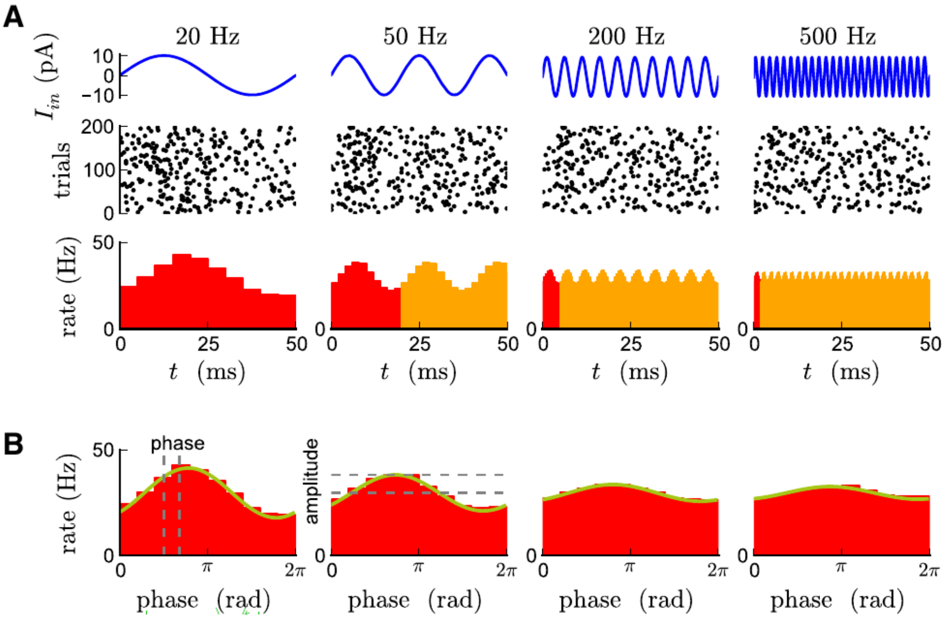

Figure 1: Linear characterisation of firing response. A. Diagram of injection of sinusoidal currents at different frequencies (top), detection of action potential times (middle) and construction of stimulus-triggered spike-time histograms (bottom). B. The data are averaged into a single cycle and the amplitude and phase of the best-fit sinusoid at the stimulus frequency is determined. Thus the transfer function from injected current to modulation of firing rate is determined. Reproduced from Ostojic et al. (2015)

regularity, and inhibitory inputs, likely somatic, appear to drive much of the instantaneous variation of firing (Häusser and Clark 1997).

Consider an experiment under noise-free conditions probing the firing response with small sinusoidal current injected at the soma. Stimuli falling near the frequency of the spontaneous firing or its harmonics will appear to to generate extremely strong responses, a phenomenon that is sometimes termed the ‘firing-rate resonance’. Because it is difficult to probe a large number of input frequencies and because the rate of spontaneous firing naturally drifts, it turns out to be remarkably difficult both to determine an accurate response spectrum and also to disentangle the firing-rate resonance from other mechanisms.

One possible solution to the problem of the firing-rate resonance is to introduce sufficient noise (either synaptic or injected) to disrupt the resonance. We followed this approach previously. This, however, introduces several new problems. The noise reduces the precision of the desired measurement, can attenuate the high-frequency (morphological) resonance and, more generally, it turns out that the spectrum of the noise shapes the response spectrum (unpublished simulations, but also apparent from the differential effects of dendritic and somatic noise in Ostojic et al. (2015)). In short, the addition of noise both distorts the response spectrum and obscures its measurement.

An alternative approach to characterising neuronal firing responses is the phase-response curve (PRC), in whose determination brief, small, randomly timed current pulses are injected and the change in timing of the next spike determined. A difficulty of the technique is that the time when the following spike would have occurred is not known precisely, introducing noise into the measurement. Depending upon the underlying assumptions of the spiking model, the noise can also intervene in the determination of the time of the reference spike (Phoka et al. 2010); this problem is particularly acute when resolving the portion of the PRC just before the spike, as this requires the use of small probe stimuli, but this is precisely the section of the PRC likely to give most information about high-frequency responses. In our hands, we were unable to obtain a precise characterisation using this technique.

Returning to the frequency domain, we considered the classical approach of injecting broad-spectrum noise. This has the advantage of disrupting the firing-rate resonance (if sufficiently strong), but still posed problems, namely that all noise present in the system is also subsumed into the measured responses and all of the infinitesimal frequencies have vanishingly small amplitudes, necessitating additional averaging mechanisms.

We finally arrived at an experimental design in which we simultaneously injected 50 defined frequencies of sinusoid, i.e. with a comb-like spectrum. The multiple advantages in terms of precision and interpretation of this design will be justified below. This technique finally enabled us to make quantitative comparisons with firing models, which therefore also needed to be precise.

In order to construct firing model to test our understanding of the firing response, we used models with a small number of compartments. The soma (or more precisely the closely connected axon initial segment) are the site of axon potential initiation, so any effective model must be able to predict its response to inputs anywhere in the cell. A two-compartment model of the Purkinje cell (Llano et al. 1991) is already quite effective for reconstituting the impedance of the the cell as viewed from the soma; we used a three-compartment model to ensure an accurate representation.

Because the hyperpolarisation-activated conductance Ih is prominent in Purkinje cells, we augmented the passive model with a linearised Ih model. We introduced a simplified but accurate representation of the active currents in the somatic compartment: an exponential integrate-and-fire (EIF) mechanism (Fourcaud-Trocmé et al. 2003) in lieu of the sodium current and an exponential after-hyperpolarisation (AHP) current. The precise compartmental model allowed us to define accurate reset conditions after the action potential.

Analysis of the reconstituted action potential cycle in our model shows that the action potential depolarises the dendrites which then in turn tends to depolarise the soma; however the soma is maintained at a more negative potential throughout most of the cycle by a slowly decaying potassium current.

A model incorporating these mechanisms was able to reproduce all of the features of our precise measurements of the Purkinje cell firing-response spectrum.

2 Materials and Methods

2.1 Slice preparation, recording and analysis

Adult female C57BL6/J mice were sedated, anæsthetised with Ketamine/Xylazine (100 mg/kg, 10 mg/kg) and decapitated under profound anæthesia. The cerebellum was dissected out and blocked for slicing parasagittal slices. Slices of 300 μm were cut on a Campden Instruments 7000 smz vibratome. Slicing was performed at 34°C (Huang and Uusisaari 2013) in a saline containing 50 μM D-APV. The same saline as the extracellular solution during recording, with SR 10 μM and NBQX 5 μM.

Two pipette solutions were used. Solution 1 (in mM): 128 K-gluconate, 10 HEPES, 2.2 K2-phosphate, 4 NaCl, 0.5 L-(−)-Malic acid, 0.0008 Oxaloacetic acid, 0.18 α-Ketoglutaric acid, 0.2 Pyridoxal 5'-phosphate hydrate, 5 L-Alanine, 0.15 Pyruvic acid, 15 L-Glutamine, 4 L-Asparagine, 0.5 K3-Citrate, 0.05 CaCl2, 0.1 K3.8EGTA, 1 L-Glutathione, 5 K2-Phosphocreatine, 0.4 Na-GTP, 2.1 Mg-ATP, 1.4 Na-ATP, 0.5 NAD+. The solution was titrated with 10 NaOH and then KOH to pH 7.3. Finally, water was added to dilute the solution to 300 mOsm. The final solution contained 15.75 Na, 144.2 K, 4.1 Cl, 0.0001 free Ca and 0.4 Mg. Solution 2 (in mM): 130 K-Gluconate; 0.6 EGTA; 2 MgCl2; 0.2 CaCl2; 10 HEPES; 2 Mg-ATP; 0.3 Na3-GTP, pH 7.3 with KOH (295-300 mOsm). The extracellular solution contained (in mM): 125 NaCl, 26 NaHCO3, 3.5 KCl, 1.25 NaH2PO4, 1.5 CaCl2, 1.8 MgCl2, 25 D-glucose.

Patch electrodes were pulled from borosilicate glass on a home-made puller and typically had resistance in the bath of 2.5–4 MΩ. To perform the whole-cell patch-clamp recordings, we used a Molecular Devices Multiclamp 700B, driven by a National Instruments DAQ interface controlled by WinWCP software (Dempster 2022). The recording temperature was maintained at 32°C by a feedback controller. The slice was visualised using red light and an Altair H164M Hypercam camera. Voltages are reported without correction for the junction potential; real voltages are expected to be about 10 mV more negative. Complete stimulus protocols were designed and applied that included different blocks: measurement of the current transient to voltage steps, series of voltage jumps to characterise Ih, etc. The order of the blocks was randomised and within the blocks the order of the stimuli was also randomised if appropriate. Thus, within a block, the steps for characterising Ih would be applied in a different order for each cell.

A controller was designed to control Purkinje cell firing rate during recordings. The algorithm will be described below. It was implemented on an Arduino Due interfaced with a small custom electronic circuit to adapt its inputs and outputs to the voltage ranges used by the amplifier and ADC/DAC converter.

Recordings were analysed using home-written Python scripts.

For measurements analysing the secondary amplifier output, which is intended as a copy of the command (voltage in voltage clamp, current in current clamp), we reconstituted the exact times of its samples interleaved between those of the primary channel. Thus, in a voltage-clamp experiment in which the two channels were sampled at 50 KHz, the analog-to-digital conversion multiplexes between the two channels, so the current would be sampled at $t = 0$, $20\,\mu$s, $20\,\mu$s..., while the voltage would be sampled at $t = 10$, $30\,\mu$s, $50\,\mu$s...

For some of the experiments, a minor rounding bug in the acquisition software caused the analog-to-digital conversion to be sampled with an interval of $19.99\,\mu$s while the digital-to-analog conversion was sampled at the intended $20.00\,\mu$s interval. Where the difference was significant, we interpolated one or both of the traces to a common time base. For the analysis of the current transients in voltage clamp, this error in fact allowed us to reconstitute a transient oversampled at 0.5–1 MHz from 100 repetitions of the stimulus during which many relative timings of the two channels were scanned.

Simulations were written in Python and occasionally made use of the Brian simulation software (Stimberg et al. 2019).

2.2 Amplifier response

2.2.1 Voltage clamp

In order to maximise the precision of our fitting of the cell model we explored the characteristics of the patch-clamp amplifier. In particular, the impedance of the cell as viewed from the soma is of critical importance, yet its time constant in the Purkinje cell can be as short as a few tens of microseconds, so we felt that some care was required to account for the early portions of the voltage-clamp response. This is illustrated in Fig. 2, where it can be seen that the electrode capacitance generates a large current that can overlap with and deform the upstroke of the cellular response that is crucial to determining the electrode and somatic properties.

Fig. 3 shows the circuit and signal-processing elements used to model the amplifier in voltage-clamp mode. The electrode or a test circuit would

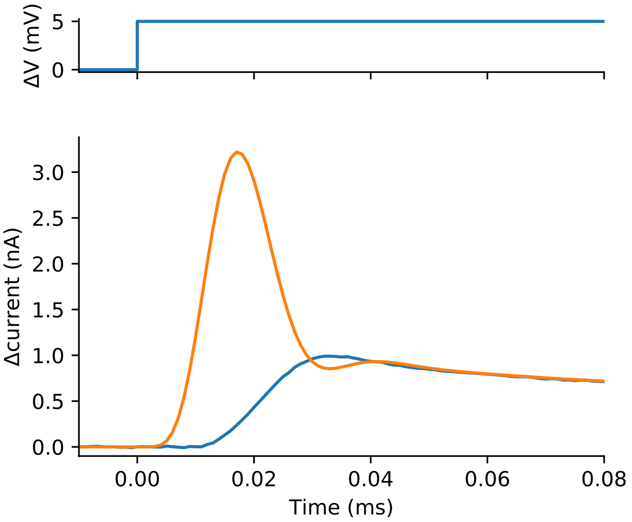

Figure 2: Possible interference of electrode capacitance with the neuronal response to a voltage step. A. Voltage-step. B. Purkinje cell current response in a carefully cancelled recording (blue) and the predicted response with no cancellation of the pipette capacitance (orange).

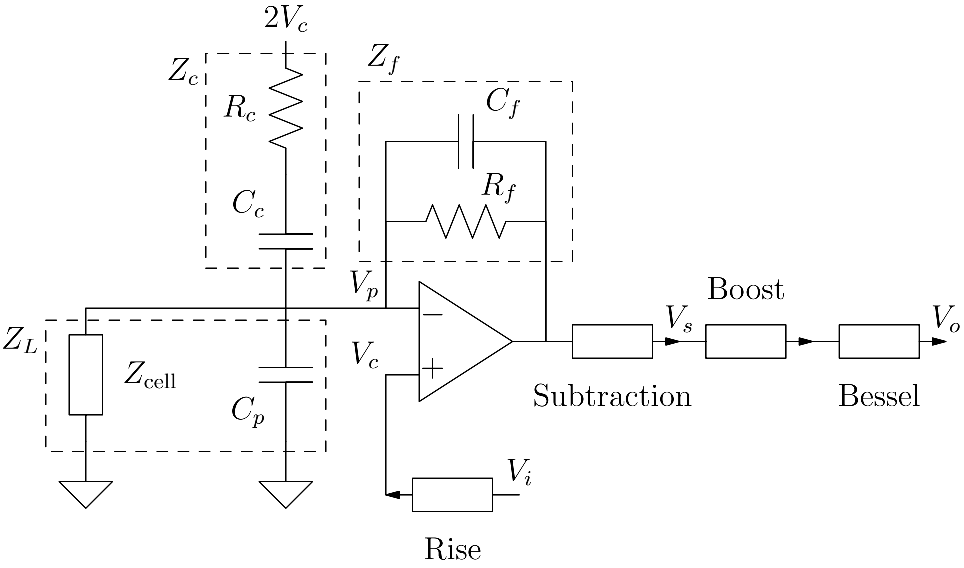

Figure 3: Circuit used to model amplifier characteristics in voltage clamp. See description in Methods.

be connected as Z_{cell}. C_p is the pipette/parasitic capacitance. The input voltage V_i is lightly filtered by the "Rise" filter to generate V_c. The central operational amplifier (opamp) is in the classical current-follower configuration, with parallel high resistance R_f and low capacitance C_f as feedback elements. We did not employ series-resistance compensation, to simplify analysis and modelling, but the electrode capacitance cancellation circuitry was used and is modelled by charge injection across the components of Z_c, driven by a multiple of the command voltage V_c. The output from the opamp undergoes quite complex processing, with first subtraction of the command voltage ("Subtraction") and then high-frequency boost ("Boost") to reverse partially the low-pass filtering caused by the $R_f||C_f$ feedback combination of the current follower. Finally, an optional 4-pole Bessel filter is applied before the recorded signal is output.

Various measurements of circuit behaviour with different test configurations were performed, a model was constructed and the unknown parameters were adjusted manually to reproduce approximately the responses observed. The modelling was done in the frequency domain using complex impedances. The manipulations of Fourier transforms involving capacitances often ran into numerical problems at zero frequency (their impedance is infinite). This was mitigated by replacing zero with a frequency much below the range of interest. In some cases, the average signal required a separate calculation (notably when calculating the steady-state current in the presence of non-zero reversal potentials). When deconvolutions were performed, we often filtered ringing using a Gaussian filter with a $10\,\mu$s standard deviation.

The opamp of the current follower was characterised in detail and was parameterised by a open-loop gain G_A and gain-bandwidth product P_A. The transfer function is

$$H_A(s, G, P) = \frac{G_A}{1 + sG_A/(2\pi P_A)}, \tag{1}$$

where $G = 10^6$ and $P = 2 \times 10^8\,\mathrm{Hz}$. The latter value is particularly large and may indicate an implementation involving a compound opamp: two opamps in series with the feedback looping from the output of the second to the input of the first. (To convert these Laplace representations to the frequency domain it suffices to replace s by $i\omega$.) We set $R_f = 500\,\mathrm{M\Omega}$ according the manufacturer's specification and from our measurements we estimated $c_f = 0.3\,\mathrm{pF}$.

The transfer function for non-critical amplifiers just included their bandwidth (as a time constant), which is equivalent to a low-pass filter,

$$H_a(s, \tau) = \frac{1}{1 + s\tau}. \tag{2}$$

A few simple combinations (outlined by the dashed boxes in Fig. 3) will simplify the equations,

$$Z_L = \frac{1}{1/Z_{\text{cell}} + sC_p}, \quad Z_c = R_c + \frac{1}{sC_c}, \quad Z_f = \frac{1}{1/R_f + sC_f}. \tag{3}$$

The Rise filter was approximated by cascaded amplifiers to generate a sigmoid response,

$$H_r(s) = H_a(s, \tau_r)^3, \tag{4}$$

where $\tau_r = 0.8\,\mu\text{s}$.

It is simplest to group the current follower and subsequent subtraction of V_c together,

$$H_{cs} = \frac{V_s}{V_c} = H_A \left(\frac{Z_f Z_c + Z_L Z_c - Z_L Z_f}{(H_A + 1) Z_c Z_L + Z_f Z_L + Z_f Z_c} - \frac{1}{G} \right), \tag{5}$$

where all H, V, Z and (below) I are functions of s, which has been omitted for readability. We shall retain this convention below. The high-frequency boost stage that will be described next amplifies high-frequencies so strongly that V_c needed to be subtracted with a frequency response matching the signal pathway, to prevent unpleasant artefacts. It is unclear how and whether this is implemented in the real amplifier.

The high-frequency boost element was assumed to operate as described in Sakmann and Neher (2009) with transfer function,

$$H_b = \frac{s\tau_a + 1}{s^2 \tau_b \tau_a + s(\tau_b + \tau_0) + 1}, \tag{6}$$

where $\tau_s = 50\,\text{ns}$ is the time constant of the boost opamp, $\tau_b = R_f C_f + 1/(2\pi P_A)$ and $\tau_0 = \sqrt{\tau_a \tau_b}$.

The transfer function of the 4-pole Bessel output filter was

$$H_o = \frac{105}{(sf_b/f_c)^4 + 10(sf_b/f_c)^3 + 45(sf_b/f_c)^2 + 105sf_b/f_c + 105}, \tag{7}$$

where $f_b = 0.3364$ and f_c is the corner frequency, which was typically 10 kHz or 30 kHz for the present recordings.

In summary, the transfer function from external command voltage to output is thus,

$$H_{VC} = \frac{V_o}{V_i} = H_r H_{cs} H_b H_o. \tag{8}$$

Below, we use this compound transfer function to generate the predicted current response of the cell to a voltage step, by taking the Fourier transform of the step, multiplying by H_{VC} and taking the inverse transform.

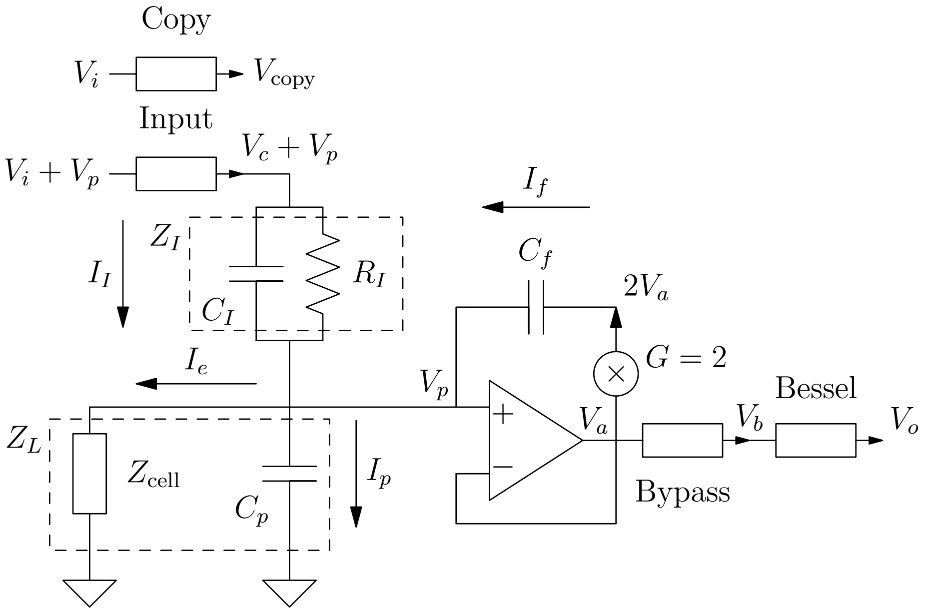

Figure 4: Circuit used to model amplifier characteristics in current-clamp. See description in Methods.

2.2.2 Current clamp

The circuit used to model the current-clamp mode of the amplifier is shown in Fig. 4. It should be noted that it is different to the voltage-clamp circuitry. At its centre there is an opamp in the voltage-follower configuration, with a feedback capacitor providing capacitance neutralisation; we did not employ bridge-balance so do not model it. The electrode or testing components would be connected in the position of Z_{cell}. Current injection is controlled by a voltage signal V_i (2 nA/V) via injection across a high resistance ($R_I = 500\,\mathrm{M\Omega}$). In order to prevent variations of V_p from affecting the injected current, V_p is added to the command voltage V_c, which is a filtered ("Input") version of V_i. In practice, V_p is not directly available and V_a is likely employed, but the practical difference under our conditions is minor. We shall see below that the injection resistor R_I has associated with it a parallel parasitic capacitance C_I through which additional current is injected at high stimulation frequencies. It turns out that the secondary amplifier output reporting the current command is further filtered, represented by the "Copy" transfer function. There is an optional 4-pole Bessel filter at the output, but even in the bypass configuration with not Bessel filter there seemed to be quite significant filtering of the signal.

As for the voltage-clamp circuit, we establish a few simplifying combinations,

$$Z_L = \frac{1}{1/Z_{\text{cell}} + sC_p}, \quad Z_I = \frac{1}{1/R_I + sC_I}. \tag{9}$$

Some of the symbols are recycled from the voltage-clamp circuit, even if in come cases they represent different components (e.g. C_f). We make use of (2) with different parameters.

The currents can be described in the frequency domain. In what follows, all I, V, H and Z are functions of s.

$$I_I = \frac{V_c}{Z_I} \tag{10}$$

$$I_p = sV_pC_p \tag{11}$$

$$I_f = \frac{sC_fV_p(2G - 1 - s\tau_a)}{1 + s\tau_a}, \tag{12}$$

where τ_a is the time constant of the voltage follower. By the current balance at the V_p node,

$$I_e = I_I + I_f - I_p. \tag{13}$$

The Bessel filter H_o is the same as described in the voltage-clamp section above. It remains to determine the nature of the "Bypass", "Input" and "Copy" filters. To estimate the circuit parameters, we connected an opamp in the voltage-follower configuration in the place of Z_{cell}. This enabled us to access a reliable measure of V_p. In this configuration, the only load is an increased C_p, to which the opamp input capacitance contributes. As shown in Fig. 5, a step current caused a constantly increasing voltage, as expected for a capacitive load. The slope of the voltage enabled estimation of the load C_p. When the voltage slope was extrapolated back to step onset, the intersect was non-zero. We interpret this as demonstrating the existence of a parasitic capacitance C_I (see Fig. 4) in parallel with the injection resistance R_I. Such capacitances are difficult to eliminate and more complex circuitry would be required to mitigate it. We estimate $C_I = 0.27\,\text{pF}$. This seems quite small when C_p may be 5–10 pF and the soma 20 pF. However, because the injection resistance has a high value, the voltages applied to drive current through it are also elevated, with the consequence that non-negligible excess charge can be injected. The effects of this excess will be illustrated in the Results for the stimuli employed.

We verified that capacitance neutralisation worked as expected. Neutralisation of $C_f = 8\,\text{pF}$ out of $C_p = 10\,\text{pF}$ increased ∼5-fold the slope and the intercept, as expected. For large voltages, some response nonlinearities emerged, but these are unlikely to be significant in the ranges studied below.

The voltage changes at step onset were not instantaneous. It was from their time courses that the various time constants in the system were estimated. The fits of the model from which the estimates were drawn are shown superimposed upon the measurements in Fig. 5.

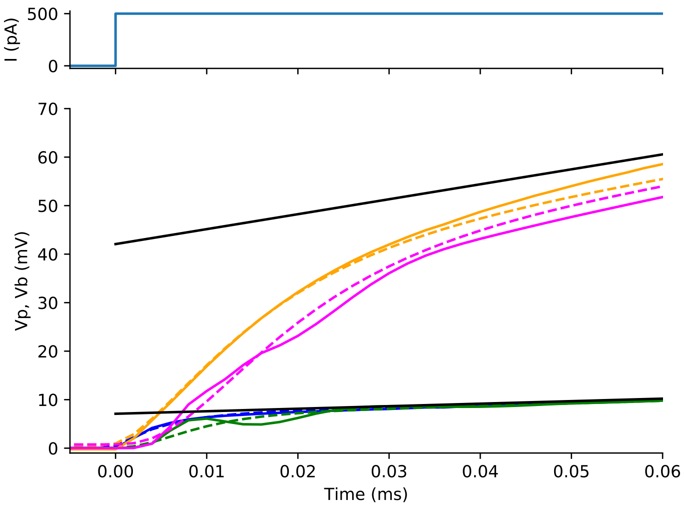

Figure 5: Measurement of current-clamp performance. Top: current step. Bottom: as described in the text, a voltage-follower opamp allows direct measurement of V_p (blue, orange; see Fig. 4 for explanation of the symbols) in addition to the amplifier output V_b (green, magenta). Measurements were performed without (blue, green) and with (orange, magenta) neutralisation of 8 pF. Black lines show extrapolated fits to the linear portions of the V_p traces. The dashed lines show a global fit, by which the parameters of the current-clamp circuitry were estimated.

The "Input" filter is given by $H_a(s, \tau_i)$ where $\tau_i = 5.2\,\mu\text{s}$. The "Copy" filter is given by $H_a(s, \tau_i) H_a(s, \tau_{\text{copy}})^2$, where $\tau_{\text{copy}} = 1.3\,\mu\text{s}$. The voltage follower was estimated to have $\tau_a = 1.2\,\mu\text{s}$. The time constant τ_b of the "Bypass" filter was $3.3\,\mu\text{s}$.

Although the directly measured V_p voltages are smoothly rising, the V_o voltages reported by the amplifier display quite significant ringing. The mechanism underlying this behaviour is unknown.

The transfer function from V_p to V_o is thus

$$H_{po} = H_a(\tau_i) H_a(\tau_b) H_o. \tag{14}$$

2.3 Model Purkinje cell

We constructed a 3-compartment model of the Purkinje cell (Fig. 6) that could be connected via an electrode with conductance G_e as Z_{cell} in the voltage- and current-clamp models described above. The compartments were in series: soma (s) , proximal dendrites (d) and terminal dendrites

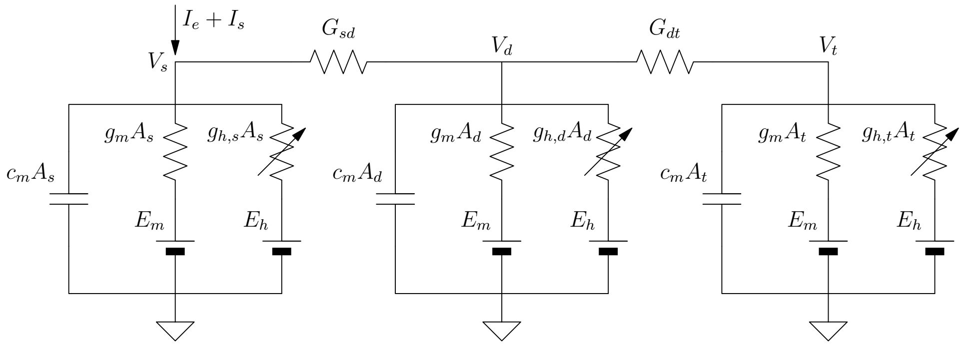

Figure 6: 3-compartment model of the Purkinje cell, with Ih in each compartment. The two dendritic compartments are connected in series.

(t). The simplifying assumption was made that the membrane had uniform specific capacitance $c_m = 10^{-2}\,\mathrm{F\,m^{-2}}$ and conductance g_m, which varied between cells. The capacitances and conductances of each compartment were therefore determined by their areas. Each compartment contained an h conductance; this will be described in the next section.

To calculate the impedance of the model we successively calculate the admittance Y of each compartment ignoring the effect of those nearer the amplifier.

$$Y_t(s) = A_t(g_m + g_{h,t}(s) + sc_m) \tag{15}$$

$$Y_d(s) = A_d(g_m + g_{h,d}(s) + sc_m) + \frac{Y_t(s)G_{dt}}{Y_t(s) + G_{dt}} \tag{16}$$

$$Y_s(s) = A_s(g_m + g_{h,s}(s) + sc_m) + \frac{Y_d(s)G_{sd}}{Y_d(s) + G_{sd}} \tag{17}$$

The impedance of the cell is thus $Z_{cell}(s) = 1/Y_s(s)$ and this is connected to the amplifier in series with the electrode conductance G_e.

We fitted current responses to voltage steps over a 30 ms time window, before significant activation of Ih, so we used the model above setting the $g_{h,x}$ to zero. In this situation the h conductance activated at the holding potential was considered constant and was included in the membrane conductance. In the cases when Ih was also fitted, the apparent membrane conductance was partitioned between the h conductance and the leak conductance.

The above impedance is not correct for the steady-state, where the current at a given potential depends upon the reversal potentials of the membrane and h conductances. The steady currents/voltages were therefore calculated separately according to the method described in the next section.

2.4 The h conductance

We used the classic one-variable model of Ih.

$$\frac{\mathrm{d}h}{\mathrm{d}t} = \alpha(1-h) - \beta(h) \tag{18}$$

$$\alpha = ae^{-b(V-V_{0.5})} \tag{19}$$

$$\beta = ae^{c(V-V_{0.5})} \tag{20}$$

which give

$$h_\infty = \frac{\alpha}{\alpha+\beta} \tag{21}$$

$$\tau_h = \frac{1}{\alpha+\beta} \tag{22}$$

We allowed the density of Ih to vary between compartments.

Calculating steady-state voltages within the 3-compartment model is complicated by the presence of Ih, whose activation depends upon the compartmental voltages. We solved for the compartmental voltages (V_x) using a numerical solver for simultaneous nonlinear equations constructed from the current balance in each compartment. The h conductances were factored into a maximum conductance and the h gating variable,

$$g_{h,x} = g_{h,x}^{\max} h_{\infty,x}, \quad x = s, d, t \tag{23}$$

and then the following expressions were set to zero and their roots found using `scipy.optimize.fsolve`.

$$G_{dt}(V_d - V_t) - A_t g_{h,t}^{\max} h_{\infty,t}(V_t - E_h) - A_t g_m(V_t - E_r) \tag{24}$$

$$G_{sd}(V_s - V_d) - G_{dt}(V_d - V_t) - A_d g_{h,d}^{\max} h_{\infty,d}(V_d - E_h) - A_d g_m(V_d - E_r) \tag{25}$$

$$G_e(V_p - V_s) - G_{sd}(V_s - V_d) - A_s g_{h,s}^{\max} h_{\infty,s}(V_s - E_h) - A_s g_m(V_s - E_r) \tag{26}$$

In experiments for determining the parameters of the h conductance we generated model current traces by numerical integration of the following compartmental differential equations

$$\frac{\mathrm{d}V_s}{\mathrm{d}t} = -\frac{A_s g_{h,s}^{\max} h_s(V,t)(V_s - E_h) + G_e(V_s - V_p) + G_{sd}(V_s - V_d) + g_m A_s(V_s - E_r)}{c_m A_s} \tag{27}$$

$$\frac{\mathrm{d}V_d}{\mathrm{d}t} = -\frac{A_d g_{h,d}^{\max} h_d(V,t)(V_d - E_h) + G_{sd}(V_d - V_s) + G_{dt}(V_d - V_t) + g_m A_d(V_d - E_r)}{c_m A_d} \tag{28}$$

$$\frac{\mathrm{d}V_t}{\mathrm{d}t} = -\frac{A_t g_{h,t}^{\max} h_t(V,t)(V_t - E_h) + G_{dt}(V_t - V_d) + g_m A_t(V_t - E_r)}{c_m A_t} \tag{29}$$

$$\frac{\mathrm{d}h_x(V,t)}{\mathrm{d}t} = \alpha(1-h_x) - \beta h_x, \quad x = s, d, t \tag{30}$$

The h-conductance was linearised about a compartmental voltage V_x^* as follows

$$\delta I_{h,x}(s) = g_{h,x}^{\max}\left[h_\infty(V_x^*) - \frac{h'_\infty(V_x^*)(E_h - V_x^*)}{1 + \tau_h(V_x^*)s}\right]\delta V_x(s). \tag{31}$$

2.5 Deconvolution of compartmental voltages and active currents

With knowledge of the output voltage and the amplifier current-clamp transfer functions, it is a relatively straightforward operation in the frequency domain to deconvolve the voltage where the electrode is connected to the amplifier headstage

$$V_p = \frac{V_o}{H_{po}} = \frac{V_o}{H_a(\tau_i)H_a(\tau_b)H_o}. \tag{32}$$

Similarly, knowledge of the current command V_i transfer function for the current pathway can be combined with the information about V_p to calculate the current injected across the electrode I_e, according to (13) and preceding equations. Knowledge of the electrode conductance G_e enables calculation of the somatic voltage V_s by Ohm's law.

We then determined the compartmental voltages in the presence of Ih. This was done for average voltages, average currents and average Ih activation by numerical solution of simultaneous nonlinear equations. This was described in Section 2.4. With these average voltages, it was possible to calculate the full impedance of the cell model using the equations beginning at (15).

The impedance of the cell determines the current expected to flow through the passive model including Ih. We can thus extract the active current at the soma I_s (see Fig. 6),

$$I_s(s) = \frac{V_s(s)}{Z_{\text{cell}}(s)} - I_e(s) \tag{33}$$

(As mentioned above, the steady values required special treatment because of the non-zero reversal potentials.) Using the compartmental impedance equations, it was then possible to determine the dynamic voltage in each of the compartments.

2.6 Feedback control of firing rate

As outlined in the introduction, the interpretation of response spectra is greatly complicated if the firing rate of the Purkinje cell is poorly defined and varies. In order to control this variable, much as was done by Couto et al. (2015), we designed a feedback controller to maintain firing near a target frequency. This was constructed using an Arduino Due open-source micro-controller interfaced to the amplifier output and command input. In outline, the algorithm was as follows. Spikes were detected and weighted by a bi-exponential kernel to generate a smooth rate estimate,

$$\hat{r} = \sum_i e^{-(t-t_i)/\tau_2} - e^{-(t-t_i)/\tau_1}, \quad t_i < t, \tag{34}$$

where $\tau_1 = 0.1\,\mathrm{s}$ and $\tau_2 = 1\,\mathrm{s}$. In practice, the two exponential kernels were incremented each time a spike was detected and decremented on each cycle of the controller. The bi-exponential function enabled new spikes to enter the kernel smoothly instead of causing a discontinuity in the rate estimator. The estimated firing rate $\hat{r}$ was compared with the target frequency r_0. The difference drove a proportional+integrating (PI) controller. The feedback command was,

$$F(t) = -k_P(\hat{r} - r_0) - k_I \int_0^t (\hat{r} - r_0)\mathrm{d}\tau, \tag{35}$$

where, k_P and k_I weight the proportional and integrating terms of the controller. The importance of the integrating term is that any error will eventually be eliminated. The feedback command was added to the experimental stimulus (such as current steps or the mix of sinusoids). A small home-built electronic circuit ensured matching of the voltage gains and bipolar ranges of the amplifier/interface to the monopolar range of the Arduino. The operation of the circuit will be illustrated below.

3 Results

3.1 Amplifier response

We sought to characterise the transfer functions of the patch-clamp amplifier used in our recordings. This was to ensure the accuracy of subsequent fitting of models of the Purkinje cell. We examined both voltage-clamp and current-clamp recording modes, which employ quite different circuits. We characterised both the command (input) pathway and the recording (output) pathways. For the output pathways both primary (independent variable) and secondary (command copy) channels were characterised, the latter to enable confirmation and in some cases reconstitution of the exact command. We have not obtained detailed information from the amplifier manufacturer, so several circuit elements were based upon classical amplifier circuits (Sakmann and Neher 2009).

The characterisation of the amplifier and the construction of the model are detailed in the Methods. A few key points are summarised here. Some effort (perhaps excessive effort) was expended to try to describe accurately high-frequency behaviour of the amplifier. We discovered that the secondary channels used to confirm the command voltage (in voltage-clamp) and current (in current-clamp) included filters (even in ‘bypass’ mode) that were not specified in the amplifier manual. Fitting the voltage-clamp response precisely proved to be challenging, no doubt reflecting significant complexity of the underlying circuitry.

In voltage clamp, the fits were not entirely satisfactory. Our model/optimisation seemed unable to detect correctly cancelled pipette capacitance, because the fits generally reported much lower values of C_p and the cancellation capacitance C_c than would be realistic. We interpret this as demonstrating that the cancellation circuitry works well and assumed that the often small difference between the two was reflecting the incorrectly cancelled electrode capacitance (the difference could be positive or negative).

A simpler and more significant issue became apparent while characterising the current-clamp circuitry. Current is typically injected into the electrode via a large resistance (500 MΩ). However, resistances invariably comprise a small parasitic parallel capacitance. Our characterisation showed that its effect could not be entirely neglected. Although a value of $\sim$0.3 pF seems small, quite large voltages are applied across the injection resistance and thus the excess current cannot always be neglected. We calculated that a 1 kHz sinusoidal current would be 30 % greater than intended, while a very significant if brief overshoot would be expected for step stimuli. This is illustrated in Fig. 4. For the step overshoot, the excess charge is 13 % for a 1 ms pulse; this ratio would increase for shorter pulses and decrease for longer ones. The overshoot is also likely to wreak havoc with any process sensitive to the derivative of the current. These measurements and predictions apply for the 500 MΩ injection resistance of our amplifier; preliminary measurements with the 5 GΩ injection resistance indicated a worse situation, with the current almost tripling at 1 kHz.

3.2 Passive model

Because action potential initiation occurs in the axon initial segment, whose voltage closely follows that of the soma until initiation occurs, a central objective was to construct an accurate model of the impedance of the Purkinje cell viewed from the soma. The work of Llano et al. (1991) showed that a two-compartment model, with a small soma and a large dendritic compartment, could provide a very effective description of the passive properties of the cell when voltage-clamped at the soma. Because adult Purkinje cells have a more complex morphology than the immature Purkinje cells studied by Llano et al, the two-compartment model deviated visibly from the current responses to voltage steps. In order maximise our description of the impedance of the Purkinje cell we therefore settled on a three-compartment model, in which the dendrites are divided into series proximal and distal

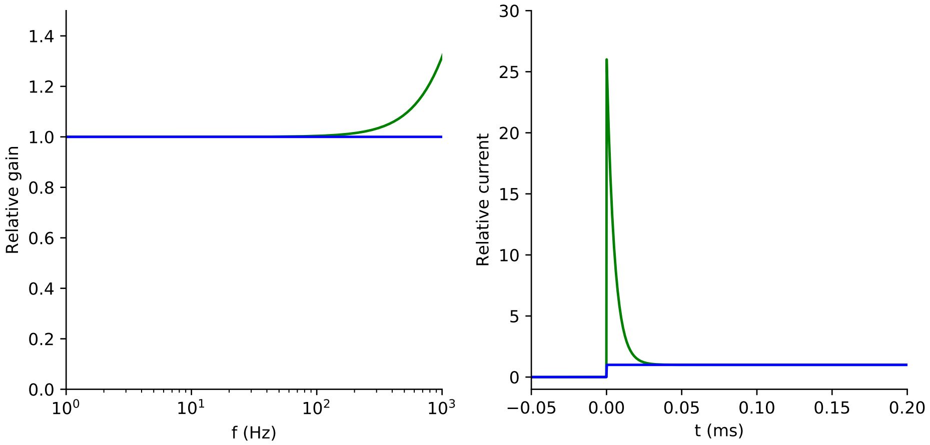

Figure 7: Distortion of current injection in the amplifier. A. Predicted gain of injected sinusoids relative to the low-frequency plateau. B. Predicted overshoot for a step stimulus. In both panels, blue shows the ideal response and green shows that occurring with the parasitic capacitance.

compartments. The cellular model used is shown in Fig. 6. A number of simplifying assumptions were made regarding the parameter values. In particular, we assumed that compartmental capacitance and membrane conductance were proportional to area and the reversal potential of the membrane conductance was common to all compartments. Each compartment also potentially contained Ih (see next section), with a common reversal potential and kinetic parameters. The electrode is attached to the soma and carries a current I_e. Active currents—the sodium and potassium currents underlying the action potential—are considered to be exclusively somatic (the axon initial segment is assumed to be effectively absorbed into the soma); the remaining compartments are passive, except for Ih. The sum of these active currents is I_s.

Using the amplifier model described in the Appendix attached to the neurone model of Fig. 6 without the h conductances through an electrode with conductance G_e, we fitted the current transient following a small voltage step. We used the transfer function of (8), multiplying it with the Fourier transform of the voltage step and then taking the inverse transform to obtain the current response. The difference between the predicted and measure response was minimised to find the best-fit parameters of the cell (A_s, A_d, A_t, G_{sd}, G_{dt}, R) and recording (G_e, C_p, C_f). The cost function in the minimisation was strongly weighted to ensure a close fit of the onset of the transient. The weighting function was $1 + 100e^{-|t-15\,\mu\text{s}|/500\,\mu\text{s}}$, where $t = 0$ is the time of the voltage step. The fit was truncated at 30 ms before

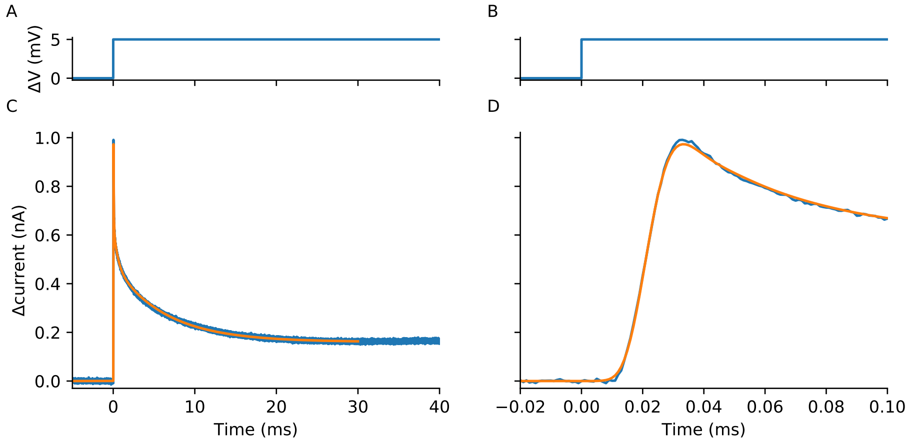

Figure 8: Fitting of current responses to voltage steps. A and B. Voltage steps. C and D. Average ($n = 100$) current responses (blue) at different time scales with the fit (orange) for a specimen Purkinje cell. Dashed lines show a global fit from which the parameters for Ih and the membrane leak conductance were derived.

before most of the activation of Ih occurred. The fit can be seen on two time scales in Fig. 8. Because Ih was not included explicitly, the membrane resistance determined at this stage contained a contribution from the h conductance activated at the holding potential. A sign that the amplifier model was not exact was that constraining the pipette/parasitic capacitance (C_p) and the neutralisation capacitance (C_f) to realistic values slightly degraded the fit at the onset of the response; the unconstrained version is presented here (the differences between $C-p$ and C_c remained small, however). The specific membrane capacitance was assumed to be $10^{-2}\,\mathrm{F\,m^{-2}}$. The group data for all parameter values will be presented below.

3.3 Ih description

Purkinje cells display a prominent h conductance. In a subset of neurones we performed a series of voltage jumps covering the activation range of Ih. To the passive model determined above, we added the h conductances diagrammed in Fig. 6, re-fitted the specific membrane resistance (because the value determined above was ‘contaminated’ by Ih) and fitted the kinetic parameters of Ih. We allowed different Ih densities in each compartment as this improved the fit somewhat without altering greatly the complexity of simulations employing the Ih model. We also fitted the reversal potentials of the membrane and h conductances. A single Ih parameter set fitted simultaneously to activation and deactivation series of of voltage steps is

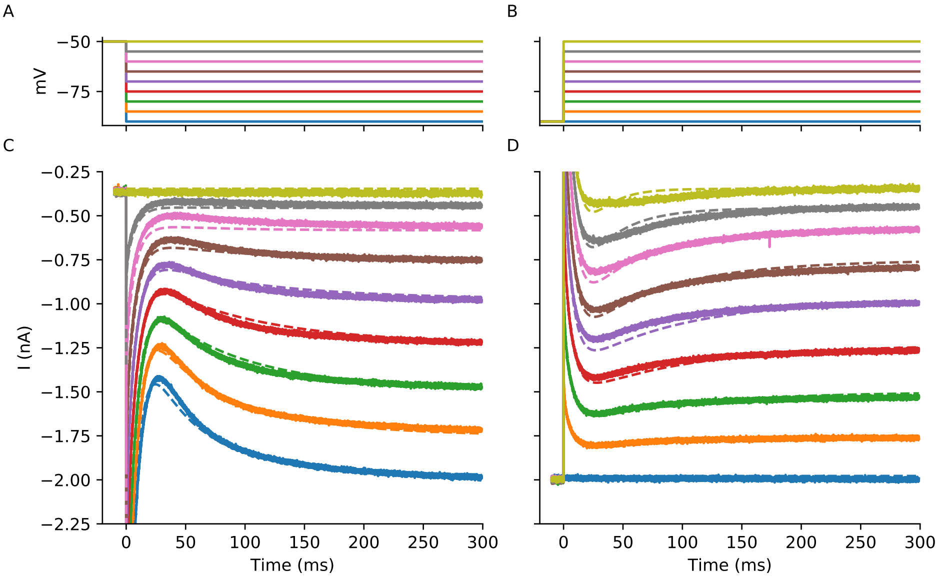

Figure 9: Fitting of the h conductance. A. Voltage jumps to probe activation of Ih. B. Voltage jumps to measure deactivation of Ih. C. Current responses to the activation jumps. D. Current responses to the deactivation jumps.

illustrated in Fig. 9. The somewhat disappointing quality of the fit is not untypical.

In a small number of cells (not shown) we applied the Ih inhibitor ZD7288, although this clearly blocked Ih, the passive cell properties drifted sufficiently to preclude a simple subtraction strategy for isolating Ih, which was the reason for performing the more global fit described above.

As a result of these fitting procedures we determined 12 cellular parameters as well as the electrode resistance and the unneutralised pipette capacitance. The grouped parameter values are tabulated in Table 1. (It is recalled that voltages have not been corrected for the junction potential.) The linearisation of the h conductance making use of these parameters is described in the Methods; this enabled us to treat the h conductance as a complex impedance. The grouped data for the parameter values will be presented below.

3.4 Impedance spectrum

In order to verify the accuracy of the recording, cell and Ih models, we compared their predictions to measurements of current responses to sinusoidal voltages applied in voltage clamp. An advantage of voltage clamp is that it allows fine control of the voltage and potentially a closer approach to the firing threshold than would be feasible in current clamp. In addition, the tight control of voltage should allow much more accurate determination of the contribution of voltage-dependent conductances, particularly Ih.

A specimen experiment and a comparison between predicted and measured impedance spectra are shown in Fig. 10. Although the model prediction were able to reproduce the form of the spectrum quite satisfactorily, with the high-frequency portion clearly requiring inclusion in the model of the amplifier response and filtering, there often remained visible deviations, particularly at low frequencies even when Ih was included

3.5 Control of firing rate

The apparent resonance at the firing frequency when firing is regular can greatly complicate the interpretation of response spectra, especially as it can drift over time. Inspired by the work of Couto et al. (2015), we decided to control the firing rate. We implemented a proportional + integrating controller using an Arduino real-time microcontroller to add a control signal to the current command (see Methods). The operation of the circuit is illustrated in Fig. 11 at two firing frequencies. After a period of stabilisation, this mechanism was usually able to control the firing rate with reasonable accuracy.

3.6 Firing mechanism

Equipped with a precise model of the amplifier and neurone, we investigated the the currents underlying the action potential and sought to construct a simple model capturing the essence of their operation. As diagrammed in Fig. 6 we assume that the active currents are restricted to the somatic compartment, without separately modelling the axon initial segment at this stage.

Using the transfer functions constructed for the amplifier model, we deconvolved voltage (and command current) recordings to calculate the precise voltage at the electrode and the current injected across it into the cell. Knowing the average current and voltage, it was then possible to work back through the cell to determine all of the voltages.

The deconvolved compartmental voltages and currents are illustrated for one cell in Fig. 12. The predicted voltage variations in the dendritic compartments are relatively small compared to the action potential in the soma (Fig. 12A). This is expected given the reported absence of back-propagation of the action potential; our model assumes that the dendrites are passive (Stuart and Häusser 1994). Simplified models of spiking neurones universally include a post-spike reset of the somatic potential to a relatively hyperpolarised value before releasing synaptic integration. When models include a dendritic compartment, the question arises of the value of its reset volt-

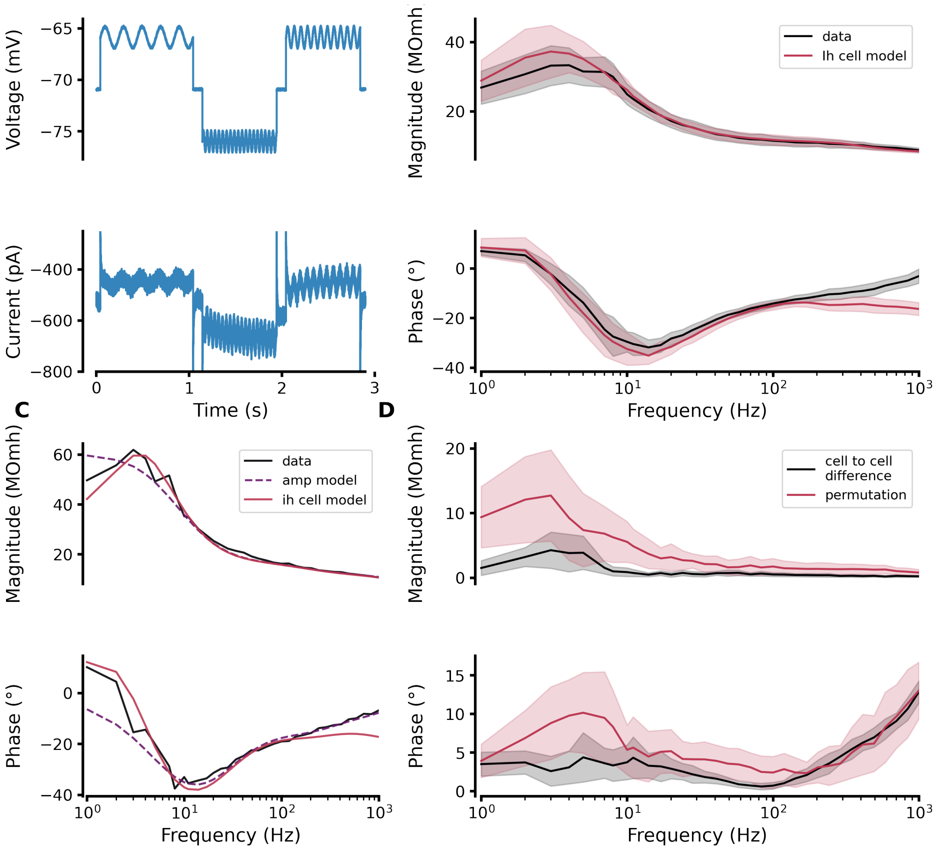

Figure 10: Measurement and fit of Purkinje cell impedance in voltage clamp. A. From top to bottom. Excerpt from sequence of sinusoidal voltage stimuli. Current response. Gain of the complex impedance from direct measurement as above (data), and of models constructed from fits of transients and of Ih. The ‘amp’ model doesn’t include Ih so deviates at low frequency, whereas the ‘Ih cell’ model with Ih does not include the amplifier response and does not account for the high-frequency response. Bottom shows the phase as a function of frequency for the same models. B. From top, average gain and phase of the complex impedance for ($n = 45$) cells for data (black) and predicted from a cell model with Ih but without the amplifier response. The bottom plots show the paired differences between the measurements and the models (black) and with random permutations between cells (pink).

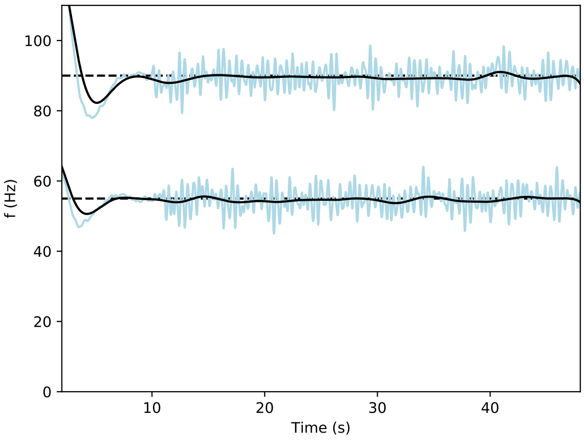

Figure 11: Illustration of feedback control of firing frequency. Two traces from the same cell. The controller was switched on shortly before the recordings shown. The firing rate has been smoothed with Gaussian kernels with standard deviations of 0.1 s (light blue) and 1 s (black). The frequency stabilises to the targets of 55 Hz and 90 Hz (dashed black lines). At 10 s a stimulus was applied, which caused high-frequency variations of the firing frequency.

age. It seems it must be a hyperpolarising step to avoid runaway positive feedback of the potential during spiking. However, as can be seen from the deconvolved voltages, the action potential itself injects a large, depolarising charge into the dendrites (as it must). As we shall see, this implies that the net negative charge necessary to ensure stability must be the result of post-spike processes. Further inspection shows that the dendritic compartments are more positive than the soma at all times except during the depolarised phase of the action potential. This means that the dendrites tend to depolarise the soma.

The action potential dominates the deconvolved active current in the soma, peaking at a few tens of nanoampères during the depolarising phase (Fig. 12C). Large currents are expected, although previous direct measurements with patch-clamp recordings were generally limited by voltage-clamp limitations caused in particular by the electrode resistance. The biphasic rising phase (barely visible on the time scale of the figure) presumably reflects the sequential activation of the sodium current in the axon initial segment followed by that in the soma.

More surprising to us was the situation following the action potential. Of course, potassium conductances underlie repolarisation and also the afterhyperpolarisation. However, the deconvolved traces show quite large repo-

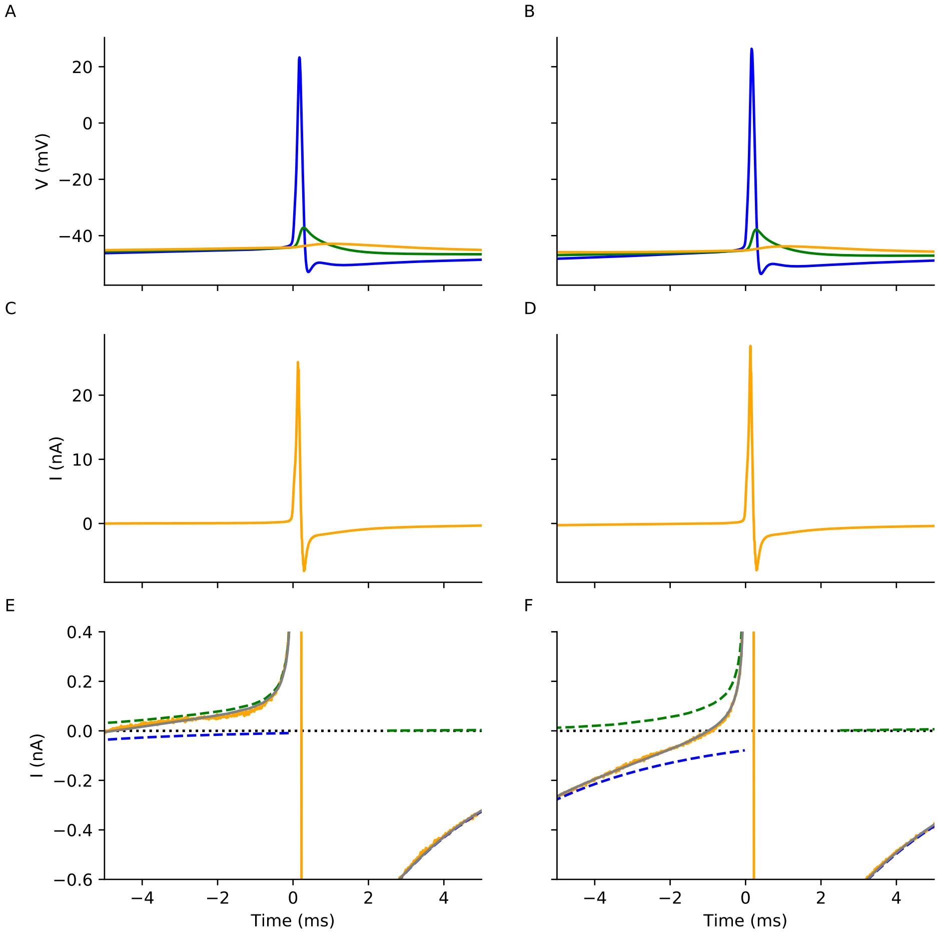

Figure 12: Deconvolution of average active currents. A and B. Average spike-triggered voltages of the somatic (blue), proximal dendritic (green) and distal dendritic (orange) compartments for a Purkinje cell firing at 55 Hz (A) and 90 Hz (B). See text for a description of the methods. C and D. Deduced spike-triggered somatic active current in the same cells at the same times, inward positive. D and E. Fits of the active current with simplified sodium (dashed blue) and potassium (dashed green) current models; their sum (grey) is also plotted.

larising currents that persist far into the interspike interval and, at higher firing rates, persist until the following spike (Fig. 12E,F). The presence of this hyperpolarising current, presumably mediated by a potassium conductance, causes the soma to remain at a potential more negative than the dendrite throughout most of the interspike interval. The negative somatic relative voltage is maintained despite the depolarising drive from the dendrite. This large hyperpolarising current is likely to play a central role in determining the rate of firing and the firing response more generally.

We sought simple mechanisms to model the active current. For the sodium current, we tested that employed in 'exponential integrate-and-fire' (EIF) models (Fourcaud-Trocmé et al. 2003). This represents the inward current as a(n instantaneous) function of voltage and is characterised by two parameters: a threshold voltage and a 'slope factor'. We represented this in a form that emphasises the roles of the two parameters:

$$I_{\mathrm{Na}} = k e^{-V_T/\Delta_T} e^{V/\Delta_T} \tag{36}$$

where Δ_T is the slope factor, V_T is the threshold voltage and the factor k was chosen to be 1 nA, to link the threshold voltage to a current amplitude observed early in spike initiation. The current is an exponential of the voltage, with an e-fold increase with each depolarisation by Δ_T, typically of the order of 1 mV. This reflects the intrinsic sensitivity of sodium channel activation to voltage. Written in this way, it is apparent that the notions of threshold and amplitude are essentially indistinguishable, because they only influence the prefactor of the exponential. We describe fitting both parameters below.

Following the action potential, there appear to be at least two components of hyperpolarising current. The longest lasting component appeared to decay exponentially with time: a relatively clean exponential is observed from about 2.5 ms after the action potential. The comparison of active currents averaged at two different firing rates (55 Hz and 90 Hz) shows that the decay of this component is, to a first approximation, time- rather than voltage-dependent, because the decays at the two frequencies follow very similar time courses, despite there being an increased rate (nearly double) of depolarisation at the higher firing frequency. We therefore fitted this hyperpolarising current with a simple exponential:

$$I_{\mathrm{K}} = A_K e^{-t/\tau_K} \tag{37}$$

We fitted the sum of these currents $I_s = I_{\mathrm{Na}} + I_{\mathrm{K}}$ to the average active current in the window free of preceding or succeeding spikes. The amplitude of I_{K} preceding the spike reflected the average of its activation by preceding spikes with different interspike intervals; this portion was therefore fitted with an amplitude parameter adjusted to take account of the distribution of interspike intervals in the average. Specifically, taking the time of the averaged spike as 0, the portion with positive time was fitted with (37) while for the portion with negative time the amplitude parameter was multiplied by a factor of $\langle e^{-\mathrm{ISI}/\tau_K} \rangle$ averaged across all ISIs. The fit and the components of I_s are shown in Fig. 12.

According to these fits, for which the grouped data is shown in Table 1, in a fraction of Purkinje cells the sodium current was only significantly activated as the action potential initiated. In other cells there appeared to be a sodium current throughout most of the interspike interval. Whether this represents a genuine cellular property or a fitting problem is unclear at this stage. (Because I_{Na} is strictly positive, it would be sensitive to imprecise determination of the zero-current level by an error of the cellular model.) Nevertheless, the fits were always very close.

The proposed active currents provide an excellent fit to the average spike waveforms. It is, however, also possible to extract the active somatic current and predicted sodium and potassium currents at all times during the recording. Such analysis is shown in Fig. 13, for the same cell at the two firing frequencies, during stimulation with a variable current (a mixture of sinusoids); the current required to maintain the firing rate can be judged by the average level of the injected current. As a general remark, we would predict that the sum of the modelled sodium and potassium currents would be equal to the extracted active current. Although the overall features are recognisable, the fit is not exact. Furthermore, there was in most cells a discernible correlation between the injected and active current, which is also not predicted. We do not have detailed explanations for these deviations from predictions, except that they are likely to represent an unidentified inaccuracy (or error) in the model.

The variable stimulus is clearly quite small compared to the potassium current, until the latter has decayed. At the lower frequency of firing there is a relatively extended window on average in which the potassium current has decayed and before the next spike occurs. The variable stimulus is presumably best able to influence the timing of the action potential during this window. However, when the firing frequency is increased, the potassium current does not have the time to decay to low levels before the next spike occurs, suggesting that the stimulus will have a much smaller window during which it can influence spike timing.

3.7 Simulations

We constructed a spiking model of the Purkinje cell using a 3-compartment passive model including Ih and augmented with the exponential potassium current and EIF-style sodium current at the soma, as described above. The parameters were tuned for each Purkinje cell according to their individual fits. The set of differential equations was integrated in time to yield the compartment voltages (and compartmental h conductances). A threshold on the

Parameter	Mean	SEM	Units
G_e	209	5	nS
A_s	1840	63	μm^2
A_d	19100	1470	μm^2
A_t	60800	2300	μm^2
G_{sd}	213	7	S
G_{dt}	268	19	S
a	3.1	1.6	s^{-1}
b	148	16	V^{-1}
c	136	12	V^{-1}
$V_{1/2}$	-69	1	mV
$g_{h,s}^{\max}$	0.97	0.02	$\mathrm{S\,m^{-2}}$
$g_{h,d}^{\max}$	0.63	0.10	$\mathrm{S\,m^{-2}}$
$g_{h,t}^{\max}$	0.39	0.14	$\mathrm{S\,m^{-2}}$
E_h	-23	1	mV
g_m	0.29	0.02	$\mathrm{S\,m^{-2}}$
E_m	-32	2	mV
$\bar{V}_s$	-46	6	mV
$\bar{V}_d$	-45	5	mV
$\bar{V}_t$	-44	5	mV
V_T	-41	6	mV
Δ_T	1.9	1.3	mV
A_K	-1.3	0.9	nA
τ_K	3.9	0.3	ms

Table 1: Recording, cell, h-conductance and active-current parameters, mean ± SEM for $n = 25$ Purkinje cells. $\bar{V}_x$ represents the time-averaged compartmental voltage during firing at 90 Hz, which was also the condition for the determination of the parameters of the active currents.

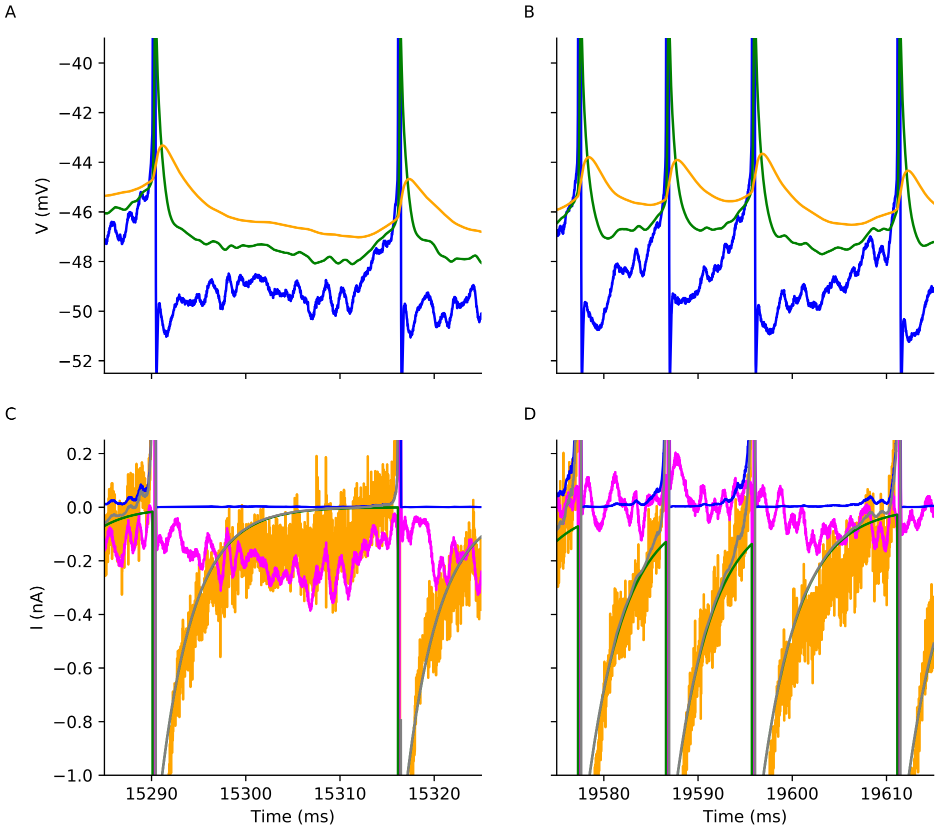

Figure 13: Deconvolution of real-time active currents. A and B. Continuous voltages of the somatic (blue), proximal dendritic (green) and distal dendritic (orange) compartments for a Purkinje cell firing at 55 Hz (A) and 90 Hz (B). C and D. Deduced somatic active current (orange) in the same cells at the same times, inward positive. The model sodium (blue) and potassium (green) currents, as well as their sum (grey) are also plotted. The injected (electrode) current (I_e) is plotted in magenta; it reflects a command of a mixture of sinusoidal currents and a current controlling the firing rate.

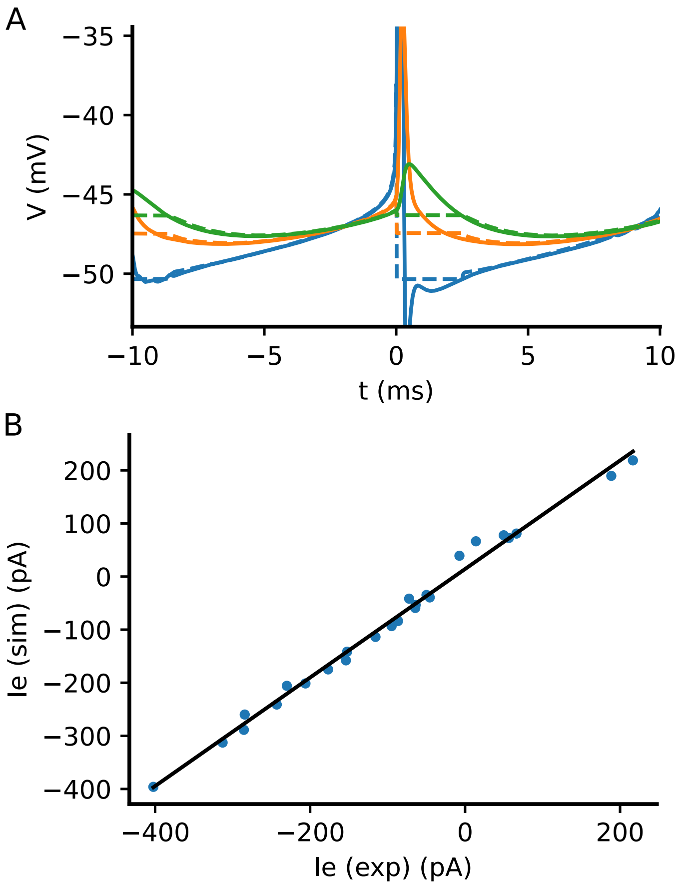

Figure 14: Firing simulations. A. Comparison of experimentally measured and deduced voltage traces (solid lines: blue soma, orange proximal dendrites, green distal dendrites) with model voltages (dashed lines, same colour code); the flat portions represent the time between spike initiation and voltage reset, when no simulation was performed. B. Model electrode current (blue) necessary to reproduce a 90 Hz firing rate plotted against the measured electrode current at the same 90 Hz firing rate, for $n = 20$ cells and matching models. Black: linear regression.

somatic voltage was set to define the time of an action potential. When that threshold was crossed, the time was advanced by 2.5 ms, the voltages of the three compartments were reset and the potassium current initialised. The reset voltages were determined from the voltages at 2.5 ms after the spike deduced from the average spike waveform as in section 3.6. The soma was always reset to the same voltage, while dendritic compartments were reset relative to their values at spike initiation by the amounts determined from their average time course. Following the reset, the simulation was restarted and advanced to the next spike. The rather long period between spike initiation and reset was chosen because of the simple form of the potassium current after that time point. Even at the higher firing frequencies studied (90–100 Hz), there were only extremely rarely, if ever, interspike intervals shorter than 2.5 ms.

The experimentally deduced and modelled compartmental voltages are illustrated for a specimen Purkinje cell in Fig. 14, where the freezing of the simulation and subsequent voltage reset can be seen in the flat portions of the voltage traces. The qualitative fit of the model and experimental traces is apparent.

The recordings were carried out under conditions where the firing rate was controlled. Before performing the simulations, the holding current in the model was adjusted to ensure a firing rate close to the same frequency. Although in neither experiment nor modelling was the control of the firing frequency during stimulation periods wholly precise, it can be seen in the plot in Fig. 14B that the injected currents were very tightly correlated. This provides some assurance that the firing model could reproduce the firing behaviour of the cell, because the parameters were obtained from fits that did not directly include information about the firing frequency.

3.8 Spiking response spectrum

As explained in the introduction, in preliminary work we had tried several methods of obtaining a general characterisation of the Purkinje cell firing response. All had unsatisfactory signal-to-noise ratios, at least in the context of a real experiment of limited duration. We designed a method for characterising precisely the firing response spectrum. As for the step responses, we performed the recordings in the presence of blockers of synaptic currents, rendering the conditions as deterministic as possible. As above, the firing frequency was also stabilised by feedback control.

We constructed stimuli by summing 50 sinusoids at frequencies without common harmonics, this was achieved by approximating a power series of π. The summed stimulus was sufficiently strong and irregular to disrupt the ‘firing-rate resonance’ yet the effective orthogonality of the individual components enabled parallel instead of sequential measurement, offering a great advantage in precision for a given recording duration. Each component

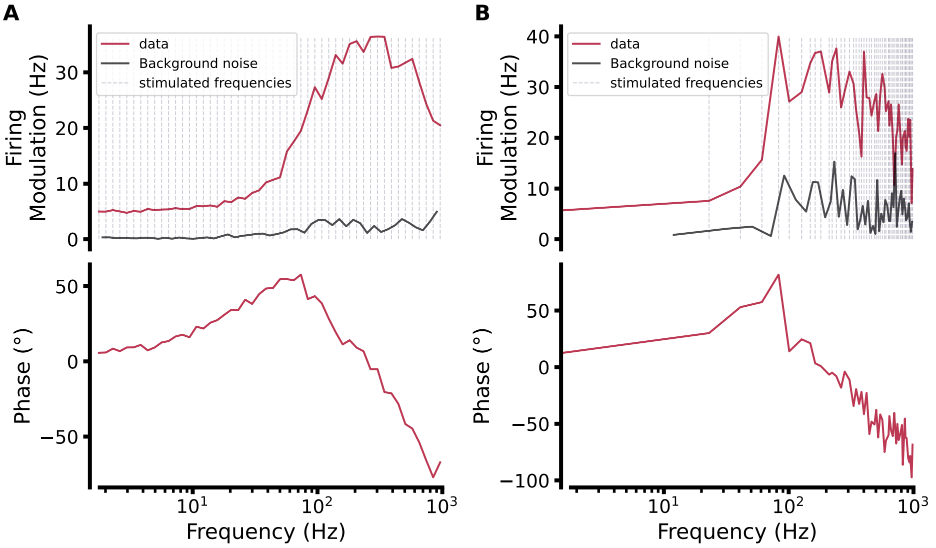

Figure 15: Purkinje cell firing responses to mixtures of sinusoidal currents. A. firing response spectrum (red) to stimuli with a ‘comb’ spectrum. 50 sinusoids were injected simultaneously with the frequencies shown (dashed vertical lines) and random phases. Their amplitudes were 15 pA and the cell was firing at 90 Hz. The stimuli had a ‘pink’ noise distribution. Between the stimuli, the background noise was also decomposed (black). B. A similar experiment in the same cell, but with the sinusoids approximating a white noise spectrum. C. The phase for each response component for the spectrum in A. D. Phase for the spectrum in B.

was only sensitive to noise at a sharply defined frequency, further improving the signal-to-noise ratio. Moreover, the noise amplitudes could be estimated from the spectrum between stimuli. The ability to sample the spectrum at 50 points as well as the control of the firing frequency facilitated interpretation of the spectrum. The frequency, amplitude and phase of each component could be defined separately. We randomised the phases of the summed sinusoids. We selected frequencies to approximate white (equal density at all frequencies) and pink (equal density per decade) noise within the 10–1000 Hz band. As above, intrinsic noise was minimised by the application of blockers of synaptic activity and no additional noise was injected.

The results are illustrated for a ‘pink noise’ stimulus (see Methods) in Fig. 15, which shows the spectrum of response amplitude. Comparison of the density at the stimulation frequencies and of the background noise between the stimulation frequencies demonstrates the exceptional signal-to-noise ratio offered by this experimental design. The dense sampling and fixed firing frequency shows that the ‘firing-rate resonance’ is greatly attenuated or even absent under the conditions of the figure. There is a flat response plateau at low frequencies (1–20 Hz), with no apparent influence from Ih. At higher frequencies we can observe a very robust, broad resonance.

Group data are shown in Fig. 16, where the the properties of the response spectra are explored. Altering the distribution of frequencies in the stimulus seemed to have little effect (individual data shown in Fig. 16A, B and averages compared directly in Fig. 16D. Thus, the spectra overlap quite closely except for a more prominent 'firing-rate resonance' with the white noise frequency distribution. We speculate that this may be in part due to a reduced overall power of the stimulus injected into the cell, because higher frequencies are naturally more strongly filtered by the cellular capacitances. For a smaller number of cells we applied stimuli with different amplitudes. Despite the small sample size, consistent behaviour was observed, in that the peak of the high-frequency resonance was barely affected, increasing much less than proportionately with stimulus amplitude. A proportional change with amplitude would be expected for a linear process. The lack of proportionality suggests the presence of some form of saturation. An obvious source of saturation occurs when the firing rate is depressed to zero—it cannot go lower. However, it seems unlikely that this could reduce the amplitude of the modulation even by 50%, since half of every sinusoid would excite beyond the baseline firing rate, yet the effect seems stronger. Interesting, at low frequencies there is a roughly proportional increase of response with stimulus amplitude. A reduced data set for a white stimulus distribution (Fig. 16F) gave results that were consistent with the preceding description.

The firing response of the models with parameters tuned to each recorded Purkinje cell exhibited broadly the same features as the experimental measurements Fig. 17, with a relatively flat spectrum at low frequencies and amplified response at frequencies around 100 Hz. The models were moreover able to capture some of the dependency of the high-frequency resonance on the firing frequency. As in the real neurones, the resonance was stronger in model cells firing at 90 Hz than at 55 Hz.

However, there were several clear, quantitative differences between the recordings and models. In particular, at higher frequencies the model is unable to reproduce the amplitude of the resonance around 100 Hz, attaining roughly only half the gain. There is moreover a prominent biphasic peak-dip sequence of the model response around the firing frequency, whereas the firing-frequency resonance is barely observable in the cell and there is no evidence for a decreased response at frequencies slightly above the firing frequency. Finally, the cellular response has a profound cut-off at the highest frequencies; this is largely absent in the model.

In summary, the cell displays a robust high-frequency resonance in its firing response that is not well captured by the model.

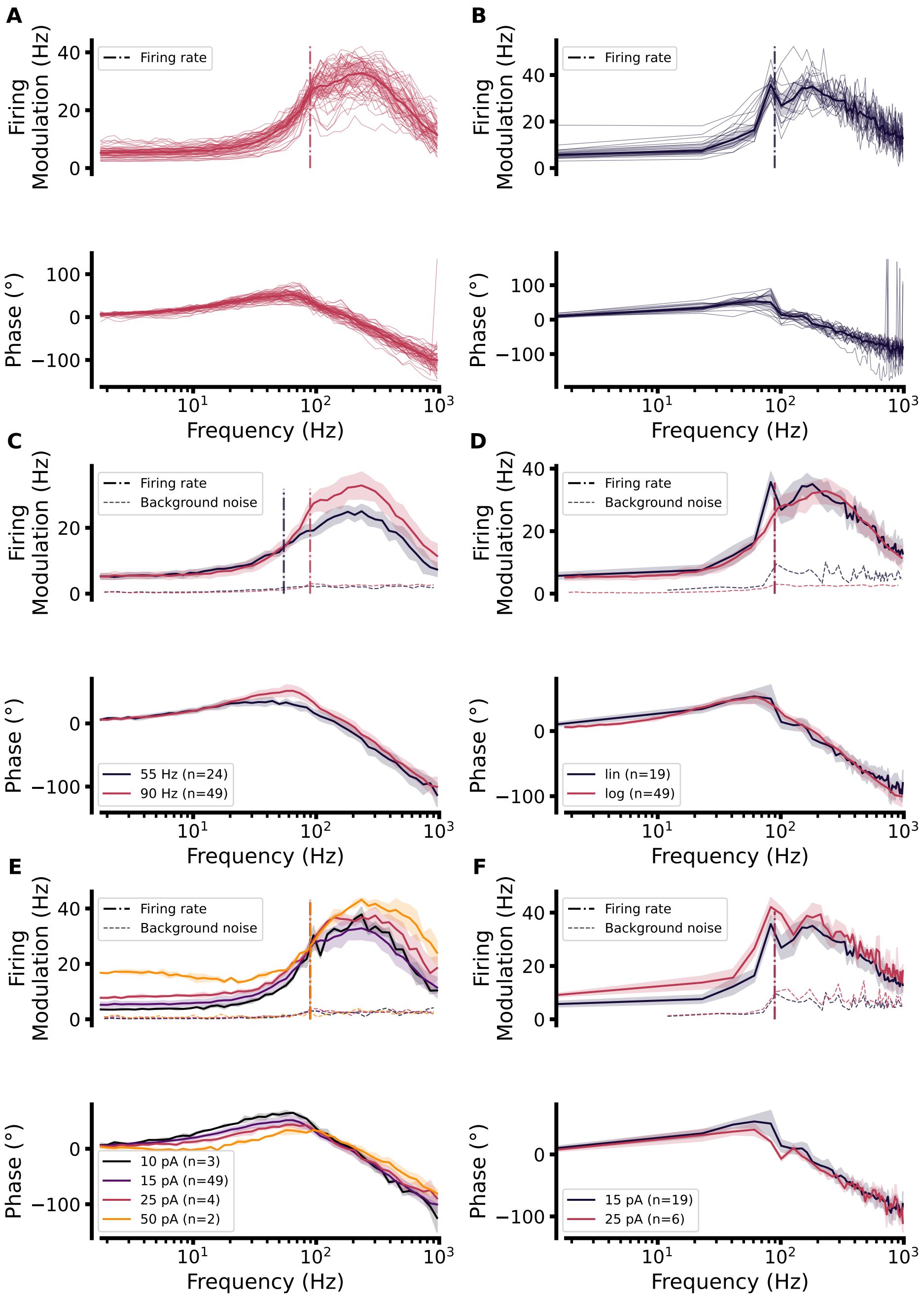

Figure 16: Exploration of response spectra. A and B. Gain and phase for group data, for 'pink' (A, red) and 'white' (B, black) stimulus mixtures (as in Fig. 15; the controlled firing frequency is indicated by a vertical dot-dashed line. C. Comparison of the gain and phase spectra for 'pink' ('log') stimuli at different firing frequencies (55 Hz black and 90 Hz red). of measured and modelled firing response spectra. D. Comparison of the gain and phase spectra in response to 'pink' (red, 'log') and 'white' (black, 'lin') stimuli. E and F. Effects of stimulus amplitude on the response spectrum for 'pink' ('log', E) and 'white' ('lin', F) stimuli. Throughout, spectra are plotted as median ± MAD.

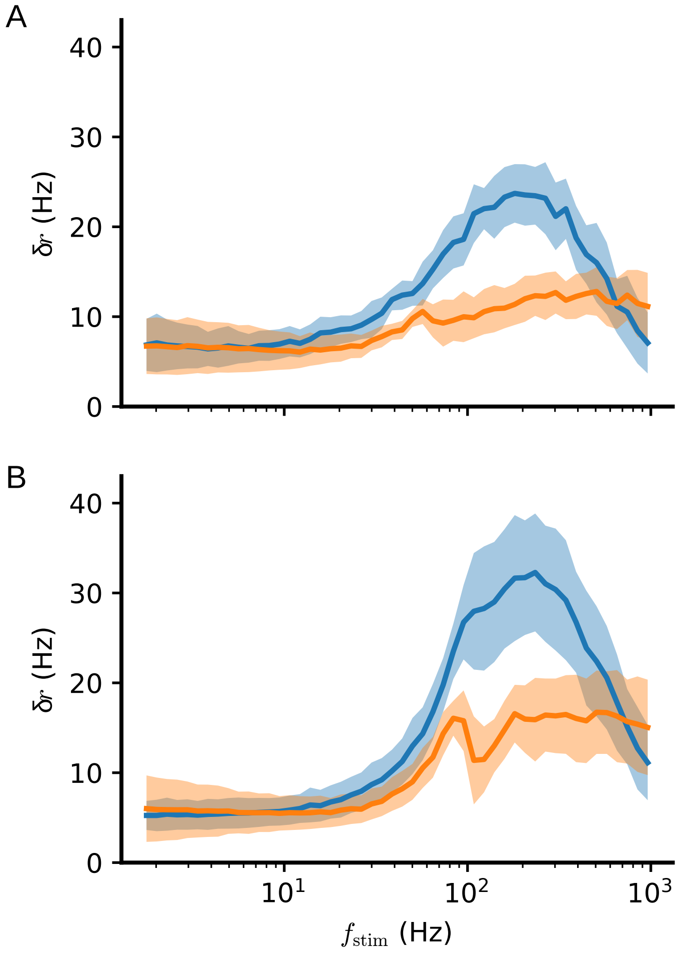

Figure 17: Comparison of measured and modelled firing response spectra. A. Experimental (blue) and modelling (orange) spectra for a ‘pink noise’ mixture of 50 sinusoids of 15 pA amplitude with Purkinje cells firing at 55 Hz. Mean ± sd. B. Similar comparison for cells firing at 90 Hz.

4 Discussion

4.1 Precise Purkinje cell model

Preliminary studies of the Purkinje cell firing response had revealed to us that its measurement could be imprecise and that the phenomenon could vary between cells. Any deeper investigation of its mechanisms would require precise measurement and modelling at the single-cell level for unequivocal interpretation. We aimed to construct accurate models that were of sufficient simplicity to be constrained by direct measurement and to be sufficiently mechanistic to offer insight. In parallel, we sought to design our experiments to maximise measurement precision. Although one can justifiably question the influence on the results of our amplifier characterisation or fitting of Ih, that is to some extent a luxury of hindsight: it is quite difficult to make that judgement without having concrete measurements. Furthermore, one only needs to combine a few 20 % errors to render most quantitative comparisons impossible to interpret.

We attempted to characterise both voltage-clamp and current-clamp modes of the amplifier. The voltage-clamp mode was preferred for the cellular characterisation, and its high-frequency performance is important for accurate measurement of the somatic compartment of the Purkinje cell, which is key to describing spiking behaviour. Our characterisation of voltage-clamp mode is work in progress, but it enabled a satisfactory fit to all time scales of the cellular capacity transient. Unsurprisingly, our investigation confirmed the challenging and complex design of the voltage-clamp amplifier. One imperfection we noted in the voltage-clamp mode was the poor quality (rather filtered) of the command copy outputs.

The current-clamp mode is a simpler circuit. However, the parasitic capacitance in parallel with the injection resistance caused a meaningful distortion of current injection, leading to a 30 % increase of current at 1 kHz, which would easily be confused for a high-frequency amplification of a response. In another configuration, which luckily we did not use, the effect would have been nearly 300 %. The capacitances involved are very small, but their impedance needs to be referred to those of their high-value parallel resistances. Furthermore, the applied voltages in the current source are large, leading to significant charge injection. Although it is not possible physically to eliminate such capacitors (at least when using resistances to inject current), it may be possible to insert a carefully tuned low-pass filter upstream of the resistance to compensate.

The three-compartment model of the Purkinje cell gives an accurate representation of the impedance of the somatic compartment. Although representation of dendritic processes is likely to be oversimplified, such a model does nevertheless offer some mechanistic insight, a feature we have exploited.

We carried the same simple-but-mechanistic approach through to describing the active currents and modelling of spiking, where quite simple mechanisms could account fully for the average interspike behaviour from about 2.5 ms after the action potential, enabled principled selection of somatic and dendritic reset voltages, and thus allowed a simple spiking model to reproduce faithfully the firing frequency.

After multiple failed approaches we were able to design a measurement protocol that enabled accurate determination of the firing response spectrum. The use of a ‘comb’ stimulus (in the frequency domain) had several decisive advantages, which we outlined in the Results. These measurements revealed a striking high-frequency resonance in the Purkinje cell, confirming previous reports (Ostojic et al. 2015).

Armed with these precise firing response measurements, accurate spiking models and precise firing response measurements, we discovered that the models could not explain the observations, in particular that the experimentally observed resonance was markedly stronger than predicted by the model. Less precise measurement and modelling would have make it difficult to be confident of this conclusion. We return to possible reasons for the unexplained resonance.

4.2 Action potential cycle

The accurate model of Purkinje cell somatic impedance we constructed enabled us to deduce the active current flowing through it. This in turn yielded a simple but effective approximation. The classical EIF firing mechanism accounted for the observed sodium current, although we fitted both of its parameters rather than just the slope factor. After the action potential, we found that a single exponential potassium current accounted for a prolonged hyperpolarising current in the soma. This current behaved to an excellent approximation as a purely time-dependent current, with a time constant of about 4 ms. This time constant is such that when the Purkinje cell is firing at low frequencies (e.g. 50 Hz), the current decays and a window of heightened sensitivity to inputs is opened, any time during which the next spike could be triggered. At higher frequencies (e.g. 90 Hz), however, the current is always active and spike initiation occurs over the balance of larger currents, offering only a small window of high sensitivity to inputs. A window of heightened sensitivity to inputs would be consistent with the conclusion that the timing of Purkinje cell spikes is influenced by the time of the previous spike only for a short period; the reported ‘memory time’ would correspond to the effective duration of the exponential potassium conductance (Blot et al. 2016).

Two mechanisms could be imagined to underlie the apparent voltage independence of the potassium current. The first would be a calcium-activated conductance, the second would involve an approximate voltage insensitivity arising from the fact that the range of interspike voltages may be positioned at the maximum of the time constant–voltage curve.

Purkinje cells varied in the degree to which the deduced sodium current was active during the interspike interval. In some cells, it was essentially negligible except shortly before initiation. In others it provided a significant input throughout much of the interspike interval. This may corroborate the report by Khaliq et al. (2003) that a resurgent sodium current maintains Purkinje cell firing.

Because we included dendritic compartments in our model, it offers potential insight into their behaviour during the action potential cycle. Two initially unexpected observations emerged. Firstly, that the action potential produced a net depolarisation of the dendrites. This is not surprising after reflection, because the action potential itself must drive significant charge into the dendrites, but it does contradict spiking models in which dendrites are reset to a hyperpolarised voltage after a short refractory period. A related observation was that, except briefly during the action potential, the soma was at a more hyperpolarised voltage than the dendrites throughout the cycle. Because the somatic time constant is very short ($C_s/G_{sd} \approx 100\mu\,\mathrm{s}$), it would normally be expected to relax to the dendritic voltage. Continuous current—provided by the potassium current—is required to maintain the voltage difference.

Although the simple currents we included in the model yielded an excellent fit of the average interspike interval at various firing rates, the real-time fit during simulation was less exact. Whether this reflects a calculation error, a model inaccuracy or current noise in the cell is unclear.

4.3 High-frequency resonance

We measured a remarkable high-frequency resonance in the firing response. When the Purkinje cell was firing at 90 Hz, the average ratio between low and high-frequency responses was greater than 6-fold. It has previously been shown that at least part of this resonance results from the morphology of the Purkinje cell—two very distinct somatic and dendritic compartments—interacting with even the simplest spiking mechanism (basically, a threshold). However, we now show that this is unlikely to be the only mechanism, because our modelling is unable to recreate several features of the Purkinje cell response mechanism, including the strength of the resonance.

The measurement and model match at low frequencies, at which, it appears, Ih plays no role in shaping the frequency response. This is presumably because the variation in its activation is too slow compared to the action potential cycle, and also because of the depolarised average voltages. There is a sharp roll-off of the measured response at high frequencies. It seems plausible that finite sodium channel activation kinetics, which are absent from the model, would contribute to this behaviour. A residual resonance at the firing frequency is very apparent in the model response but barely visible in the recordings. It is likely that the firing rate of the real cell varied somewhat under the influence of membrane current noise, despite the rate control, and that this would disrupt the firing resonance.

However, there is no obvious mechanism we can suggest to account for the stronger high-frequency resonance in the recordings. Possible mechanisms to explore are the kinetics of sodium channel activation and inactivation, and also a possible role for the axon initial segment, which we have for now simply subsumed into the soma.

4.4 Perspectives

The Purkinje cell population can organise in high-frequency oscillations mediated in part by reciprocal inhibitory connections. These must be somatic to support such high frequencies of oscillation, underlining the relevance of studying the firing response to somatic input. Clearly the firing resonance we observe in the same frequency range will amplify the emergence of such oscillations. Even in the absence of oscillation, the resonance implies a high sensitivity of the Purkinje cell population to inputs with high-frequency components. The action potential cycle we have elucidated suggests that Purkinje cells will have a larger window of input sensitivity when firing at lower frequencies.

Now that an accurate model has been established, the efficacy and accuracy of simplifications can be explored. For instance, are three compartments that much better than two? Modelling based upon the somatic impedance can easily be adapted to different neuronal morphologies and, with a degree of approximation, be used to predict the action of more distal inputs, notably synaptic inputs in the dendrites. An unexamined issue in this context is how to represent the post-spike reset in neurones that, unlike the Purkinje cell, support back-propagating action potentials.

5 Author contributions

- Conceptualisation: all authors.
- Experiments: AM
- Analysis: AM, JR, BB
- Simulations: JR, AM

GB performed pilot experiments.

6 Acknowledgements

This work was supported by the Fondation pour la Recherche Médicale through grant 'Equipe FRM DEQ20160334927'. This work has received support under the program 'Investissements d'Avenir' launched by the French Government and implemented by the ANR with the references ANR–10–LABX–54 MEMOLIFE and ANR–10–IDEX–0001–02 PSL* Université Paris.

References

(1) Blot, A., de Solages, C., Ostojic, S., Szapiro, G., Hakim, V. and Léna, C. (2016). Time-invariant feed-forward inhibition of Purkinje cells in the cerebellar cortex in vivo. *The Journal of Physiology 594*, 2729–2749, DOI: 10.1113/JP271518.

(2) Couto, J., Linaro, D., De Schutter, E. and Giugliano, M. (2015). On the firing rate dependency of the phase response curve of rat Purkinje neurons in vitro. *PLoS computational biology 11*, e1004112, DOI: 10.1371/journal.pcbi.1004112.

(3) Dempster, J. WinWCP `https://spider.science.strath.ac.uk/sipbs/software_ses.htm` (accessed Nov. 20, 2022).

(4) de Solages, C., Szapiro, G., Brunel, N., Hakim, V., Isope, P., Buisseret, P., Rousseau, C., Barbour, B. and Léna, C. (2008). High-frequency organization and synchrony of activity in the purkinje cell layer of the cerebellum. *Neuron 58*, 775–788, DOI: 10.1016/j.neuron.2008.05.008.

(5) Fourcaud-Trocmé, N., Hansel, D., van Vreeswijk, C. and Brunel, N. (2003). How spike generation mechanisms determine the neuronal response to fluctuating inputs. *The Journal of Neuroscience: The Official Journal of the Society for Neuroscience 23*, 11628–11640.

(6) Häusser, M. and Clark, B. A. (1997). Tonic synaptic inhibition modulates neuronal output pattern and spatiotemporal synaptic integration. *Neuron 19*, 665–678, DOI: 10.1016/s0896-6273(00)80379-7.

(7) Huang, S. and Uusisaari, M. Y. (2013). Physiological temperature during brain slicing enhances the quality of acute slice preparations. *Frontiers in Cellular Neuroscience 7*, 48, DOI: 10.3389/fncel.2013.00048.

(8) Khaliq, Z. M., Gouwens, N. W. and Raman, I. M. (2003). The contribution of resurgent sodium current to high-frequency firing in Purkinje neurons: an experimental and modeling study. *The Journal of Neuroscience: The Official Journal of the Society for Neuroscience 23*, 4899–4912.

(9) Llano, I., Marty, A., Armstrong, C. M. and Konnerth, A. (1991). Synaptic- and agonist-induced excitatory currents of Purkinje cells in rat cerebellar slices. *The Journal of Physiology 434*, 183–213, DOI: `10.1113/jphysiol.1991.sp018465`.

(10) Llinás, R. and Yarom, Y. (1986). Oscillatory properties of guinea-pig inferior olivary neurones and their pharmacological modulation: an in vitro study. *The Journal of Physiology 376*, _eprint: https://onlinelibrary.wiley.com/doi/pdf/10.1113/jphysiol.1986.sp016147, 163–182, DOI: `10.1113/jphysiol.1986.sp016147`.

(11) Ostojic, S., Szapiro, G., Schwartz, E., Barbour, B., Brunel, N. and Hakim, V. (2015). Neuronal Morphology Generates High-Frequency Firing Resonance. *Journal of Neuroscience 35*, 7056–7068, DOI: `10.1523/JNEUROSCI.3924-14.2015`.

(12) Phoka, E., Cuntz, H., Roth, A. and Häusser, M. (2010). A new approach for determining phase response curves reveals that Purkinje cells can act as perfect integrators. *PLoS computational biology 6*, e1000768, DOI: `10.1371/journal.pcbi.1000768`.

(13) Puil, E., Meiri, H. and Yarom, Y. (1994). Resonant behavior and frequency preferences of thalamic neurons. *Journal of Neurophysiology 71*, Publisher: American Physiological Society, 575–582, DOI: `10.1152/jn.1994.71.2.575`.

(14) Richardson, M. J. E., Brunel, N. and Hakim, V. (2003). From Subthreshold to Firing-Rate Resonance. *Journal of Neurophysiology 89*, Publisher: American Physiological Society, 2538–2554, DOI: `10.1152/jn.00955.2002`.

(15) *Single-channel recording*, 2nd ed; Sakmann, B. and Neher, E., Eds.; Springer: New York, NY, 2009, 700 pp.

(16) Stimberg, M., Brette, R. and Goodman, D. F. (2019). Brian 2, an intuitive and efficient neural simulator. *eLife 8*, e47314, DOI: `10.7554/eLife.47314`.

(17) Stuart, G. and Häusser, M. (1994). Initiation and spread of sodium action potentials in cerebellar Purkinje cells. *Neuron 13*, 703–712, DOI: `10.1016/0896-6273(94)90037-x`.

Part III

Discussion

5 General remarks

5.1 A general and cell specific model ?

Our approach is to use transient voltage steps and impedance as tools to understand the passive properties of the cell, and to identify possible active components in order to incorporate them in a model. Then the spike triggering (EIF) and AHP currents are fitted to the spike-triggered average of the same cell. This creates an individual model for each probed cell around a defined model structure. The idea is that the structure should explain the intercellular disparities. Usually models are fitted on average data traces and the inter cellular disparities are treated as biological noise. This is a challenge experimentally speaking because we needed to incorporate the impedance and transient protocols for every experiment. This also gives a more general idea of how each variable can vary from one cell to another. The fit does not necessarily represent reality but it can give some insights, especially if the model then reproduces well the cell's response. Another question to be considered when taking into account intercellular specificity: can this variability have an impact on the population response? This can potentially have even more impact with our type of experiments, where the frequency response of one cell can be seen as a response of a population of cells identical to the one we are probing. Essentially, by investigating different cells we are also investigating the impact of a different set of variables on the population response.

The model also aims to be a generalised one. We could then use the model to investigate dendritic responses or other stimuli. Moreover, as well as the model, the experimental framework can be extended to any cellular type. An interesting idea could also be to explore this in a even more controlled environment. We could imagine a set of cultured neurons from a morphologically simple type, to which different kinds of channels could be expressed and test the impact on the firing properties and if the model is resistant to those changes. The more a model is able to represent cellular difference the more general and robust it will be.

5.2 Noise

Although noise seems to be a key factor in the firing response, how this impacts it is still unclear. Without noise, external or internal, neuronal firing profiles are dominated by their firing rate resonance. Noise reduces this resonance and unveils other possible profiles. But if there is some other kind of resonance, does the spectral shape of the noise impact or even shape, the firing response? Noise can reduce the resonance of the firing rate but resenons arising from other mechanisms too. That there is noise “in vivo” is undeniable. This noise could shape or simply be responsible for some of the resonance. From simulations (data not shown) we had insight that such a phenomenon could occur. We were interested in reproducing more realistically how the noise is represented at the soma. As the majority of synaptic input comes from the dendrites, we expect the summed noise to arrive filtered at the soma. In this case the dendrites act as a low-pass filter. Depending on the cut-off frequency of the filtering, the high-frequency resonance of the model cells were affected. We tested some experiments where individual frequency's currents were injected in the presence of different filtered noise, but the noise amplitude needed to suppress the firing rate resonance was too important and the data was not exploitable. But more importantly, this was done with the first protocols where the measurement was not precise enough to see a difference. The idea of changing the distribution of the frequencies in the "comb" profile experiments was a way of testing different types of filtering (colours) of the noise. In the logarithmic scale distribution, more low frequencies were injected, so mimicking low-pass filtered noise where the linear scale was "white". Interestingly it did not affect the overall resonance response other than the logarithmic scale was more efficient for removing the firing-rate resonance.

Noise is usually represented by the coefficient of variation of the firing defined by:

$$CV = \frac{\sigma}{\mu}$$

Where σ is the standard deviation and μ the mean

During our experiments we don't control the cv of each cell. We could imagine some kind of controller, on the same basis as the firing rate one, where the cv is estimated online and some white (or coloured ?) noise is injected at the soma to adjust the firing stability. The cv changes for the same cell depending on its firing rate: the higher the rate, the lower the cv. It could be understood by the fact that at lower rates the "perturbation window" in between spikes is longer. By homogenising the cell cv between rates, it could be possible to separate an effect from the simple fact that the cell is firing with some randomness, or a cellular one. The randomness of firing represents an effect of the population, the more random the more chance to have a cell near threshold.

5.3 High-frequency resonance

Our experiments confirmed the presence of an astonishingly reproducible and clear high-frequency resonance among Purkinje cells. The range of frequencies we probed increased the precision of our measurement compared to previous work. This improvement and the process of reproducing cell by cell the response with a model, revealed the lack of understanding we had to explain this resonance. This is not completely unsurprising, considering the fact that we started this project because a previous model was failing to reproduce rapid responses.

The fitting of the cellular currents showed two interesting, linked features. The first is that the AHP potassium current stays active longer than expected and seems to be mainly time dependent. The second that the dendrites could be highly depolarised after the spike compared to the soma. This gap leads to a constant depolarising current from the dendrites to the soma counteracting the hyperpolarising potassium one in the soma. This could also be a part of the reason Purkinje cells fire intrinsically at rather high rates. The "charging" of the dendrites after each spike would keep a constant depolarisation in the soma between them. But this does not explain any resonance. Previous work (Ostojic et al., 2015) showed that the morphology, namely the massive dendritic arborisation, was responsible for that resonance. However, it is clear now that although it does play a role, it is not sufficient for the general shape nor does it account for its amplitude. We are looking for possible explanations of the sharpness of the spike initiation, including that the localisation of the spike initiation in the axon initial segment would play an important role.

It was shown that the Purkinje cell layer exhibits a high-frequency oscillation (200 Hz) de Solages et al., 2008. This was explained by recurrent inhibitory connexions between Purkinje cells. The fact that even without any synaptic input the cells have a sensitivity for this range of frequency also raises the question of how this oscillation is generated and if it is a epiphenomenon of the Purkinje cell's preferred frequencies. It is important to note here that our experiments injected current in the soma of the cells. Purkinje cells mainly receive inhibitory inputs to the soma. From our model, we will mimic different kinds of protocols to understand better the interplay between inputs from the soma and the dendrites.

6 Perspectives

6.1 Potassium channels

One of the reasons we sought precise, reproducible measurements, which gave a clear effect, was to be able to perform pharmacological experiments and see the potential impact of specific channels on the firing properties. In previous experiments, prior to my project, short inhibitory pulses were injected at the Purkinje cell's soma, giving insight that voltage-gated potassium channel (K_V) could have an impact on rapid responses. This was already a rather counter-intuitive idea; potassium channels are better known to be involved at slow time scales. Potassium pharmacological blockers were used on the biphasic step protocol as well as the "comb" frequency profile protocol. The addition of potassium blocker sometimes resulted in the loss of the cell's stability. Also, the firing-rate clamp was calibrated on "control" cells' behaviour; for some cells it was not possible to stabilise the cell to the given frequency. For these reason, the number of comparisons is still too small.

On biphasic steps, we had to shorten protocols and focus on one firing rate (100 Hz). Three cells were tested with 4-Aminopyridine (4-AP)(Figure 33). 4-AP is a non-selective K_V blocker. Blocking K_V channels has a direct effect on spike shape, it removes the after hyperpolarisation (AHP). Also, interestingly, the rising phase of the spike is slowed. Although the effect on the step response is unclear especially with the small number of cells, a slight reduction of the response could emerge with a greater number of experiments. Other cells were tested with Tetraethylammonium (TEA), a non-selective potassium channel blocker, with similar results on biphasic steps (data not shown).

In a different batch of experiments the same number of cells (n=3) were tested with 4-AP on the "comb" protocol (Figure 34). The impedance did not seem to change between the two conditions except for one cell where it suppressed the low-frequency membrane potential resonance. This is probably due to a slowly rectifying current as explained in section 1.2.2. On the firing, it seemed to lower the responses for every frequency for at least two cells. This could be understood as a shift in the membrane resistance, except the impedance remained unchanged. If the effects are confirmed, one explanation could be that the the K_V channels implicated in the AHP have an indirect effect on the spike triggering. Indeed, the triggering of the spike is dependent on voltage-gated sodium channels. These channels inactivate quickly (Figure 2.1.1) and stay need the AHP in order to get activated again for the next spike. We can imagine that removing the AHP by blocking the K_V channels would diminish the pool of sodium channel ready to be activated on the next spike. This could be potentially a very promising path

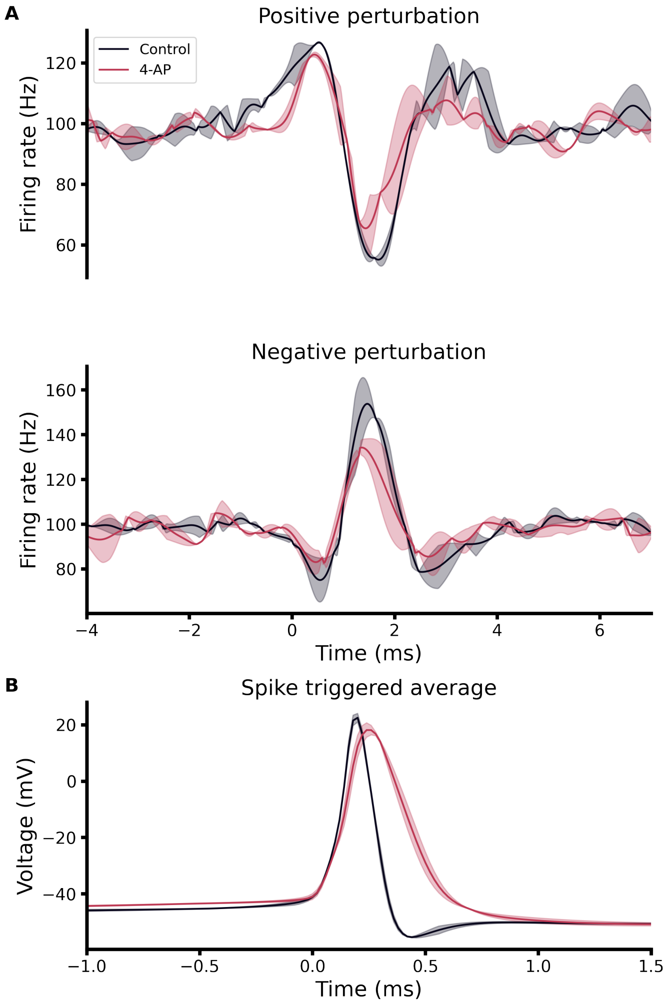

Figure 33:
Purkinje cell biphasic steps with 4-AP

Biphasic steps consist of a direct succession of a 1 ms step current of 15 pA followed by a similar step of the opposite sign. A. The peri-stimulus time histograms (PSTH) of the steps for both “first direction”. B. The spike-triggered average for each condition, the color code is consistent with (A). Solid lines surrounded by light area represent the median and the MAD of the data to explore where potassium currents could have a greater impact than expected on the firing properties of neurons, especially in tonic firing cells. This could be seen in a firing rate dependency of the firing frequency profiles when potassium currents are blocked. The greater the firing rate the less sensitive the spike triggering would be. We already see that in the normalised frequency profiles, the amplitude at low frequencies are not similar. There is a need for a more in-depth investigation of this phenomenon to a greater range of firing rates.

This could also be contrasted with a more general finding that there is a low-frequency membrane resonance in the Purkinje but nothing is to be seen in the firing. We showed that part of that low-frequency resonance could be explained by the Ih current, at least partially. One possible explanation is that when the cell is firing its membrane voltage is depolarised. At such potential Ih current is almost null so it would need a great amplitude perturbation to activate the current. Although at a depolarised state the low-frequency membrane resonance disappears, the impedance is not flat like in the firing profile. I think that the parallel between the impedance and the firing frequency profiles can be interesting, and can explain the firing resonance in some cases, but it does not take into account what happens during the spike. In my experiments, I tried to probe the impedance at depolarised states, such as -45 mV, but it would trigger spikes even in voltage clamp. First of all, the impedance at -70 mV is not necessarily the same at -40 mV, near the spike threshold. If we wanted to have the impedance around that threshold we would need to suppress the sodium channel responsible for the spike. But the missing link is always what is triggered by the spike and that cannot be rendered by the impedance.

6.2 Pyramidal cells

One of the goals of this project is not only to explain the Purkinje cell but to seek generalisable mechanisms to explain how firing is modulated in neurons. We performed experiments of "comb" firing frequency profiles on pyramidal cells in the deep cortical layers of the sensory cortex, more precisely in the barrel cortex region (Figure 35).

The cells fire at lower rates than the Purkinje cells and not in a tonic manner without some external depolarising current added. The low firing rate makes it quite difficult to say for certain that we can see a resonance different from the firing rate of the cells. But it seems that a resonance appears after the firing frequency. And that resonance is then rate dependent because it seems more diffuse than a firing rate resonance. Although the impedance profiles (Figure 36) of the cells do not show any resonance, it was shown that a resonance appears at depolarised states around between 2-10 Hz. Still the firing resonances we are seeing here are at higher frequencies. These results

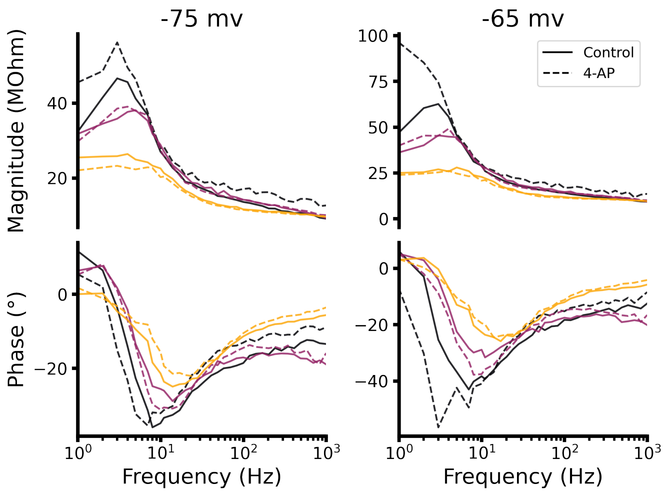

(a) Impedance

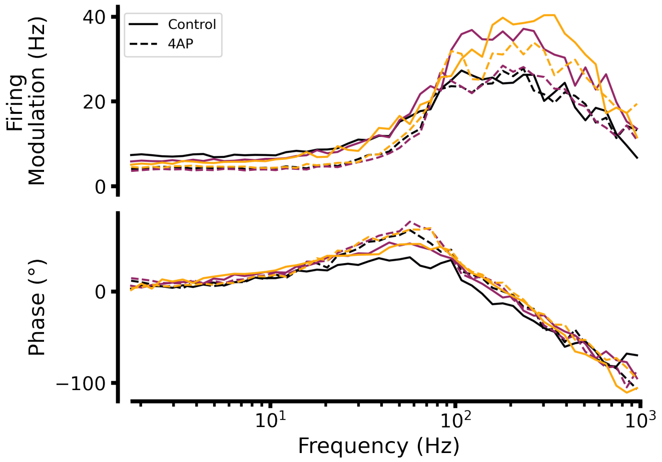

(b) Firing profile

Figure 34:
Purkinje cell firing modulation profile with 4-AP
3 cells were probed before (Control) and after the addition of 4-AP (5µM) to the extracellular medium

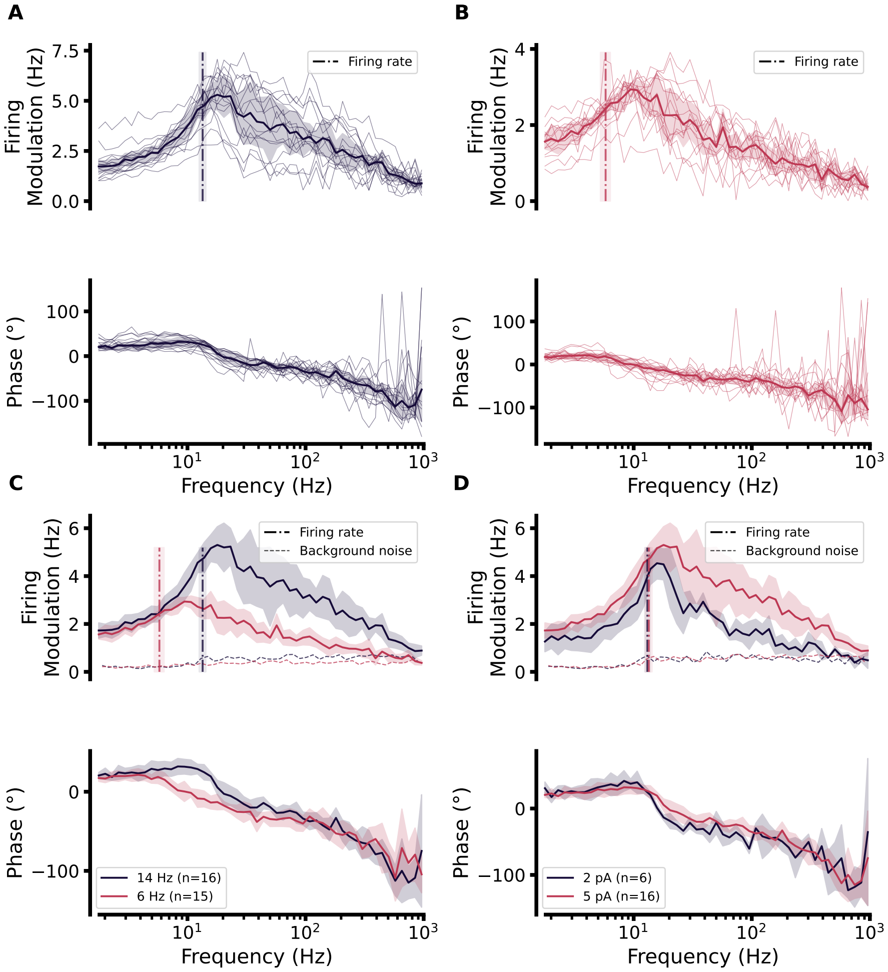

Figure 35:
Cortical Pyramidal cell firing modulation "comb" profiles
A. All the cells for 14 Hz firing rate with a 5 pA/frequency current amplitude. B. All the cells for 6 Hz firing rate with a 5 pA/frequency current amplitude. C. Comparison between 14 Hz and 6 Hz at 5 pA (Between A and B). D. Comparison between amplitude of stimulation for 14 Hz firing rate. Solid lines surrounded by light area represent the median and the MAD of the data. The probed frequencies were arrange in a the "log" scale.

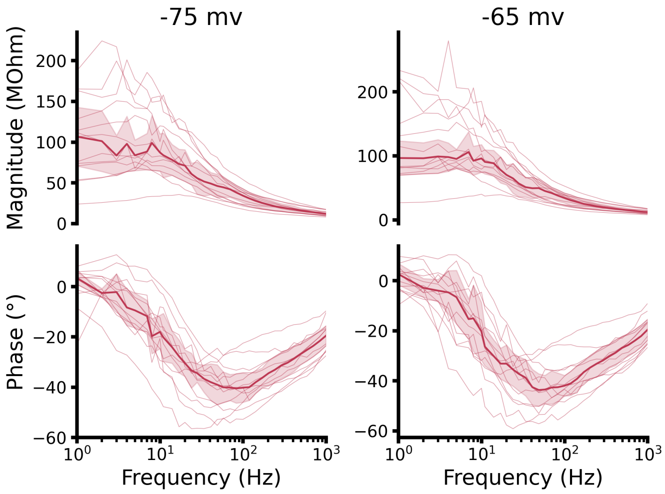

Figure 36:
Pyramidal cell firing and impedance profiles
Solid lines surrounded by light area represent the median and the MAD of the data. Light lines represent individual cells.

are striking by the way in which it does not correspond to the literature of neocortical neurons. Indeed the results showed a quasi straight integration until a cut-off at a rather high frequency. The results we show are closer to pyramidal cells of the hippocampus (Broicher et al., 2012). The next step will be to take the model we used for the Purkinje and see if the pipeline of fitting can work with these cells. But in the Purkinje cells the action potential does not back-propagate in the dendrites as it does in the Pyramidal cell. Surely we will have to incorporate such a mechanism.

Purkinje cells are very easy to spot during experiments, but in the cortex it is sometimes not clear if the cell is pyramidal or stellate and if it is located in the fourth or the fifth layer and so on. Perhaps a simple model fitting with voltages steps and impedance could be helpful to differentiate or even have a more descriptive view of the neocortical cells.

References

- Abbott, L. F. (1999). Lapicque's introduction of the integrate-and-fire model neuron (1907). *Brain Research Bulletin*, *50*(5), 303–304. https://doi.org/10.1016/s0361-9230(99)00161-6

- Albus, J. S. (1971). A theory of cerebellar function. *Mathematical Biosciences*, *10*(1), 25–61. https://doi.org/10.1016/0025-5564(71)90051-4

- Barbour, B. (2018). Electronics for electrophysiologists, 24.

- Beatty, J. A., Song, S. C., & Wilson, C. J. (2015). Cell-type-specific resonances shape the responses of striatal neurons to synaptic input. *Journal of Neurophysiology*, *113*(3), 688–700. https://doi.org/10.1152/jn.00827.2014

- Blinks, L. R. (1928). HIGH AND LOW FREQUENCY MEASUREMENTS WITH LAMINARIA. *Science (New York, N.Y.)*, *68*(1758), 235. https://doi.org/10.1126/science.68.1758.235

- Boucsein, C., Tetzlaff, T., Meier, R., Aertsen, A., & Naundorf, B. (2009). Dynamical response properties of neocortical neuron ensembles: Multiplicative versus additive noise. *The Journal of Neuroscience*, *29*(4), 1006–1010. https://doi.org/10.1523/JNEUROSCI.3424-08.2009

- Broicher, T., Malerba, P., Dorval, A. D., Borisyuk, A., Fernandez, F. R., & White, J. A. (2012). Spike phase locking in CA1 pyramidal neurons depends on background conductance and firing rate. *The Journal of Neuroscience: The Official Journal of the Society for Neuroscience*, *32*(41), 14374–14388. https://doi.org/10.1523/JNEUROSCI.0842-12.2012

- Brumberg, J. C., & Gutkin, B. S. (2007). Cortical pyramidal cells as non-linear oscillators: Experiment and spike-generation theory. *Brain Research*, *1171*, 122–137. https://doi.org/10.1016/j.brainres.2007.07.028

- Brunel, N., Chance, F. S., Fourcaud, N., & Abbott, L. F. (2001). Effects of synaptic noise and filtering on the frequency response of spiking neurons. *Physical Review Letters*, *86*(10), 2186–2189. https://doi.org/10.1103/PhysRevLett.86.2186

- Carandini, M., Mechler, F., Leonard, C. S., & Movshon, J. A. (1996). Spike train encoding by regular-spiking cells of the visual cortex. *Journal of Neurophysiology*, *76*(5), 3425–3441. https://doi.org/10.1152/jn.1996.76.5.3425

- Cole, K. S., & Curtis, H. J. (1938). ELECTRIC IMPEDANCE OF NITELLA DURING ACTIVITY. *The Journal of General Physiology*, *22*(1), 37–64. https://doi.org/10.1085/jgp.22.1.37
- Cole, K. S. (1928). ELECTRIC IMPEDANCE OF SUSPENSIONS OF ARBACIA EGGS. *The Journal of General Physiology*, *12*(1), 37–54.
- Cole, K. S., & Curtis, H. J. (1939). ELECTRIC IMPEDANCE OF THE SQUID GIANT AXON DURING ACTIVITY. *The Journal of General Physiology*, *22*(5), 649–670.
- Couto, J., Linaro, D., De Schutter, E., & Giugliano, M. (2015). On the firing rate dependency of the phase response curve of rat purkinje neurons in vitro. *PLoS computational biology*, *11*(3), e1004112. https://doi.org/10.1371/journal.pcbi.1004112
- De Schutter, E., & Bower, J. M. (1994). An active membrane model of the cerebellar purkinje cell. i. simulation of current clamps in slice. *Journal of Neurophysiology*, *71*(1), 375–400. https://doi.org/10.1152/jn.1994.71.1.375
- Desai, N. S., Gray, R., & Johnston, D. (2017). A dynamic clamp on every rig [Publisher: Society for Neuroscience Section: Methods/New Tools]. *eNeuro*, *4*(5). https://doi.org/10.1523/ENEURO.0250-17.2017
- de Solages, C., Szapiro, G., Brunel, N., Hakim, V., Isope, P., Buisseret, P., Rousseau, C., Barbour, B., & Léna, C. (2008). High-frequency organization and synchrony of activity in the purkinje cell layer of the cerebellum. *Neuron*, *58*(5), 775–788. https://doi.org/10.1016/j.neuron.2008.05.008
- Engel, T. A., Schimansky-Geier, L., Herz, A. V. M., Schreiber, S., & Erchova, I. (2008). Subthreshold membrane-potential resonances shape spike-train patterns in the entorhinal cortex. *Journal of Neurophysiology*, *100*(3), 1576–1589. https://doi.org/10.1152/jn.01282.2007
- Erchova, I., Kreck, G., Heinemann, U., & Herz, A. V. M. (2004). Dynamics of rat entorhinal cortex layer II and III cells: Characteristics of membrane potential resonance at rest predict oscillation properties near threshold. *The Journal of Physiology*, *560*, 89–110. https://doi.org/10.1113/jphysiol.2004.069930
- Fourcaud, N., & Brunel, N. (2002). Dynamics of the firing probability of noisy integrate-and-fire neurons. *Neural Computation*, *14*(9), 2057–2110. https://doi.org/10.1162/089976602320264015

- Fourcaud-Trocmé, N., Hansel, D., van Vreeswijk, C., & Brunel, N. (2003). How spike generation mechanisms determine the neuronal response to fluctuating inputs. *The Journal of Neuroscience: The Official Journal of the Society for Neuroscience*, *23*(37), 11628–11640.
- French, A. S., & DiCaprio, R. A. (1975). The dynamic electrical behaviour of the electrotonic junction between retzius cells in the leech. *Biological Cybernetics*, *17*(3), 129–135. https://doi.org/10.1007/BF00364161
- Gerstner, W. (2000). Population dynamics of spiking neurons: Fast transients, asynchronous states, and locking. *Neural Computation*, *12*(1), 43–89. https://doi.org/10.1162/089976600300015899
- Gimbarzevsky, B., Miura, R. M., & Puil, E. (1984). Impedance profiles of peripheral and central neurons. *Canadian Journal of Physiology and Pharmacology*, *62*(4), 460–462. https://doi.org/10.1139/y84-074
- Gutfreund, Y., yarom, Y., & Segev, I. (1995). Subthreshold oscillations and resonant frequency in guinea-pig cortical neurons: Physiology and modelling. *The Journal of Physiology*, *483 (Pt 3)*, 621–640. https://doi.org/10.1113/jphysiol.1995.sp020611
- Guttman, R., Feldman, L., & Lecar, H. (1974). Squid axon membrane response to white noise stimulation. *Biophysical Journal*, *14*(12), 941–955. https://doi.org/10.1016/S0006-3495(74)85961-8
- Haas, J. S., & White, J. A. (2002). Frequency selectivity of layer II stellate cells in the medial entorhinal cortex. *Journal of Neurophysiology*, *88*(5), 2422–2429. https://doi.org/10.1152/jn.00598.2002
- Higgs, M. H., & Spain, W. J. (2009). Conditional bursting enhances resonant firing in neocortical layer 2–3 pyramidal neurons [Publisher: Society for Neuroscience Section: Articles]. *Journal of Neuroscience*, *29*(5), 1285–1299. https://doi.org/10.1523/JNEUROSCI.3728-08.2009
- Hille, B. (2001, July 16). *Ion channels of excitable membranes* (3rd edition). Sinauer Associates is an imprint of Oxford University Press.
- Hodgkin, A. L., & Huxley, A. F. (1939). Action potentials recorded from inside a nerve fibre [Number: 3651 Publisher: Nature Publishing Group]. *Nature*, *144*(3651), 710–711. https://doi.org/10.1038/144710a0
- Hodgkin, A. L., & Huxley, A. F. (1952). A quantitative description of membrane current and its application to conduction and excitation in nerve. *The Journal of Physiology*, *117*(4), 500–544.

- Hodgkin, A. L., Huxley, A. F., & Katz, B. (1952). Measurement of current-voltage relations in the membrane of the giant axon of loligo. *The Journal of Physiology*, *116*(4), 424–448.

- Hutcheon, B., Miura, R. M., & Puil, E. (1996). Subthreshold membrane resonance in neocortical neurons. *Journal of Neurophysiology*, *76*(2), 683–697. https://doi.org/10.1152/jn.1996.76.2.683

- Hutcheon, B., & Yarom, Y. (2000). Resonance, oscillation and the intrinsic frequency preferences of neurons. *Trends in Neurosciences*, *23*(5), 216–222.

- Ito, M., Sakurai, M., & Tongroach, P. (1982). Climbing fibre induced depression of both mossy fibre responsiveness and glutamate sensitivity of cerebellar purkinje cells. *The Journal of Physiology*, *324*(1), 113–134. https://doi.org/10.1113/jphysiol.1982.sp014103

- Jahnsen, H., & Karnup, S. (1994). A spectral analysis of the integration of artificial synaptic potentials in mammalian central neurons. *Brain Research*, *666*(1), 9–20. https://doi.org/10.1016/0006-8993(94)90277-1

- Johnston, D., & Wu, S. M.-S. (1994, November 2). *Foundations of cellular neurophysiology*. Bradford Books.

- Khaliq, Z. M., Gouwens, N. W., & Raman, I. M. (2003). The contribution of resurgent sodium current to high-frequency firing in purkinje neurons: An experimental and modeling study [Publisher: Society for Neuroscience Section: Cellular/Molecular]. *Journal of Neuroscience*, *23*(12), 4899–4912. https://doi.org/10.1523/JNEUROSCI.23-12-04899.2003

- Kispersky, T. J., Fernandez, F. R., Economo, M. N., & White, J. A. (2012). Spike resonance properties in hippocampal o-LM cells are dependent on refractory dynamics. *The Journal of Neuroscience: The Official Journal of the Society for Neuroscience*, *32*(11), 3637–3651. https://doi.org/10.1523/JNEUROSCI.1361-11.2012

- Knight, B. W. (1972). Dynamics of encoding in a population of neurons. *The Journal of General Physiology*, *59*(6), 734–766. https://doi.org/10.1085/jgp.59.6.734

- Köndgen, H., Geisler, C., Fusi, S., Wang, X.-J., Lüscher, H.-R., & Giugliano, M. (2008). The dynamical response properties of neocortical neurons to temporally modulated noisy inputs in vitro. *Cerebral Cortex (New York, N.Y.: 1991)*, *18*(9), 2086–2097. https://doi.org/10.1093/cercor/bhm235

- Lapicque, L. (1907). Recherches quantitatives sur l'excitation électrique des nerfs traitée comme une polarisation. *J. Physiol. Pathol. Gen.*, (9), 620–635.
- Linaro, D., Couto, J., & Giugliano, M. (2014). Command-line cellular electrophysiology for conventional and real-time closed-loop experiments. *Journal of Neuroscience Methods*, *230*, 5–19. https://doi.org/10.1016/j.jneumeth.2014.04.003
- Lindner, B., & Schimansky-Geier, L. (2001). Transmission of noise coded versus additive signals through a neuronal ensemble. *Physical Review Letters*, *86*(14), 2934–2937. https://doi.org/10.1103/PhysRevLett.86.2934
- Llano, I., Marty, A., Armstrong, C. M., & Konnerth, A. (1991). Synaptic- and agonist-induced excitatory currents of purkinje cells in rat cerebellar slices. *The Journal of Physiology*, *434*, 183–213.
- Llinás, R., & Sugimori, M. (1980a). Electrophysiological properties of in vitro purkinje cell dendrites in mammalian cerebellar slices. *The Journal of Physiology*, *305*, 197–213.
- Llinás, R., & Sugimori, M. (1980b). Electrophysiological properties of in vitro purkinje cell somata in mammalian cerebellar slices. *The Journal of Physiology*, *305*, 171–195. https://doi.org/10.1113/jphysiol.1980.sp013357
- Llinás, R., & Yarom, Y. (1986). Oscillatory properties of guinea-pig inferior olivary neurones and their pharmacological modulation: An in vitro study. *The Journal of Physiology*, *376*(1), 163–182. https://doi.org/10.1113/jphysiol.1986.sp016147
- Llinás, R. R. (1988). The intrinsic electrophysiological properties of mammalian neurons: Insights into central nervous system function [Publisher: American Association for the Advancement of Science]. *Science*, *242*(4886), 1654–1664. https://doi.org/10.1126/science.3059497
- Marmont, G. (1949). Studies on the axon membrane. i. a new method. *Journal of Cellular and Comparative Physiology*, *34*(3), 351–382. https://doi.org/10.1002/jcp.1030340303
- Marr, D. (1969). A theory of cerebellar cortex. *The Journal of Physiology*, *202*(2), 437–470. https://doi.org/10.1113/jphysiol.1969.sp008820
- Mauro, A., Conti, F., Dodge, F., & Schor, R. (1970). Subthreshold behavior and phenomenological impedance of the squid giant axon. *The Journal of General Physiology*, *55*(4), 497–523. https://doi.org/10.1085/jgp.55.4.497

- Moore, L. E., Yoshii, K., & Christensen, B. N. (1988). Transfer impedances between different regions of branched excitable cells [Publisher: American Physiological Society]. *Journal of Neurophysiology*, *59*(3), 689–705. https://doi.org/10.1152/jn.1988.59.3.689
- Napper, R. M. A., & Harvey, R. J. (1988). Quantitative study of the purkinje cell dendritic spines in the rat cerebellum. *Journal of Comparative Neurology*, *274*(2), 158–167. https://doi.org/https://doi.org/10.1002/cne.902740203
- Naundorf, B., Geisel, T., & Wolf, F. (2005). Action potential onset dynamics and the response speed of neuronal populations. *Journal of Computational Neuroscience*, *18*(3), 297–309. https://doi.org/10.1007/s10827-005-0329-8
- Nelson, P. G., & Lux, H. D. (1970). Some electrical measurements of motoneuron parameters. *Biophysical Journal*, *10*(1), 55–73. https://doi.org/10.1016/S0006-3495(70)86285-3
- Osterhout, W. J. V. L. (1922). *Injury, recovery, and death: In relation to conductivity and permeability*. Nabu Press.
- Ostojic, S., Szapiro, G., Schwartz, E., Barbour, B., Brunel, N., & Hakim, V. (2015). Neuronal morphology generates high-frequency firing resonance. *The Journal of Neuroscience: The Official Journal of the Society for Neuroscience*, *35*(18), 7056–7068. https://doi.org/10.1523/JNEUROSCI.3924-14.2015
- Person, A. L., & Raman, I. M. (2012). Purkinje neuron synchrony elicits time-locked spiking in the cerebellar nuclei [Number: 7382 Publisher: Nature Publishing Group]. *Nature*, *481*(7382), 502–505. https://doi.org/10.1038/nature10732
- Puil, E., Meiri, H., & Yarom, Y. (1994). Resonant behavior and frequency preferences of thalamic neurons [Publisher: American Physiological Society]. *Journal of Neurophysiology*, *71*(2), 575–582. https://doi.org/10.1152/jn.1994.71.2.575
- Rall, W. (1960). Membrane potential transients and membrane time constant of motoneurons. *Experimental Neurology*, *2*(5), 503–532. https://doi.org/10.1016/0014-4886(60)90029-7
- Raman, I. M., & Bean, B. P. (2001). Inactivation and recovery of sodium currents in cerebellar purkinje neurons: Evidence for two mechanisms. *Biophysical Journal*, *80*(2), 729–737. https://doi.org/10.1016/S0006-3495(01)76052-3

- Rapp, M., Segev, I., & Yarom, Y. (1994). Physiology, morphology and detailed passive models of guinea-pig cerebellar purkinje cells. [Publisher: Wiley-Blackwell]. *The Journal of Physiology*, *474*(1), 101. https://doi.org/10.1113/jphysiol.1994.sp020006
- Richardson, M. J. E., Brunel, N., & Hakim, V. (2003). From subthreshold to firing-rate resonance. *Journal of Neurophysiology*, *89*(5), 2538–2554. https://doi.org/10.1152/jn.00955.2002
- Roth, A., & Häusser, M. (2001). Compartmental models of rat cerebellar purkinje cells based on simultaneous somatic and dendritic patch-clamp recordings. *The Journal of Physiology*, *535*(2), 445–472. https://doi.org/10.1111/j.1469-7793.2001.00445.x
- Sabah, N. H., & Leibovic, K. N. (1969). Subthreshold oscillatory responses of the hodgkin-huxley cable model for the squid giant axon. *Biophysical Journal*, *9*(10), 1206–1222. https://doi.org/10.1016/S0006-3495(69)86446-5
- Sakmann, B., & Neher, E. (1984). Patch clamp techniques for studying ionic channels in excitable membranes. *Annual Review of Physiology*, *46*, 455–472. https://doi.org/10.1146/annurev.ph.46.030184.002323
- Shelton, D. P. (1985). Membrane resistivity estimated for the purkinje neuron by means of a passive computer model. *Neuroscience*, *14*(1), 111–131. https://doi.org/10.1016/0306-4522(85)90168-x
- Shin, S.-L., Hoebeek, F. E., Schonewille, M., Zeeuw, C. I. D., Aertsen, A., & Schutter, E. D. (2007). Regular patterns in cerebellar purkinje cell simple spike trains [Publisher: Public Library of Science]. *PLOS ONE*, *2*(5), e485. https://doi.org/10.1371/journal.pone.0000485
- Szapiro, G., & Barbour, B. (2007). Multiple climbing fibers signal to molecular layer interneurons exclusively via glutamate spillover. *Nature Neuroscience*, *10*(6), 735–742. https://doi.org/10.1038/nn1907
- Tchumatchenko, T., Malyshev, A., Wolf, F., & Volgushev, M. (2011). Ultrafast population encoding by cortical neurons [Publisher: Society for Neuroscience Section: Articles]. *Journal of Neuroscience*, *31*(34), 12171–12179. https://doi.org/10.1523/JNEUROSCI.2182-11.2011
- Wang, X.-J., & Buzsáki, G. (1996). Gamma oscillation by synaptic inhibition in a hippocampal interneuronal network model [Publisher: Society for Neuroscience Section: Articles]. *Journal of Neuroscience*, *16*(20), 6402–6413. https://doi.org/10.1523/JNEUROSCI.16-20-06402.1996

Personal statement

Experimental considerations

During my PhD I had to build my patch-clamp set-up from scratch. The initial idea was to build it as a modular set-up where each "modules" can be upgraded through time. The first step was to build a "human size" Faraday cage with opening doors on the side to give access to back of the set-up. It took me A few weeks to draw up the plans, find the right material and supplier, before finally constructing it over a weekend with the help of my father. Secondly, in order to be able to easily add lasers for possible light stimulations we needed an "open" microscope. I had to set up a Köhler illumination with a laser beam, some lenses, an open optical tract and a condenser. The third part was to be able to have a rapid flow (up to $15ml/min$) in the patch chamber, with a constant temperature, during experiments. With the use of thermistors (resistance sensitive to temperature) placed in the chamber at the entry and exit point of the extracellular medium, I am able to monitor the temperature with precision in the bath. A Peltier device (thermo-electric heat pump) was put in series to the liquid circulation just before the bath chamber. An arduino collects the thermistors values, computes the bath temperature. Giving a desired temperature it then computes, the product, integral and derivative of the error and returns the adequate voltage to apply at the Peltier's terminals.

Another challenge was that the protocols we wanted to test on cells were not conventional and we wanted to randomise and automate as much as possible. I used the Winwcp software from the University of Strathclyde, because it is open source and was already used in the lab. I was able to create my own protocols in python and write them in files that could be read by the software. I am then able to automatically:

- Switch from voltage to current clamp between protocols.
- Incorporate information to send information for the external (arduino) frequency clamp.
- Arrange intra and inter-protocols features randomly for each cells.

The goal is that as the experimentalist I have the least impact possible on recordings. The inter-cells recordings are similar and this permits a fully automated analysis. To arrange the set-up, the protocols and analysis in this manner was highly time-consuming considering the fact that my personal knowledge in programming at the start of my PhD was limited. However it was necessary to remove numbers of possible parasitising variable, but most importantly have a deeper understanding of how recordings are made and where it could go wrong.

The struggle we encountered trying to model the amplifier is also emblematic of a bigger issue. We realised that what was recorded was not exactly what was written in the protocols. Also, a number of crucial parameters from the amplifier controller, like the pipette capacitance or series resistance compensations are not recorded. But what is inside the amplifiers is not open source, there is no information on the circuits. We had to use some kind of reverse engineering with current injections at different levels of the circuit to try and understand it. The idea that the circuits are known but we don't have access is in my sense dangerous for science. I think that the technology used in research should be openly available. While writing my thesis I saw the initiative of Linaro et al., 2014, and will investigate how to incorporate it in my future set-ups. An interesting project would be to build an open source amplifier combined with a software. That would need to be a collaborative project in order to homogenise recordings and allow everyone to profit from technological advances, as should have been the case when the dynamic clamp was developed (Desai et al., 2017). Also unifying some basic protocols as the membrane voltage step or impedance measurement with known amplifier parameters and filters would make inter-laboratories experiment comparisons with more serenity.

Personal considerations

I come from a rather "classical" biological background. However, with the help of a few classes at University, I was interested in how physics could help me have a more systemic understanding of what I was trying to learn. The combination of biology and physics is interesting; one likes to have a full description of what can be seen, down to the smallest detail, while the other seeks a simple solution to explain as much as it can, if not all. We can see how these views are complementary and antagonist at the same time. Working at the interface of the two for the past four years as been both exiting and terribly tiring. I still think I lack an enormous amount of knowledge and more importantly some kind of intuition required to understand physics concepts, but I think that in a few years I will realise how pushing those boundaries has expanded my understanding capacities. Models give you infinite possibilities of exploration; getting out of a brainstorming meeting over my project with physicist was at the beginning rather overwhelming. The challenge was then to transcript what was said into possible experiments. I sometimes struggled feeling too far from understanding anything and neglecting experiments. But combining scientific domains is essential to understand the complexity of neurons and the brain. The techniques we use are getting more and more complicated but it is important to understand the tools we use. It is worth repeating. This takes time, but this is time well spent.

RÉSUMÉ

L'opération la plus fondamentale d'un neurone est de transformer une entrée synaptique en une sortie en potentiel d'action. On sait que des conductances actives façonnent les réponses de certains neurones aux entrées, généralement à des fréquences d'entrée faibles et modérées. En outre, un mécanisme "morphologique" de résonance du taux d'émission résultant d'une forte asymétrie des compartiments somatiques et dendritiques a été signalé dans les cellules de Purkinje du cervelet. En essayant d'examiner ses mécanismes en détail, nous avons rencontré des difficultés pour effectuer des mesures suffisamment précises des réponses, pour tester des modèles mono-cellulaires précis. Ici, nous décrivons d'une part une approche générale pour construire un modèle cellulaire précis incorporant l'impédance et les conductances actives référées au compartiment somatique, où le potentiel d'action est initié, et d'autre part une conception de mesure permettant la détermination à faible bruit du spectre de modulation. Nous comparons ensuite les réponses mesurées au modèle construit. Nos mesures révèlent une très forte résonance à haute fréquence et que le comportement inter-pic est contrôlé par une AHP prolongé. Nos modèles sont incapables de rendre compte quantitativement de la force de la réponse du Purkinje, suggérant l'existence d'un mécanisme inconnu de résonance à haute fréquence.

MOTS CLÉS

Initiation potentiel d'action   Resonance   Cellule de Purkinje

ABSTRACT

The most fundamental operation of a neurone is to transform synaptic input into output spikes. Active conductances are known to shape the responses of some neurones to inputs, typically at low and moderate input frequencies. In addition, a ‘morphological’ mechanism of firing-rate resonance resulting from a strong asymmetry of somatic and dendritic compartments has been reported in cerebellar Purkinje cells. In attempting to examine its mechanisms in detail, we encountered difficulties in performing sufficiently precise measurements of firing responses to test accurate single-cell models. Here, we describe on the one hand a general approach to constructing an accurate cellular model incorporating impedance and active conductances referred to the somatic compartment, where firing initiates, and on the other hand a measurement design enabling low-noise determination of the spectrum of firing modulation. We then compare the measured firing responses to the constructed model. Our measurements reveal a very strong high-frequency resonance and that interspike behaviour is controlled by a prolonged AHP. Our models are unable to account quantitatively for the strength of the firing response of the Purkinje, suggesting the existence of an unknown mechanism of high-frequency resonance.

KEYWORDS

Spike initiation   Resonance   Purkinje cell